Responses to compiled reviewer and editor comments for manuscript titled: *Erosion rates in a wet, temperate climate derived from rock luminescence techniques*.

In this document, we detail changes to the manuscript in response to each of the reviewer and editor comments. We use the following abbreviations. Please note that the ACs are our responses to the (unedited) reviewer and editor comments.

Reviewer 1 (Benjamin Lehmann) comments: RC1

Reviewer 2 (Anonymous) comments: RC2

Editor comments: EC

Author comments: AC

Reviewer 1: Benjamin Lehmann (RC1)

General comments

RC1: This paper presents a study on the erosion rate history of rock avalanche deposit using surface exposure datings from optically stimulated luminescence signals. The authors present luminescence signals of calibration sites and from rock boulder surfaces. The setting of the rock avalanche deposits is framed by terrestrial cosmogenic nuclide (TCN) dating from the literature. The study is well organized and takes advantage of the previous work on this OSL application by using rock color and texture observations in order to choose the most appropriated calibration samples. The main innovation of this study is the use of a multi-elevated temperature, post-infra-red, infra-red stimulated luminescence (MET-pIRIR) protocol (50, 150 and 225°C) allowing the identification of samples complexities and bringing more constrain to calculate exposure datings and erosion rate histories.

Overall the paper is well written, easy to follow but the figures lake in clarity and bring confusion to the reader. Indeed, Figure 7 is supposed to convince of the good quality of the inversion of the erosion history (erosion rate and time at which the erosion is switch on) from the experimental luminescence signals, but in its current form, the figure does not allow any visual inspection and validation of the results of erosion rate history.

Also, the authors use an approach developed by Lehmann et al., 2019a, in which the use of OSL signals from bedrock surface allows to calculate an erosion correction over TCN dating. Here, this approach in not fully exploited. Erosion rate histories are determined but are not used to discuss the possible erosion correction of the TCN exposure dating.

AC: This is a very good suggestion that we have included in the paper, please see a full explanation in response to your comment on Lines 271-281, which is directly related to this comment.

RC1: Finally, this study brings important observations on the differences of bleaching depth according of the energy traps targeted by the OSL stimulation. The IR50 signals are bleached deeper than pIR150 which is bleached deeper than pIR225, in a way that the higher the temperature of stimulation is, the longer it takes to the light exposure to affect the OSL signal in depth. However, the discussion on the difference of bleaching rate of the different signal could have be brought further. Does the difference in bleaching depth of the different stimulations of a same sample could give us information about complex burial/exposure histories? Do the signals from different stimulations would have the same bleaching difference in a steady state or with a transient state with erosion?

AC: Although, these are very interesting ideas to explore in the future and we thank the reviewer for sharing them, we do not currently consider that our data provides any evidence to explore them to any depth within the discussion of this paper as our samples have very simple burial/exposure histories. As such, we have included a statement to highlight these future research avenues where we discuss the value of using the MET protocol in Section 6.1 as we consider the ideas to be valuable for future research avenues in light of our findings. See below:

Beyond this, it is possible that the MET-pIRIR protocol may be useful in identifying complex burial or exposure histories of rocks, similar to those that have been reported in previous studies but solely using the IR_{50} signal (e.g. Freiesleben et al. 2015; Brill et al. 2021). There is also potential to explore whether the different temperature IRSL signals of the MET protocol record different states of erosion (i.e. steady or transient states) within the same rock surface, whereby the pIRIR signals that are attenuated greater are more susceptible to transient states of erosion in comparison to the lower temperature signals, which measure luminescence depth profiles to greater depths within the rock surface.

Specific comments and technical corrections

RC1: Line 53: The authors should mentioned the work of Brown and Moon, 2019* and Brown, 2020**.

AC: We have added mention of these works in Section 1. It includes the following sentences at the appropriate positions within the paragraph:

Brown (2020) even combine these phenomena within model simulations to explore different sample histories of exposure and burial to inform geomorphological interpretations of luminescence depth profiles measured for samples collected from the natural environment.

Recent findings from erosion simulations compared with measured data have shown that the erosion rates derived from luminescence depth profiles can be accurate even with stochastic erosion as experience in nature (Brown and Moon, 2019).

RC1: Line 90: The authors should mentioned the work of Brill et al., 2021***.

AC: We agree and have added the work of Brill et al. (2021) on carbonate limestones into our text:

Studies have applied rock luminescence techniques (mostly exposure dating) to a variety of lithologies including granites, gneisses (Lehmann et al. 2018 2019a,b; Meyer et al. 2019), sandstones (Sohbati et al. 2012; Chapot et al. 2012; Pederson et al. 2014), quartzites (Gliganic et al. 2019) and carbonate limestone (Brill et al. 2021).

RC1: Lines 208-213: How do the raw data Lx/Tx were normalised (L0 determination)? Is it done for each core individually or for each sample (considering the same L0 for every core of a same sample)? Core 3 for IR50 signal of sample ROAD3 (Fig. 4D) for example, seems to be normalised too low. I would recommend to normalise each independently. The normalisation approach should also be mentioned the Fig. 4 caption.

AC: The raw data L_x/T_x for each core was normalised individually as you suggest. There is a large amount of scatter in the saturated plateau of the cores (as is typical in rock luminescence depth profiles) which makes Core 3 for IR_{50} signal of sample ROAD03 (Fig. 4D) look low, but it is not

inconsistent with the rest of the samples. Based upon your suggestion, we have added an explanation of the normalisation approach in the caption of Fig. 4:

All of the raw L_n/T_n data presented in this figure were normalised individually for each core and subsequent analysis uses the data in this format.

RC1: Lines 219-221: The difference in depth of the bleaching front regarding the difference of ages of sample ROAD02 and ROAD03 could be explain also with the noise of the signal, the orientation of the sampled faces, difference at the rock surface.

AC: We have added this as an example within the text to illustrate factors that may influence the light penetration in our calibration samples as suggested:

This suggests that either another factor is influencing light penetration with depth in these rocks (e.g. small differences in the orientation of the sampled rock faces)…

RC1: Lines 214-221: How does the fit (black lines) in Fig. 4 are produced? This should be mentionned in the main text and in the caption of Fig. 4.

AC: In the text we have added the following sentence in response to this comment:

Note that the inferred models shown in Fig. 4 were fit using the $\overline{\sigma\varphi_0}$ and μ values included in each figure. See Section 5.2 for further explanation of the estimation of the model parameters.

While in the caption of Fig. 4 we have included an explanation of how the fit was produced and also provided the sigmaphi and mu values in each figure to provide further clarification (this is in response to other reviewer comments):

The black line shown is the inferred model that was fitted to derive the corresponding $\overline{\sigma\varphi_0}$ and μ values included in each figure.

RC1: Line 229: "sample BALL01 was coarser grained than BALL02 and BALL03" this affirmation is not supported by the results shown in Fig. 3B where only the two first discs of sample BALL01 are coarser than the other samples BALLs but deeper into the signal BALL03 seems to has the coarsest grained texture.

AC: We have edited the text so that it specifies that the surface is coarser:

… the surface of sample BALL01 was coarser grained than BALL02 and BALL03 (Fig. 2; Fig. 3b).

RC1: Lines 232-233: "[…] lost during sample and/or sample preparation […]". Are there any ways to invalidate this experimental bias? During the sampling, did you mark the exposed surface with ink? Did you measure the core before and after slicing? Does the surface of the first disc look alike the surface of other 1st disc of other cores?

AC: Yes, we did all those suggestions during sampling and preparation as we were very careful. Prior to writing the paper, we revisited all information on this sample, visually inspecting all of the

discs, cores and core holes in the rocks, and could not find any other explanation. We have added a clarification of this into the text, but cannot invalidate the statement definitively so retain the narrative. See below:

Thus, although care was taken when sampling to mark the surface of rock and to measure the rock cores before and after slicing, it is possible that the luminescence depth profile (likely <10 mm based on BALL02 and BALL03) was lost during sampling and/or sample preparation due to the presence of a fragile weathering crust, potentially with a sub-surface zone of weakness (e.g. Robinson and Williams, 1987).

RC1: Lines 244-245: "sigmaphi0 and μ were calibrated using the known-age sample […]" Reading this sentence I was confused that ROADs samples are the calibration samples. "ROAD samples" could be explicitly mentioned in this sentence to improve clarity.

AC: We have added this to the sentence:

$\overline{\sigma\varphi_0}$ and μ were calibrated using Eq (1) and the known-age samples (ROAD01, ROAD02 and ROAD03) of similar, suitable rock composition as determined by the down-core profiles of RGB and grainsize (Section 4.2).

RC1: Lines 253-258: There is no mention of the results for the calibration of sigmaphi0 and μ parameters. They should be explicitly written in the main text.

AC: We had original omitted this because it turns into a long list in the text that is much more easily read from the table. However, to respond to the reviewers comment here, we have added a few sentences listing the parameters in the text:

For ROAD01, the parameters determined using the IR_{50} (μ = 3.2 mm^{-1}, $\overline{\sigma\varphi_0}$ = 2.80e^{-4} s^{-1}), $pIRIR_{150}$ (μ = 3.1 mm^{-1}, $\overline{\sigma\varphi_0}$ = 3.27e^{-5} s^{-1}) and $pIRIR_{225}$ (μ = 3.0 mm^{-1}, $\overline{\sigma\varphi_0}$ = 2.88e^{-5} s^{-1}) signals were broadly consistent. For ROAD02, the parameters differed between the IR_{50} (μ = 2.1 mm^{-1}, $\overline{\sigma\varphi_0}$ = 6.67e^{-6} s^{-1}), $pIRIR_{150}$ (μ = 1.5 mm^{-1}, $\overline{\sigma\varphi_0}$ = 1.73e^{-8} s^{-1}) and $pIRIR_{225}$ (μ = 2.8 mm^{-1}, $\overline{\sigma\varphi_0}$ = 9.01e^{-8} s^{-1}) signals, but the values for each signal were broadly similar to the equivalent values determined for ROAD03 using the IR_{50} (μ = 2.7 mm^{-1}, $\overline{\sigma\varphi_0}$ = 1.56e^{-5} s^{-1}), $pIRIR_{150}$ (μ = 1.5 mm^{-1}, $\overline{\sigma\varphi_0}$ = 3.80e^{-8} s^{-1}) and $pIRIR_{225}$ (μ = 1.4 mm^{-1}, $\overline{\sigma\varphi_0}$ = 1.70e^{-8} s^{-1}) signals.

RC1: Lines 258-260: Note that the μ value for ROAD03 are not so different than the ones for ROAD02 even if the grain size are very different. Could you comment on that?

AC: Yes, we have added a comment as suggested:

Given the similarity of $\overline{\sigma\varphi_0}$ and μ determined using all three IRSL signals for ROAD02 and ROAD03 and the difference in grainsizes (Fig. 3B), it suggests that grainsize has a minimal impact upon the attenuation of light into a rock surface in comparison to other factors (e.g. mineralogy, surficial coatings).

RC1: Lines 262-266: All the values mentioned in this section are different than the values in Table 3!

AC: We thank the reviewer for noticing these mistakes and have corrected the text accordingly.

RC1: Line 305: The "(2018)" reference is wrong and it should "(2019a)"

AC: We have corrected this in text.

RC1: Lines 271-281: Now that you inferred erosion history is determined for the two boulders, what are the consequences on the cosmo age of the deposit? Does the sampled boulders are the same sampled for TCN dating? If not, it would be interested to discuss the potential exposure age correction. Lehmann et al., 2019a approach does correct the TCN age with the inferred erosion history. It seems that the approach is not fully exploited here.

AC: This is a very good suggestion that we have incorporated into the paper as a paragraph within Section 6.2, which is included below:

The modelled erosion histories that we have calculated here using the luminescence erosion-meter for samples BALL02 and BALL03 would have had a minimal effect upon the cosmogenic nuclide exposure age (4.54 ± 0.27 ka; Ballantyne and Stone, 2004). Only the steady-state erosion rate of 66 mm/ka inferred for BALL02 using the IR_{50} signal, when applied for durations exceeding 1 ka, would have increased the exposure age to any great degree. For example, when the steady-state erosion rate of 66 mm/ka was applied for 0.1 ka, the corrected cosmogenic nuclide exposure age would have been 4.58 ka and, when the same erosion rate was applied for 1 ka it would have been 4.99 ka; these corrected ages are consistent within ± 2 σ uncertainties of the uncorrected age of 4.54 ± 0.27 ka (Ballantyne and Stone, 2004). The higher, transient erosion rates inferred for BALL03 were all applied for such a short period of time (e.g. Table 3) that they had a minimal effect on the cosmogenic nuclide exposure age.

Based on the long-term erosion rates derived here, the boulder sampled for BALL02 would have lost a total of 300 mm (IR_{50}), 41 mm ($pIRIR_{150}$) and 54 mm ($pIRIR_{225}$) from the surface over 4.54 ka, while the long-term erosion rates determined for BALL03 suggested that the boulder surface would have lost 27 mm (IR_{50}), 64 mm ($pIRIR_{150}$) and 50 mm ($pIRIR_{225}$). All of these values (except for the IR_{50} signal of BALL02) were broadly consistent with field observations of quartz protrusions on the surface of boulders >2 x 2 x 2 m that were densely distributed within the rock avalanche feature (Fig. 1). Alternatively, the maximum (shorter-term) erosion rate end members of the transient erosion histories would have removed 1407 mm (BALL02, $pIRIR_{225}$), 2088 mm (BALL03, IR_{50}), 454 mm (BALL03, $pIRIR_{150}$) and 817 mm (BALL03, $pIRIR_{225}$) from the boulder surface over the 4.54 ka. These large values were inconsistent with field evidence and so indicative of the transient state of erosion where high erosion rates were only sustained over short periods of time.

RC1: Lines 355-365: Do field observations of the deposit of weathered material on/in the ground/soil below the blocks have been done and would validate the hypothesis raised in this paragraph?

AC: We have included the sentence below in Section 6.3 to discuss field observations of weathered material and also included a photograph of the wider area in Fig. S6 newly included in the supplementary material to illustrate our observations:

This is also supported by a lack of shattered material surrounding the large sampled boulders (and in fact on much of the Beinn Alligin rock avalanche deposit), despite the presence of dense vegetation surrounding the boulders (e.g. Fig. S6.

RC1: Figure 1: This figure could be highly improved by adding in Panel B, the outline of the rock avalanche deposit, the elevation isoline or two elevation points and the coordinates. In Panel C, the north or flow direction of the rock avalanche deposit.

AC: We have added the outline of the rock avalanche into Fig. 1C in addition to the elevations. We have also added the rock avalanche flow direction into each image of Fig. 1D.

RC1: Figure 2: The scale could be directly placed on the figure.

AC: The scale has now been added to the figure.

RC1: Figure 3: The direction of the y-axis label should be turned 180° to be consistent with other figures.

AC: The axes have been turned by 180° so that the plot is consistent with other figures.

RC1: Figure 4: The uncertainties of the inversion could be plot as an envelope using ±1sigma of the μ and sigmaphi0.

AC: Thank you for this comment, it was very enlightening. We have produced inferred models for each of the ROAD samples using the ± 1 σ $\overline{\sigma\varphi_0}$ and μ values as suggested here. These lines are included in Fig. 4 and we have added a sentence into the figure caption to describe how they were produced.

RC1: Figure 6: In every sub figure, an age is written in white, for example (0.01 a^{-1}) in Fig. 6A. Does unit [a^{-1}] is the correct unit? Also, the units are mentioned with "[ ]" but should be "( )" for consistency with the rest of the paper.

AC: You are absolutely correct, sorry for the mistake. We have corrected both the units and the brackets in Fig. 6.

RC1: Finally, the inversions for each stimulation of the ROAD01 sample appear to explore a truncated range of μ values, that is, the probabilities of 1 (yellow) reach the side of the inspection box. The μ values obtained will surely be much higher if the inversion will allow to explore the values of μ up to 5 or 6 mm^{-1}.

AC: We have not extended the axes of these inversions as ROAD01 had such a short exposure history of only 0.01 a. Thus, there is large uncertainty in these inversions. We use it as a means of demonstrating that even very short durations of exposure can lead to the development of a luminescence depth profile, but do not use them for calibrating any of our samples and so retain the use of the original parameter space. If we were using them for calibration, we would of course provide a wider parameter space; however, it is unlikely that the data would then have such large uncertainties and so would likely not need this.

RC1: Figure 7: The formatting of this figure should be considerably improved. The panels A, B, C, G, H, I do not allow any visual inspection of the data and inversion qualities (for ex: the x-axis boundaries should be set between 0 and 20 mm). The inversions in C, G, H and I do not seem to fit to the experimental value. This figure should be THE figure of the paper, but in the current formatting, it removes persuasive force of the results on the erosion rate history and confuses the conveyed message by the study.

AC: To improve the data visualisation, we have removed the luminescence depth profiles from Fig. 7 and included the inferred erosion models in the luminescence depth profiles of Fig. 5. Fig. 7 now only includes the inversion model profiles of likelihoods. We have provided additional comments on the fit of the inferred erosion models to the experimental data in "Section 5.3 Apparent exposure ages and erosion rates".

RC1: Figures S1, S4: These figures are too pixelised and should be improved.

AC: Both figures have been re-exported, which has improved the resolution.

RC1: Supplementary material: Raw data of Lx/Tx luminescence with depth for every core/sample could be shared in the supplementary material.

AC: We have provided the raw data of the luminescence depth profiles in the supplementary material from Table S2-S7. We have also included a note explaining the availability of this data in the supplementary material in the figure captions.

RC1: Formatting: In general, there is a lack in consistency between the labelling of figures (i.e. Fig. 4 A, B) in uppercase letters and its mention in the main text (i.e. Fig 4 a, b) in lowercase letters.

AC: Apologies, I think some confusion arose around journal formatting regulations. We have corrected all of these formatting issues.

RC1: *Brown, N. D., & Moon, S. (2019). Revisiting erosion rate estimates from luminescence profiles in exposed bedrock surfaces using stochastic erosion simulations. Earth and Planetary Science Letters, 528, 115842.

**Brown, N.D. (2020) Which geomorphic processes can be informed by luminescence measurements?, Geomorphology, https://doi.org/10.1016/ j.geomorph.2020.107296

***Brill, D., May, S. M., Mhammdi, N., King, G., Lehmann, B., Burow, C., ... & Brückner, H. (2021). Evaluating optically stimulated luminescence rock surface exposure dating as a novel approach for reconstructing coastal boulder movement on decadal to centennial timescales. Earth Surface Dynamics, 9(2), 205-234.

AC: Thank you for the reference suggestions here, we have added them into the text and reference list.

Reviewer 2: anonymous (RC2)

General remarks

RC2: The paper "Erosion rates in a wet, temperate climate derived from rock luminescence techniques" presents new data for the application of luminescence rock surface techniques. The approach is applied to rock avalanche deposits from Scotland that have previously been dated by terrestrial cosmogenic nuclides to infer regional erosion rates for the last millennia. The study is well structured, well written and generally easy to follow. It presents valuable new results for the emerging topic of luminescence rock surface dating and erosion rate modelling that are highly needed to better understand the limitations and the potential of the technique. Innovative methodological aspects of the study are the use of a MET-post-IR-IRSL protocol to provide internal quality criteria for the selection of samples with appropriate lithology to adequately record light penetration into the rock surface.

There are several inconsistencies in the paper with regard to the presentation of the data. In particular numbers presented in the main text, the tables and figures do not always match (I will provide details below). This must be revised prior to publication.

AC: We thank the reviewer for bringing this to our attention and have corrected all of the inconsistencies and formatting issues within the paper. Please see the tracked changes document for details.

RC2: Another irritating aspect that needs clarification is the model fit for the unknown age samples in Figure 7. It seems that the inferred model does not really fit the measured data for most of the measured signals. This might indicate inadequate values for μ and/or sigmaphi and the authors should comment on that.

AC: This is a sound observation and so we have further explored this. Firstly, we have moved the inferred erosion model from Fig. 7 to Fig. 5, so that Fig. 7 now only includes the inversion profiles. We have also included further discussion into "Section 5.3 Apparent exposure ages and erosion rates" of the fits in response to the RCs:

At face value, the fit of the inferred erosion model to the experimental data for BALL02 using the IR_{50} (Fig. 5D) and $pIRIR_{150}$ (Fig. 5E) signals is better than the equivalent fits for BALL02 using the $pIRIR_{225}$ signal (Fig. 5F) and BALL03 using the IR_{50} (Fig. 5G), $pIRIR_{150}$ (Fig. 5H) and $pIRIR_{225}$ (Fig. 5I) signals. In the latter cases, the inferred erosion model is shallower than the experimental data. This could suggest that the $\overline{\sigma\varphi_0}$ and μ values were inaccurate, i.e. the attenuation of light with depth into the rock surface is lower in BALL02 and BALL03 than estimated by ROAD02. A possible explanation for this is that the surface of the roadcut sampled by ROAD02 (Fig. S1a) was orientated differently to the Beinn Alligin rock avalanche boulders sampled by BALL02 and BALL03 (Fig. 1), relative to the incoming sunlight (e.g. Gliganic et al. 2019). If the orientation of the known-age roadcut samples was inconsistent with the unknown samples, we would expect these inconsistencies to manifest similarly in all three MET signals for BALL02 and BALL03, which was not observed here. A factor that is common to all the profiles that are less well fit by the inferred erosion model is that they determined transient erosion rates. This suggests that these surfaces experienced complex erosional histories over time whereby the erosion was time-varying. Consequently, it is possible that surficial weathering products may have changed in thickness and composition over time, which in turn could slightly vary the attenuation of light (Meyer et al. 2018; Luo et al. 2018), meaning that the calibration of $\overline{\sigma\varphi_0}$ and μ from ROAD02 would introduce more uncertainty into the inferred erosion model. It is possible that sample-specific measurements of $\overline{\sigma\varphi_0}$ and μ (e.g. Ou et al. 2018), rather than calibration from

known-age samples, could reduce the uncertainty introduced by time-varying light attenuation. However, further investigation is required into the physical mechanisms of time-varying light attenuation in the context of surficial weathering and subsequent erosion, and the impacts upon inferred transient erosion rates.

Specific comments

RC2: Lines 79-80: Please add a reference for the insights on the exposure history.

AC: We have added the citation for the exposure history from Ballantyne and Stone (2004).

RC2: Lines 85-93: The shape and position of the bleaching front is also influenced by dose accumulation during exposure. Although this term is irrelevant for most samples, the authors should include a short explanation why they think it is not necessary to address dosing in their setting. It is also confusing that dose rates are considered in the methods section, while they are not part of equation (1). This is confusing and needs clarification.

AC: We have now added worked examples into "Section 2 Theoretical background" in response to the ECs comments, which provides improved clarification on how the dose accumulated over the exposure time is incorporated into the modelling. Please see comments below where we respond to the ECs comments for further information.

RC2: Lines 104-107: How do you consider temporal variability of μ? With your approach you rather account for spatial variability of light attenuation between different surfaces and in different depth levels of a surface.

AC: It is not possible to determine the temporal variability of μ as we cannot monitor this in real-time over thousands of years. As such, none of the existing studies consider the temporal variability of μ. Similarly, we cannot measure it here. However, we do include some consideration of the possibility that μ is time-dependent when exploring the potential explanations for the fit of the inferred erosion models to the experimental data in Section 5.2 in response to a number of comments from RC1 and RC2.

RC2: Lines 176-177: Please provide details regarding internal dose rate assessment here. What internal potassium contents were used? How exactly has sample grain size been determined?

AC: This information was provided in the caption for Table 1, however, we have also included the information in the text in response to the reviewers comment:

Internal dose-rates were calculated assuming an internal K-content of 10 ± 2 % (Smedley et al. 2012) and internal U and Th concentrations of 0.3 ± 0.1 ppm and 1.7 ± 0.4 ppm (Smedley and Pearce, 2016), in addition to measured average grain sizes for each sample.

RC2: Line 190: This should be "successively" instead of "simultaneously".

AC: We have exchanged these words in the text where suggested and in Section 4.1 where it also applies.

RC2: Line 196: Please provide the number of cores that were used per sample.

AC: We had already included this information in the original manuscript. See below:

De values were determined for the shallowest disc and the deepest disc from one core of each sample to quantify the natural residual dose and saturation limit (L0, Eq. 1), respectively.

RC2: Line 202: "…were in line with previous measurements of IRSL signals"

AC: We have corrected this in the text. See the tracked changes document.

RC2: Lines 219-220: How exactly was grain size determined with the microscope? Did you use a software or were grains measured manually? For the latter, how many grains were measured per slice?

AC: We have added additional information into the text to explain the methods of measuring grainsize. See below:

The average down-core grainsize of each sample was measured under an optical microscope using Infinity Analyze. For each rock slice of an example core per sample, ten randomly-selected grains were measured and the mean and standard deviation grainsize were calculated per core and plotted against the core depths (Fig. 3B).

RC2: Line 235: Which values for μ and sigmaphi have been used for the fits in Figure 4? I assume you used the parameters presented in section 5.2? If so, I would suggest to change the order of sections 5.1 and 5.2.

AC: In response to other reviewer's comments, the parameters used to fit the data shown in Fig. 4 are now included in each plot, which will clarify what parameters were used to fit each dataset. We have not changed the order of Sections 5.1 and 5.2 as Section 5.1 presents the data and describe the luminescence depth profiles in their raw form, and then Section 5.2 then fits this raw data to determine the parameters, so it would not make sense to us to switch the two sections around.

RC2: Lines 236-237: The numbers given for the depths of the IR50 bleaching front do not agree with the modelled fits in figure 4. Please clarify.

AC: This is a fair comment and we thank the reviewer for highlighting the point. We originally presented the depth of the first rock slice that measured an L_n/T_n value that was >50 % of the saturation plateau, which meant that it was much deeper than the model fit, and as highlighted here, misleading. We have rectified this by referring to the position of the bleaching front according to the fits show in Fig. 4 and corrected the text (see tracked changes document). We have also corrected the values presented in Fig. S4a.

RC2: Lines 265-268: Here dose rates are considered, although the term for dose accumulation is not part of equation (1). So either it was not equation (1) that was used for fitting, or the dose rate information is not needed. Please clarify.

AC: This is a fair comment as it was not clear exactly how the dose-rate information is used in the parameterisation of $\overline{\sigma\varphi_0}$ and μ, and age/erosion rate determination. We have provided more clarity in this section and refer the reader to our new worked example of the inversion model (requested in the Editors Comments - ECs) for further explanation, but we summarise relevant amendments here:

$\overline{\sigma\varphi_0}$ and μ were calibrated using Eq. 1 and the known-age samples (ROAD01, ROAD02 and ROAD03) of similar, suitable rock composition as determined by the down-core profiles of RGB and grainsize (Section 4.2). Note that ($\dot{D}$) is not considered in Eq. 1 but is used to determine an apparent exposure or erosion rate and so needs to be measured for each sample.

RC2: Line 282: The values of Sohbati et al. (2012) are for quartz signals, thus for a different wave length spectrum. Since different wave lengths are attenuated differently, I would suggest to compare with other feldspar studies.

AC: A very good point, thank you. We have removed reference to Sohbati et al. (2012).

RC2: Lines 282-286: Please provide the numbers for μ and sigmaphi directly in the text.

AC: We had originally omitted this because it turns into a long list in the text that is much more easily read from the table. However, to respond to the reviewers comment here, we have added a few sentences listing the parameters in the text:

For ROAD01, the parameters determined using the IR_{50} (μ = 3.2 mm^{-1}, $\overline{\sigma\varphi_0}$ = 2.80e^{-4} s^{-1}), $pIRIR_{150}$ (μ = 3.1 mm^{-1}, $\overline{\sigma\varphi_0}$ = 3.27e^{-5} s^{-1}) and $pIRIR_{225}$ (μ = 3.0 mm^{-1}, $\overline{\sigma\varphi_0}$ = 2.88e^{-5} s^{-1}) signals were broadly consistent. For ROAD02, the parameters differed between the IR_{50} (μ = 2.1 mm^{-1}, $\overline{\sigma\varphi_0}$ = 6.67e^{-6} s^{-1}), $pIRIR_{150}$ (μ = 1.5 mm^{-1}, $\overline{\sigma\varphi_0}$ = 1.73e^{-8} s^{-1}) and $pIRIR_{225}$ (μ = 2.8 mm^{-1}, $\overline{\sigma\varphi_0}$ = 9.01e^{-8} s^{-1}) signals, but the values for each signal were broadly similar to the equivalent values determined for ROAD03 using the IR_{50} (μ = 2.7 mm^{-1}, $\overline{\sigma\varphi_0}$ = 1.56e^{-5} s^{-1}), $pIRIR_{150}$ (μ = 1.5 mm^{-1}, $\overline{\sigma\varphi_0}$ = 3.80e^{-8} s^{-1}) and $pIRIR_{225}$ (μ = 1.4 mm^{-1}, $\overline{\sigma\varphi_0}$ = 1.70e^{-8} s^{-1}) signals.

RC2: Lines 288-292: The unit of the ages should be a instead of a^{-1}. Also the numbers do not match those in table 3.

AC: We have corrected these mistakes in the text.

RC2: Lines 306-309: Please provide numbers for erosion rates in the text.

AC: Similar to above, we had originally omitted this because it turns into a long list in the text that is much more easily read from the table. However, to respond to the reviewers comment here, we have added the following text listing the parameters in the text:

However, the $pIRIR_{225}$ signal suggested a transient erosion state, where the luminescence signal could be derived from numerous pairs of erosion rates and initiation times from a maximum erosion rate of 310 mm/ka over a minimum time interval of 4 a to a minimum erosion rate of 12 mm/ka over time a minimum time interval of 90 a. All three IRSL signals from sample BALL03 consistently suggested a system undergoing a transient response to erosion, which was consistent with the $pIRIR_{225}$ signal of BALL02 (Fig. 7, Table 3). The IR_{50} signal for BALL03 derived a maximum erosion rate of 460 mm/ka over a minimum time interval of 3 a and a minimum erosion rate of 6 mm/ka over a minimum time interval of 231 a. The $pIRIR_{150}$ signal for BALL03 derived a maximum erosion rate of 100 mm/ka over minimum time interval of 19 a and a minimum erosion rate of 14 mm/ka over a minimum time interval of 137 a. The $pIRIR_{225}$ signal for BALL03 derived a maximum erosion rate of 180 mm/ka over a minimum time interval of 4 a and a minimum erosion rate of 11 mm/ka over a minimum time interval of 73 a.

RC2: Line 317: Based on the modelled fits shown in figure 7 (red lines), the fit seems not to match the measured data for most of the signals, which indeed indicates that the parameters might be inaccurate. This should be explored in more detail.

AC: This was also identified by RC2 in their more general comments above and so we have provided a more detailed response there of the further discussion that we have included exploring the fit of the inferred erosion models to the experimental data. The same response applies to this comment.

RC2: Lines 327-329: This assumption does not really make sense in my opinion. Post-IR_{225} signals need shorter wave lengths than IR_{50} and post-IR_{150} signals to be reset. But the attenuation of shorter wave lengths in rocks tends to be stronger than that of longer wave lengths (cf. Ou et al., 2018).

AC: In this statement we are suggesting that it is the Fe-coating that forms as a weathering product on the surface of the rock that may have preferentially attenuated the longer wavelengths that would reset the IR_{50} and $pIRIR_{150}$ signals, rather than the referring to the rock itself. An Fe-coating and crystalline rock would have very different compositions. However, we appreciate that this is a speculative statement and to respond to the reviewer's comment here, we have re-phrased this sentence to better reflect the evidence we present. See below:

Interestingly, the similarity between BALL02 and BALL03 for the $pIRIR_{225}$ signal suggests that the presence of an Fe-coating altered the attenuation of the IR_{50} and $pIRIR_{150}$ signals to a lesser extent than the $pIRIR_{225}$ signal, but the reasons for this requires further investigation.

RC2: Line 343: I think it should be "exploited" or similar instead of "inferred"?

AC: We have considered this comment at length and currently do not understand how the word exploited would replace inferred. If the authors were exploiting the fact that shorter-term erosion rates derived from luminescence measurements were higher than the long-term averages, then they would needed to have used them for some specific purpose after calculating them. From our understanding, the authors essentially reported that shorter-term erosion rates derived from luminescence measurements were higher than the long-term averages; thus, the word "inferred" is appropriate in this case. We would welcome further clarification if required.

RC2: Figure 1: Please also mark the locations of the road cuts and provide photographs of the road cut sampling sites.

AC: To allow the roadcut sample locations to be shown, we have added an extra panel into Fig. 1 (Fig. 1B) to include the sample locations in NW Scotland. We have included photographs of the roadcut sections in the Supplementary material.

RC2: Figure 3: Why are the datasets for grain size and RGB different? Were the analysis performed on different slices?

AC: The measurements were not performed on exactly the same cores, but example cores for each sample. We have added the text below into the figure caption to clarify this:

Note that the RGB values and grainsize measurements were not derived from exactly the same cores, but example cores for each sample.

RC2: Figure 4: I would suggest to mention in the figure caption that core 3 of Road 2 was not considered for fitting. Also, information regarding the inferred model (which μ, which sigmaphi, reference) should be provided.

AC: We have added the following text into the figure caption for Fig. 4 “Note that core 3 of ROAD02 was not considered for fitting”. We have also included the μ and sigmaphi values in each plot as it was an excellent suggestion.

RC2: Figure 5: I recommend to add the inferred model fits that are shown in figure 7 also here. In figure 7 it seems that the model fits (red lines) do not match the measured data for most signals, but it is hard to judge since the panels are rather small. Figure 5 would allow for a much better evaluation.

AC: We have moved the inferred erosion models from Fig. 7 to Fig. 5 to better represent the data and fit. Fig. 7 is now limited to only the inversion model profiles of erosion rates.

RC2: Figure 6: The unit for the ages should be a instead of a^{-1}.

AC: You are absolutely correct, sorry for the mistakes. We have corrected this.

RC2: Figure 7: It seems that the model (red lines) in C, G, h and I does not really fit the data. Could you please comment why this might be the case? Please also provide more information on the likelihoods (where do these come from) and the forbidden zone (how do I recognize it in the figure).

AC: This was also identified by RC2 in their more general comments above and so we have provided a more detailed response there of the further discussion that we have included exploring the fit of the inferred erosion models to the experimental data. The same response applies to this comment. Also, the new worked examples in “Section 2 Theoretical background” also includes further details on the calculations of likelihoods and the forbidden zone. These additions were included in response to the ECs and so we refer you to our response to the ECs for full details.

RC2: Figure S4a: The signals are only identical for sample ROAD 01 (1 a reference sample).

AC: Correct, we have added the missing text “for ROAD01 (0.01 a known-age sample)” into the caption to clarify this.

Associate Editor comments: Jim Feathers

EC: Associate editor here.

The two reviews of Smedley et al. on erosion rates in NW Scotland have now been posted. I read them over and think they made many good points. The authors should address all their comments, but two in particular need attention. First, both reviewers found Figure 7 difficult to understand. I found the graphs with mostly blue shading to be fully incomprehensible, yet as one of the reviewers pointed out it is the main figure of the paper. Second, the authors rely heavily on Lehmann et al.'s approach for determining erosion rates that are punctuated rather than steady state. The authors need to better explain that approach, so that the reader does not have to consult Lehmann et al. to understand what the authors are doing. I would suggest giving a working example of how this approach works, using one of their samples as the example.

AC: We thank the EC for this suggestion and agree that this will add clarity to the approach used here. As such, we have added two paragraphs into “Section 2 Theoretical background” that provide worked examples of steady state and transient state erosion based on our data presented in Fig. 7 (revised). See the paragraphs below:

For determining erosion rates for rock surfaces of known exposure age, Sohbati et al. (2018) use a confluent hypergeometric function to provide an analytical solution, but assuming only steady-state erosion. Lehmann et al. (2019a) provide a numerical approach that exploits the differential sensitivities to erosion of the luminescence (shorter-term) and cosmogenic nuclide (longer-term) techniques to erosion to infer erosion histories (steady state and transient over time) for rock surfaces. This approach uses the experimental data from the luminescence depth profiles and the ^{10}Be concentrations for the same sample. Modelling of the luminescence depth profiles accounts for the electron trapping dependent upon the environmental dose-rate and D_0 but does not consider athermal loss of the signal (i.e. anomalous fading) as it has been demonstrated to have a negligible impact upon the luminescence depth profiles (Lehmann et al. 2019a). Modelling of the ^{10}Be concentrations assumes that no inheritance of the cosmogenic nuclides from prior exposure has occurred, and that the ^{10}Be concentrations have been corrected for the sample depth and density, topographical shielding, local production rates, and the sample location (longitude, latitude and elevation). The combined experimental data for the luminescence depth profiles and cosmogenic nuclides are solved simultaneously for two unknowns: the exposure age and the erosion rate. Forward modelling is used to calculate all of the possible combinations of luminescence depth profiles and ^{10}Be concentrations for synthetic erosion and exposure histories, which are then validated using inversion models against the experimental data to determine the combinations with the highest likelihood. A forbidden zone is determined where the range of possible solutions of erosion rates and durations are in excess of those that are feasible for the experimental ^{10}Be concentrations provided for the sample; these solutions are excluded from the parameter ranges used for the inversion model. For example, the forbidden zone identified in the inversion model profile shown in Fig. 7A is restricted to ranges from ca. 10^4 mm/ka for durations of ca. 100 a to ca. 10^3 mm/ka for ca. >3000 a.

The approach of Lehmann et al. (2019a) models synthetic erosion histories in both steady and transient states. Steady state erosion assumes a constant erosion rate throughout the duration of

surface exposure. Transient erosion is typical of shorter exposure histories where a steady state of erosion has not yet been reached. Transient erosion varies with time and was simulated here by assuming that the evolution of erosion in time follows a stepped function of fixed increases in erosion rates from zero for varying durations throughout the exposure history for each synthetic erosion history simulated. An illustration of this is provided by Fig. 7A where transient erosion rates of between ca. 10^4 mm/ka were inferred for a minimum duration of ca. ≤1 a, extending up to ca. 10^3 mm/ka for durations up to ca. 50 a. Beyond ca. 50 a, a steady state of erosion was reached at a constant erosion rate of ca. 10^3 mm/ka, represented by the flattening of the profile with the highest likelihood. Alternatively, a profile indicative of a transient state of erosion where no steady state has been established is illustrated by Fig. 7D where transient erosion rates of between ca. 10^2 mm/ka were inferred for a minimum duration of ca. ≤1 a, extending up to ca. 10^1 mm/ka for durations beyond ca. 200 a. This numerical approach (Lehmann et al. 2019a) allows erosion history to be considered as non-constant in time (i.e. transient), in addition to steady-state, and so it is more indicative of the stochastic erosional processes (driven by temperature, precipitation, snow cover, wind) in nature.

EC: So I think the paper needs major changes, but I do concur with the reviewers that the paper has merit and deserves publication once the problems are corrected.

A few other minor comments that I have:

EC: **Lines 153-158** – Were whole rocks or just portions collected in the field? Cores were drilled in the laboratory, but it is not clear how the rocks were collected.

AC: We have clarified this in the text in the Methods section. See below:

Portions of the original boulder or bedrock sample were collected in the field in daylight and immediately placed into opaque, black sample bags.

EC: **Line 196** – What do you mean by “similar”. You just mentioned fairly wide ranges in reduction.

AC: We have added further clarification to the text in response to this comment. See below:

This indicates that within our samples the minerals emitting the IRSL signals (i.e. K-feldspar) have similar inherent bleaching rates when exposed to longer durations of time (i.e. > 8 h in the solar simulator).

EC: **Line 578**. Figure 4 caption. What do you mean by “replicate” core? Replicates of what?

AC: We have added further clarification into the figure caption to help explain this.

Presented in age-order are the IRSL-depth profiles for each of the three replicate cores analysed per sample.

EC: **Lines 229-239** – I have seen surfaces of cores show complete saturation when nearby cores from the same rock did not. I am not sure we understand fully why this should be.

AC: Interesting, it is certainly puzzling. We have added further clarification in this section in response to Benjamin Lehmann's comments, and hopefully our discussion here helps to fuel future research to address these issues.

Erosion rates in a wet, temperate climate derived from rock luminescence techniques

Rachel K. Smedley[1], David Small[2], Richard S. Jones[2, 3], Stephen Brough[1], Jennifer Bradley[1], Geraint T.H. Jenkins[4]

[1] School of Environmental Sciences, University of Liverpool, Liverpool, UK.

[2] Department of Geography, Durham University, South Road, Durham, UK.

[3] School of Earth, Atmosphere and Environment, Monash University, Melbourne, Australia.

[4] Independent researcher: Powys, Wales, UK

Correspondence to: Rachel K. Smedley (rachel.smedley@liverpool.ac.uk)

Abstract

A new luminescence erosion-meter has huge potential for inferring erosion rates on sub-millennial scales for both steady and transient states of erosion, which is not currently ~~not~~ possible with any existing techniques capable of measuring erosion. This study applies new rock luminescence techniques to a well-constrained scenario provided by the Beinn Alligin rock avalanche, NW Scotland. Boulders in this deposit are lithologically consistent, have known cosmogenic nuclide ages, and independently-derived Holocene erosion rates. We find that luminescence-derived exposure ages for the Beinn Alligin rock avalanche were an order of magnitude younger than existing cosmogenic nuclide exposure ages, suggestive of high erosion rates (as supported by field evidence of quartz grain protrusions on the rock surfaces). Erosion rates determined by luminescence were consistent with independently-derived rates measured from boulder-edge roundness. Inversion modelling indicates a transient state of erosion reflecting the stochastic nature of erosional processes over the last ~4.5 ka in the wet, temperate climate of NW Scotland. Erosion was likely modulated by known fluctuations in moisture availability, and to a lesser extent temperature, which controlled the extent of chemical weathering of these highly-lithified rocks prior to erosion. The use of a multi-elevated temperature, post-infra-red, infra-red stimulated luminescence (MET-pIRIR) protocol (50, 150 and 225°C) was advantageous as it identified samples with complexities introduced by within-sample variability (e.g. surficial coatings). This study demonstrates that the luminescence erosion-meter can infer accurate erosion rates on sub-millennial scales and identify transient states of erosion (i.e. stochastic processes) in agreement with independently-derived erosion rates for the same deposit.

1. Introduction

Rock erosion is dependent upon a variety of internal (e.g. mineralogy, grainsize, porosity, structures) and external (e.g. temperature, moisture availability, snow cover, wind, aspect) factors. Chemical and/or physical weathering of rocks (or rock

decay; Hall et al. 2012) breaks down the surficial materials making them available for transportation (i.e. erosion), where the rates and processes of degradation is primarily controlled by the rock lithology (e.g. Twidale, 1982; Ford and Williams, 1989). For boulders with similar lithologies, the erosion rate is conditioned by weathering principally caused by moisture availability, but also temperature, and in some cases biological factors (Hall et al. 2012). It is widely reported that warmer temperatures increase most rates of chemical activity, while sub-zero temperatures arrest chemical activity on a seasonal basis. However, cold temperatures alone do not preclude chemical weathering (Thorn et al. 2001). As such, rock erosion rates will be sensitive to changing climate (moisture availability, temperature) such as that experienced throughout the Late Holocene (i.e. last 4 ka) (e.g. Charman, 2010), in addition to that forecast for the future due to anthropogenic climate change (e.g. Stocker et al. 2013).

Measuring erosion rates over shorter ($\leq 10^3$ a) and longer ($\geq 10^4$ a) integration times is advantageous as each targets a different phenomenon of erosion. Longer timeframes will inform on how landscapes respond to changing large-scale climatic and tectonic conditions (e.g. Herman et al. 2010), whereas shorter timeframes assess local or regional responses to shorter-lived environmental conditions (e.g. climate fluctuations). A number of techniques can constrain long-term, landscape erosion rates on $\geq 10^4$ a timeframes, such as cosmogenic nuclides (e.g. Lal,1991; Braun et al. 2006; Balco et al. 2008) or thermochronology (Reiners and Brandon, 2006). While observational measurements on very short timeframes $\leq 10^2$ a are performed with both direct contact (e.g. Hanna, 1966; High and Hanna, 1970; Trudgill et al. 1989) and non-contact (e.g. Swantesson, 1989; Swantesson et al. 2006) techniques. However, until now it has been difficult to constrain erosion rates on 10^2 to 10^3 a timeframes due to a lack of techniques with the required sensitivity and resolution.

The luminescence signal within mineral grains (quartz and feldspar) is reset when a rock surface is exposed to sunlight for the first time (e.g. Habermann et al. 2000; Polikreti et al. 2002; Vafiadou et al. 2007). With continued exposure the luminescence signal resetting in the mineral grains propagates to increasing depths (i.e. the luminescence depth profile is a function of time). Improved understanding of this fundamental principle has led to the development of new applications of luminescence; constraining the timing of rock exposure events (Laskaris and Liritzis, 2011; Sohbati et al. 2011; Lehmann et al. 2018) and rock surface erosion rates (Sohbati et al. 2018; Lehmann et al. 2019a,b). Brown (2020) ~~even~~ combine these phenomena within model simulations to explore different sample histories of exposure and burial, ~~to~~ informing geomorphological interpretations of luminescence depth profiles measured ~~for~~in samples collected from the natural environment. Here, we ~~measure~~ investigate erosion rates, rather than weathering rates as the luminescence technique specifically measures the light penetration into a rock surface after the removal of material (i.e. erosion), occurring after the in-situ rock breakdown (i.e. weathering). Luminescence depth profiles are a product of the competing effects of time (which allows the bleaching front to propagate to greater depths) and erosion (which exhumes the bleaching front closer to the surface). Existing studies have suggested that rock luminescence exposure dating is only feasible for very short timeframes (e.g. <300 a; Sohbati et al. 2018) as light penetrates faster than the material can be removed, and/or in settings where erosion rates are <1 mm/ka (Lehmann et al. 2018). Beyond this, the dominant control on the luminescence depth profile is erosion,

rather than time, hence if time can be parameterised, then erosion can be determined (and vice versa). Recent findings from erosion simulations compared with measured data have shown that the erosion rates derived from luminescence depth profiles can be accurate even where stochastic erosion was experienced in nature (Brown and Moon, 2019).

New luminescence techniques have the potential to derive 10^2 to 10^3 a scale erosion rates because of two important characteristics: (1) measurable luminescence depth profiles can develop in a rock surface over extremely short durations of sunlight exposure (e.g. days; Polikreti et al. 2003, or years; Lehmann et al. 2018); and (2) luminescence depth profiles are sensitive to mm-scale erosion. Conversely, cosmogenic nuclides are sensitive to m-scale erosion, depending on the density (e.g. Lal, 1991). Therefore, the new luminescence erosion-meter has the potential to provide a step-change in capabilities of measuring erosion rates on currently impossible 10^2 to 10^3 a timeframes. However, its application has been limited to few studies (e.g. Sohbati et al. 2018; Lehmann et al. 2019b) validated against long-term erosion rates of landscape evolution from global or regional datasets rather than local, independently-constrained erosion rates derived from the same rock type.

This study tests the accuracy and applicability of rock erosion rates inferred from luminescence techniques in a new latitudinal (57°N) and climate (wet, temperate) setting with independently-constrained erosion rates. The Beinn Alligin rock avalanche in NW Scotland (Fig. 1) provides a well-constrained test scenario as: (1) the boulders were sourced from a single fault-bounded failure scarp occurring within sandstones of the Torridonian group (i.e. rocks are likely to be lithologically consistent); (2) all boulder samples share an identical exposure history as they were deposited by a single, instantaneous event (Ballantyne and Stone, 2004); (3) independent cosmogenic exposure ages constrain the timing of the rock avalanche (Ballantyne and Stone, 2004); and (4) independently-derived erosion rates over the last ~4 ka for the boulders of the Beinn Alligin rock avalanche uniquely provide constraints on erosion rates (Kirkbride and Bell, 2010).

2. Theoretical background

The propagation of a bleaching front (i.e. the depth at which the luminescence signal has been reduced by 50 %) into a rock surface can be described by a double exponential function (Eq. 1), where L_x is the luminescence measured with depth (x) from the rock surface, L_0 is the saturation limit for this sample (determined experimentally), t is the exposure time, $\overline{\sigma\varphi_0}$ is the intensity of light of a specific wavelength at the rock surface, and μ is the light attenuation coefficient. To determine the exposure time (t) of a rock surface (and also erosion rates), it is necessary to parameterise μ and $\overline{\sigma\varphi_0}$, which are likely unique to any specific rock lithology and natural sunlight conditions (e.g. latitude, cloudiness) of the sample being dated, respectively. Therefore, to provide accurate luminescence exposure ages (and also~~or~~ erosion rates), μ and $\overline{\sigma\varphi_0}$ must be calibrated using samples of known-age with the same lithology and natural sunlight conditions (e.g. a nearby road-cutting).

$$L_x = L_0 e^{-\overline{\sigma\varphi_0} t e^{-\mu x}} \quad (1)$$

Studies have applied rock luminescence techniques (mostly exposure dating) to a variety of lithologies including granites, gneisses (Lehmann et al. 2018, 2019a,b; Meyer et al. 2019), sandstones (Sohbati et al. 2012; Chapot et al. 2012; Pederson et al. 2014), ~~and~~ quartzites (Gliganic et al. 2019) and carbonate limestone (Brill et al. 2021). These studies showed that μ is highly dependent upon the rock lithology, where mineralogy has a strong control on the rock transparency. This is supported

by direct measurements of μ for a variety of lithologies (greywacke, sandstone, granite, and quartzite) using a spectrometer (Ou et al. 2018). In addition to mineralogy, it has also been shown that the precipitation of dark Fe-hydroxides (Meyer et al. 2018) and rock varnishing (or weathering crusts) (e.g. Luo et al. 2019) can influence μ by changing the rock transparency principally at the rock surface. Mineralogy is broadly a constant variable over time. However, the formation of precipitates or rock varnishing can be time-variable due to changing environmental factors external to the rock; thus, we ~~must~~ should consider the possibility that μ may be time-variable. Consequently, investigating the rock opacity of each sample is important to assess whether the known-age samples used to parameterise μ and $\overline{\sigma\varphi_0}$ were consistent with the unknown-age samples used for exposure dating or erosion rates.

Since the introduction of the new rock luminescence techniques, most studies on K-feldspar (except Luo et al. 2019) have only utilised the IR_{50} signal as it bleaches more efficiently with depth into rock surfaces compared to higher temperature post-IR IRSL signals (e.g. Luo et al. 2019; Ou et al. 2018). However, electron multiplying charged coupled device (EMCCD) measurements of four rock types (quartzite, orthoclase and two different granites) have shown that the post-IR IRSL signals of rock slices were dominated by K-feldspars, while Na-rich feldspars can contribute towards the IR_{50} signal (Thomsen et al. 2018). It is possible that the different IRSL signals will have different luminescence characteristics (e.g. bleaching rates, fading rates, saturation levels, light attenuation, internal mineral composition) that could be exploited during measurements. Luo et al. (2019) used the post-IR IRSL signals with a multiple elevated temperature (MET) protocol (50, 110, 170, 225 °C) to demonstrate that all the IRSL signals provide luminescence depth profiles, but the lower temperature signals penetrated further into the rock with depth. The authors fit the four IRSL signals to improve the accuracy of their parameterisation of μ and $\overline{\sigma\varphi_0}$. However, no study has yet used the MET-post IR IRSL protocol to exploit the differing luminescence characteristics of the ~~simultaneously~~successively-measured IRSL signals to provide an internal quality control check on the reliability of the measured data, i.e. the luminescence depth profile will penetrate deeper in to the rock for the IR_{50} signal than the $pIRIR_{150}$ signal, which in turn will penetrate deeper than the $pIRIR_{225}$ signal. However, all three signals should determine the same erosion rates if the model parameterisation (i.e. μ and $\overline{\sigma\varphi_0}$) is accurate. To maximise the potential information that could be derived from the samples, this study applied a MET-post IR IRSL protocol (50, 150 and 225 °C).

For determining erosion rates for rock surfaces of known exposure age, Sohbati et al. (2018) used a confluent hypergeometric function to provide an analytical solution, but assuming only steady-state erosion. Lehmann et al. (2019a) provide a numerical approach that exploits the differential sensitivities to erosion of the luminescence (short-term) and cosmogenic nuclide (longer-term) techniques to erosion to infer erosion histories (steady state and transient over time) for rock surfaces. ~~By applying a step function from zero to increased constant erosion rates at certain times in history,~~ This approach uses the experimental data from the luminescence depth profiles and the ^{10}Be concentrations for each sample. Modelling of the luminescence depth profiles accounts for the electron trapping dependent upon the environmental dose-rate and D_0 but does not consider athermal loss of the signal (i.e. anomalous fading) as it has been demonstrated to have a

negligible impact upon the luminescence depth profiles (Lehmann et al. 2019a). Modelling of the ^{10}Be concentrations assumes ~~that~~ no inheritance of ~~the~~ cosmogenic nuclides from prior exposure ~~has occurred~~, and that the ^{10}Be concentrations have been corrected for ~~the~~ sample depth, ~~sample~~and ~~-~~density and topographical shielding~~. local production rates, and the sample location (longitude, latitude and elevation).~~ The luminescence depth profiles and c~~The combined experimental data for the luminescence depth profiles and C~~cosmogenic nuclide concentrations~~s~~ are solved simultaneously for two unknowns: the exposure ~~age~~duration and the erosion ~~rate~~history as defined by a step function (e.g. zero erosion for an initial period of time followed by an instant increase to a constant erosion rate). Forward modelling is used to calculate all of the possible ~~combinations of~~ luminescence depth profiles ~~and ^{10}Be concentrations~~ for these synthetic erosion and exposure histories, which are then validated using inversion models against the experimental data to determine the combinations with the highest likelihood. A forbidden zone is ~~determined~~defined ~~where the~~by ~~range of possible solutions~~combinations of erosion rate~~s~~ and duration~~s~~ that ~~are in excess of those that~~ are ~~feasible~~not possible given ~~for~~ the ~~experimental~~measured ^{10}Be concentrations ~~provided for the sample~~; these solutions are excluded from the parameter ranges used for the inversion model. For example, the forbidden zone identified in the inversion model profile shown in Fig. 7A is restricted to ranges from ca. 10^4 mm/ka for durations of ca. 100 a to ca. 10^3 mm/ka for ca. >3000 a.

The approach of Lehmann et al. (2019a) can model~~s~~ synthetic erosion histories in both steady and transient states. Steady state erosion ~~assumes~~is defined as a constant erosion rate over a portion of ~~throughout~~ the ~~duration~~total duration of surface exposure. Transient erosion is typical of shorter exposure histories where a steady state of erosion has not yet been reached and is defined by erosion rates that decrease linearly with increased timing of erosion onset within the parameter space ~~Transient erosion varies with time and was simulated here by assuming that the evolution of erosion in time follows a stepped function of a fixed increase in erosion rate from zero for varying durations throughout the exposure history for each synthetic erosion history simulated~~. An illustration of this is provided by Fig. 7A where transient erosion rates of between ca. 10^4 mm/ka were inferred for a minimum duration of ca. ≤1 a, and extending up to ca. 10^3 mm/ka for durations up to ca. 50 a. Beyond ca. 50 a, a steady state of erosion was reached at a constant erosion rate of ca. 10^3 mm/ka, represented by the flattening of the profile with the highest likelihood. Alternatively, a profile indicative of a transient state of erosion where no steady state has been established is illustrated by Fig. 7D where transient erosion rates of between ca. 10^2 mm/ka were inferred for a minimum duration of ca. ≤1 a, and extending up to ca. 10^1 mm/ka for durations beyond ca. 200 a. T~~t~~his numerical approach (Lehmann et al. 2019a) allows erosion history to be considered as non-constant in time (i.e. transient), in addition to steady-state, and so it is more indicative of the stochastic erosional processes (driven by temperature, precipitation, snow cover, wind) in nature.

3. The Beinn Alligin rock avalanche

Today, average winter and summer temperatures in NW Scotland are 7°C and 18°C, respectively, while average annual precipitation (mostly rainfall) is high (ca. 2,300 mm/a) (Met Office, 2021). The Beinn Alligin rock avalanche (57°35'N, 05°34'W) is a distinct, lobate deposit of large boulders that is 1.25 km long and covers an area of 0.38 km^2 (Fig. 1). It has

previously been ascribed various origins including a rockslide onto a former corrie glacier (e.g. Ballantyne, 1987; Gordon, 1993) and a former rock glacier (Sissons, 1975; 1976). However, on the basis of cosmogenic exposure dates that constrain its deposition to the ~~Middle to~~ Late Holocene it is now widely accepted to have been deposited by a rock-slope failure that experienced excess run-out (e.g. a rock avalanche). The source is a distinct, fault-bounded failure scar on the southern flank of Sgurr Mor, the highest peak of Beinn Alligin (Ballantyne, 2003; Ballantyne and Stone, 2004). The rock avalanche is comprised of large, poorly-sorted boulders and is calculated to comprise a total volume of 3.3 – 3.8 x 10^6 m^3, equivalent to a mass of 8.3 – 9.5 Mt (Ballantyne and Stone, 2004). The source lithology is Late Precambrian Torridonian sandstone strata. The Torridonian sandstones are reddish or reddish brown terrestrial sedimentary rocks deposited under fluvial or shallow lake conditions (Stewart, 1982). The sandstones maintained a common origin throughout deposition (Stewart, 1982) and are thus largely consistent in mineralogy (dominated by quartz, and alkali and plagioclase feldspar) although there are some local variations in grain size (Stewart and Donnellan, 1992).

The ^{10}Be concentrations of three boulders used for cosmogenic nuclide exposure dating were internally consistent evidencing a single, catastrophic mass movement event which occurred 4.54 ± 0.27 ka (re-calculated from Ballantyne and Stone, 2004). Consequently, the boulders were very unlikely to have previously been exposed to cosmic rays or sunlight prior to transport and deposition. Moreover, the large size of the flat-topped boulders (>2 x 2 x 2 m) and lack of finer sediment matrix within the rock avalanche deposit, suggested that post-depositional movement or exhumation is unlikely. The Torridonian sandstones are hard, cemented rocks (Stewart, 1984; Stewart and Donnellson, 1992) susceptible to granular disintegration (e.g. Ballantyne and Whittington, 1987). Given its inland location, salt weathering is likely negligible. Kirkbride and Bell (2010) estimated edge-rounding rates of ~3.3 mm/ka for a suite of Torridonian sandstone boulder samples from a range of sites in NW Scotland under the warmer, wetter climates of the Holocene. A notably higher erosion rate of 12 mm/ka was specifically determined for the Beinn Alligin rock avalanche. Kirkbride and Bell (2010) suggest that this higher erosion rate, in comparison to the other sites, is likely due to inherited rock roundness caused by abrasion during the high-magnitude depositional event. Additionally, minor differences in lithology cannot be ruled out (e.g. Twidale, 1982; Ford and Williams, 1989). Consequently, we consider the range ~3.3 to 12 mm/ka as a reasonable estimation of the Holocene erosion rate of the Torridonian sandstone boulders that comprise the Beinn Alligin rock avalanche.

4. Methods

A total of six rock samples were taken from the Torridonian sandstones in NW Scotland (Fig. 1). Three samples were taken from three different road-cuttings of known age to calibrate the values of μ and $\overline{\sigma\varphi_0}$: ROAD01 (0.01 a), ROAD02 (57 a; Fig. S1a), ROAD03 (44 a; Fig. S1b). Three further samples were taken from flat-topped, angular boulders that were part of the Beinn Alligin rock avalanche deposit: BALL01, BALL02 and BALL03 (Fig. 1D). Portions of the original boulder or bedrock sample~~Samples~~ were collected in the field in daylight and immediately placed into opaque, black sample bags. All samples were taken from surfaces perpendicular to incoming sunlight to ensure that the daylight irradiation geometry was similar between calibration and dating samples (cf. Gliganic et al. 2019).

4.1 Luminescence measurements

To calculate the environmental dose-rate throughout burial for each sample (Table 1), U, Th and K concentrations were measured for ca. 80 g of crushed bulk sample using high-resolution gamma spectrometry. Internal dose-rates were calculated assuming an internal K-content of 10 ± 2 % (Smedley et al. 2012) and internal U and Th concentrations of 0.3 ± 0.1 ppm and 1.7 ± 0.4 ppm (Smedley and Pearce, 2016), in addition to the~~using~~ measured average grain sizes for each sample. Cosmic dose-rates were calculated after Prescott and Hutton (1994). For measuring the luminescence depth profiles, sample preparation was performed under subdued-red lighting conditions to prevent contamination of the luminescence signal. Rock cores ~7 mm in diameter and up to 20 mm long were drilled into the rock surface using an Axminster bench-top, pillar drill equipped with a water-cooled, diamond-tipped drillbit (~9 mm diameter). Each core was sliced at a thickness of ~0.7 mm using a Buehler IsoMet low-speed saw equipped with a water-cooled, 0.3 mm diameter diamond-tipped wafer blade. All slices were then mounted in stainless steel cups for luminescence measurements.

Luminescence measurements were performed on a Risø TL/OSL reader (TL-DA-15) with a $^{90}Sr/^{90}Y$ beta irradiation source. Heating was performed at 1°C/s and the rock slices were held at the stimulation temperature (i.e. 50, 150 and 225°C) for 60 s prior to IR stimulation to ensure all of the disc was at temperature before stimulating (cf. Jenkins et al. 2018). IRSL signals were detected in blue wavelengths using a photo-multiplier tube fitted with Schott BG-39 (2 mm thickness) and Corning 7-59 (2 mm thickness) filters. A MET-post-IR IRSL sequence (Table S1) was used to determine IRSL signals at three different temperatures (50, 150 and 225°C) ~~simultaneously~~successively, hereafter termed the IR_{50}, $pIRIR_{150}$ and $pIRIR_{225}$ signals. ~~OSL~~Luminescence depth profiles were determined for each core by measuring the natural signal (L_n) normalised using the signal measured in response to a 53 Gy test-dose (T_n), hereafter termed the L_n/T_n signal. The IRSL signal was determined by subtracting the background signal (final 20 s, 40 channels) from the initial signal (0 – 3.5 s, 7 channels). The large test-dose (53 Gy) was used to reduce the impact of thermal transfer/incomplete resetting of the IRSL signal between measurements (after Liu et al. 2016).

D_e values were determined for the shallowest disc and the deepest disc from one core of each sample to quantify the natural residual dose and saturation limit (L_0, Eq. 1), respectively. Fading rates (*g*-values, Aitken 1985) were determined for three discs of each sample and normalised to a t_c of two days (Huntley and Lamothe 2001). The weighted mean and standard error of the g-values for all discs were 3.7 ± 0.4 %/dec. (IR_{50}), 1.0 ± 0.5 %/dec. ($pIRIR_{150}$) and 1.0 ± 0.5 %/dec. ($pIRIR_{225}$). The large uncertainties on the individual *g*-values measured were derived from uncertainty in the fit of the data, which is typical of fading measurements (e.g. Smedley et al. 2016). The fading rates were in line with previous measurements of IRSL signals (e.g. Roberts 2012; Trauerstein et al. 2014; Kolb and Fuchs 2018). Lehmann et al. (2019a) performed sensitivity tests of the shape of the luminescence depth profiles (IR_{50}) with a high and low g-value end-members and these simulations demonstrated that athermal loss of signal has a minimal impact upon the IRSL depth profile shape; thus, athermal loss (i.e. fading rates) was not considered in calculations.

Previous studies have shown that the IR_{50} signal bleached faster than the pIRIR signals (Smedley et al., 2015). To test the inherent bleaching rates of the feldspars in our samples, artificial bleaching experiments were performed on seven discs from all six samples (n.b. these experiments do not test for variations in light attenuation with depth). All previously-analysed discs were given a 105 Gy dose, then subjected to different exposure times in a solar simulator (0 m, 1 m, 10 m, 30 m, 1 h, 4 h and 8 h) and the normalised luminescence signals (IR_{50}, $pIRIR_{150}$ and $pIRIR_{225}$) were measured (Fig. S~~1~~2). The results show some variations after 1 m of solar simulator exposure. However, luminescence signals reduced to 2 – 6 % (IR_{50}), 6 – 11 % ($pIRIR_{150}$) and 14 – 22 % ($pIRIR_{225}$) of the unexposed light levels after 1 h and 1 – 2 % (IR_{50}), 2 – 3 % ($pIRIR_{150}$) and 4 – 7 % ($pIRIR_{225}$) after 8 h. This indicates that within our samples the minerals emitting the IRSL signals (i.e. K-feldspar) have similar inherent bleaching rates when exposed to longer durations of time (i.e. > 8 h in the solar simulator).

4.2 Rock composition

After luminescence measurements were performed, each rock slice (e.g. Fig. 2) was analysed to investigate potential changes in rock composition with depth (inferred by opacity and grainsize). The average down-core grainsize of each sample was measured under an optical microscope using *Infinity Analyze*. For each rock slice of an example core per sample, ten randomly-selected grains were measured and the mean and standard deviation grainsize were calculated per core and plotted against the core depths (Fig. 3B). Down-core red-green-blue (RGB) values were determined for each sample to investigate whether there was any colour variation within the sample, and externally between samples; thus, providing a semi-quantitative tool to detect variability in rock opacity (Meyer et al. 2018). Raster images of RGB were obtained for each rock slice using an EPSON Expression 11000XL flatbed scanner at 1200 dpi resolution (e.g. Fig. S3~~2~~). Mean and standard deviations of the RGB values (e.g. Fig. 3A) for each rock slice were calculated using the *raster* package in R (version 2.9-23; Hijmans, 2019).

5. Results

5.1 Luminescence depth profiles

The luminescence depth profiles (IR_{50}, $pIRIR_{150}$ and $pIRIR_{225}$) (Fig. 4) record bleaching fronts caused by sunlight exposure for all of the known-age samples. The luminescence depth profile measured for core 3 of sample ROAD02 (Fig. 4 ~~g,h,j~~G,H,J) was inconsistent with cores 1 and 2, giving high standard deviation values for the IR_{50} (1.2), $pIRIR_{150}$ (1.1) and $pIRIR_{225}$ (0.9) signals; thus, core 3 was removed from subsequent analysis (likely sample preparation issues related to drilling preservation of the weathered surface). The luminescence depth profiles for the remaining replicate cores for all three samples were broadly consistent within each rock sample with mean standard deviations ranging from 0.2 – 0.8.

The luminescence depth profiles (Fig. 4) for the IR_{50} signal were consistent with the increasing sunlight exposure ages for ROAD01 (0.01 a), ROAD03 (44 a) and ROAD02 (57 a), with bleaching fronts at ~~2.5~~0.75 mm, 4.~~5~~00 mm and 4.7~~6.~~5 mm, respectively (Fig. S5~~4~~a). This indicated that the depth of the IR_{50} bleaching front was dominated by exposure duration for the known-age samples as expected. Similarly, the $pIRIR_{150}$ and $pIRIR_{225}$ bleaching fronts were shallower in sample

ROAD01 (0.751.5 mm) compared to ROAD02 and ROAD03 (2.5.00 – 33.500 mm), reflecting the younger exposure duration of ROAD01. However, the $pIRIR_{150}$ and $pIRIR_{225}$ bleaching fronts were at similar depths (23.75 and 3.00 mm and 2.005 and 2.50 mm respectively) for both ROAD02 (57 a) and ROAD03 (44 a). This suggests that either another factor is influencing light penetration with depth in these rocks (e.g. small differences in the orientation of the sampled rock faces; Fig. S1) or that the pIRIR signals cannot resolve between a 57 a and 44 a exposure history (difference of only 13 a). Note that the inferred models shown in Fig. 4 were fitted using the $\overline{\sigma\varphi_0}$ and μ values included in each figure. See Section 5.2 for further explanation of the estimation of the model parameters.

The luminescence depth profiles measured for the unknown-age samples BALL02 and BALL03 using the IR_{50}, $pIRIR_{150}$ and $pIRIR_{225}$ signals (Fig. 5) recorded bleaching fronts caused by sunlight exposure. Conversely, the luminescence depth profile for sample BALL01 had saturated IRSL signals throughout the core and did not display any evidence of IRSL signal resetting with depth (Fig. 5aA-Ce). A luminescence depth profile measured for a core drilled into the bottom surface (Bottom C1; Fig. 5Aa-eC) confirmed that the bottom surface of BALL01 was also saturated. The lack of a bleaching front in sample BALL01 is difficult to explain as the sample was taken in daylight and had seemingly identical characteristics to samples BALL02 and BALL03 (i.e. no lichen-cover or coatings preventing light penetration in the rock). Although all the samples were similar in colour/opacity (Fig. 3Aa), the surface of sample BALL01 was coarser grained than BALL02 and BALL03 (Fig. 2; Fig. 3Bb). Studies have shown that coarser grain sizes are more susceptible to mechanical weathering via grain detachment induced by chemical weathering (Israelli and Emmanuel, 2018).; tThus, although care was taken when sampling to mark the surface of the rock and to measure the length of the rock cores before and after slicing, it is possible that the luminescence depth profile (likely <10 mm based on BALL02 and BALL03) was lost during sampling and/or sample preparation due to the presence of a fragile weathering crust, potentially with a sub-surface zone of weakness (e.g. Robinson and Williams, 1987). Furthermore, field observations showed the presence of a rock pool on the surface of the boulder sampled for BALL01, which is not present on BALL02 band BALL03 (Fig. 1De); thus, there is also potential that the surface sampled for BALL01 had experienced enhanced chemical weathering via trickle paths draining the rock pool. These are commonly linked to a greater density of micro-cracks in the uppermost mm's millimetres of the rock (Swantesson, 1989, 1992). Consequently, we did not derive exposure ages or erosion rates from BALL01. Where rock pools are likely on boulders, the highest rock surface should be sampled for luminescence techniques to avoid the potential for pooling or trickle paths.

5.2 Estimation of model parameters

To determine an apparent exposure age or erosion rate from the measured luminescence depth profiles, the variables that control the evolution of a luminescence depth profile in a rock surface must be parameterised; specifically, the dose-rate ($\dot{D}$) (see Section 4.1), saturation level (D_0), $\overline{\sigma\varphi_0}$ and μ. D_0 was determined experimentally from saturated dose-response curves measured for the deepest rock slices of each sample. $\overline{\sigma\varphi_0}$ and μ were calibrated using Eq. (1) and the known-age samples (ROAD01, ROAD02 and ROAD03) of similar, suitable rock composition as determined by the down-core profiles of RGB

and grainsize (Section 4.2). Note that ($\dot{D}$) is not considered in Eq. (1) but is used to determine an apparent exposure age or erosion rate and so needs to be measured for each sample (see Section 2). Down-core RGB values for all samples were internally consistent (Fig. 3~~a~~A) as indicated by the relative standard deviation (RSD) range between 8 and 12 %. The down-core RGB values were also externally consistent between all samples (Fig. 3A~~a~~), with the exception of the slightly darker-coloured sample ROAD01. However, measurements of grainsize (Fig. 3~~b~~B) showed that the known-age sample ROAD02 (90 ± 23 µm) had a similar grainsize to the unknown-age samples BALL02 (73 ± 18 µm) and BALL03 (98 ± 19 µm), whereas ROAD01 (42 ± 9 µm) and ROAD03 (168 ± 56 µm) were finer and coarser grained, respectively. Given the similarity in colour and grain-size, it was considered most appropriate to calibrate $\overline{\sigma\varphi_0}$ and µ for the unknown age samples (BALL02 and BALL03) using known-age sample ROAD02.

The values of $\overline{\sigma\varphi_0}$ and µ were determined by fitting Eqn. (1) using the approach of Lehmann et al. (2019a). The inferred model (Eq. 1) had a good fit to the measured data for all samples and signals (Fig. 4) and µ and $\overline{\sigma\varphi_0}$ were calculated (Table 2; Fig. 6). For ROAD01, the parameters determined using the IR_{50} (µ = 3.2 mm^{-1}, $\overline{\sigma\varphi_0}$ = 2.80e^{-4} s^{-1}), $pIRIR_{150}$ (µ = 3.1 mm^{-1}, $\overline{\sigma\varphi_0}$ = 3.27e^{-5} s^{-1}) and $pIRIR_{225}$ (µ = 3.0 mm^{-1}, $\overline{\sigma\varphi_0}$ = 2.88e^{-5} s^{-1}) signals were broadly consistent. For ROAD02, the parameters differed between the IR_{50} (µ = 2.1 mm^{-1}, $\overline{\sigma\varphi_0}$ = 6.67e^{-6} s^{-1}), $pIRIR_{150}$ (µ = 1.5 mm^{-1}, $\overline{\sigma\varphi_0}$ = 1.73e^{-8} s^{-1}) and $pIRIR_{225}$ (µ = 2.8 mm^{-1}, $\overline{\sigma\varphi_0}$ = 9.01e^{-8} s^{-1}) signals, but the values for each signal were broadly similar to the equivalent values determined for ROAD03 using the IR_{50} (µ = 2.7 mm^{-1}, $\overline{\sigma\varphi_0}$ = 1.56e^{-5} s^{-1}), $pIRIR_{150}$ (µ = 1.5 mm^{-1}, $\overline{\sigma\varphi_0}$ = 3.80e^{-8} s^{-1}) and $pIRIR_{225}$ (µ = 1.4 mm^{-1}, $\overline{\sigma\varphi_0}$ = 1.70e^{-8} s^{-1}) signals. Given the similarity of $\overline{\sigma\varphi_0}$ and µ determined using all three IRSL signals for ROAD02 and ROAD03 and the difference in grainsizes (Fig. 3B), it suggests that grainsize has a minimal impact upon the attenuation of light into a rock surface in comparison to other factors (e.g. mineralogy, surficial coatings). The µ values for samples ROAD01, ROAD02 and ROAD03 determined using the IR_{50} signal in this study were comparable to µ values in existing literature for sandstones using K-feldspar e.g. ~~µ = 1.01 mm^{-1} where $\overline{\sigma\varphi_0}$ = 6.80e^{-9} s^{-1} (Sohbati et al. 2012) and~~ 3.06 mm^{-1} (Ou et al. 2018). For sample ROAD01, µ and $\overline{\sigma\varphi_0}$ were similar for all three IRSL signals with large uncertainties (Fig. 6A~~a~~-~~c~~C) which is likely related to the shorter exposure age of this sample (0.01 a). The finer grain size and darker rock opacity of sample ROAD01 in comparison to ROAD02 and ROAD03 likely explained the larger values of µ (i.e. greater light attenuation with depth into the rock surface).

5.3 Apparent exposure ages and erosion rates

Luminescence exposure ages were determined from the luminescence depth profiles using µ and $\overline{\sigma\varphi_0}$ derived from sample ROAD02 for each of the IRSL signals (Table 3). For BALL03, the IR_{50} (3~~7~~87 ± 10315 a^{-1}), $pIRIR_{150}$ (2964 ± ~~61~~54 a^{-1}) and $pIRIR_{225}$ (3~~70~~62 ± 4~~6~~9 a^{-1}) signals all gave luminescence exposure ages in agreement within uncertainties. For BALL02, the three signals were inconsistent with one another. The $pIRIR_{225}$ signal (2~~79~~63 ± ~~48~~30 a^{-1}) was consistent with BALL03, but the IR_{50} (~~8~~9 ± ~~2~~3 a^{-1}) and $pIRIR_{150}$ (~~70~~66 ± ~~9~~16 a^{-1}) signals for BALL02 were younger than BALL03. All apparent exposure ages based on the different luminescence signals were at least one order of magnitude younger than the apparent exposure age based cosmogenic nuclide dating (4.54 ± 0.27 ka; Ballantyne and Stone, 2004). This was likely because erosion over

time in this wet, temperate climate has removed material from the surface of the rock and created shallower luminescence depth profiles in comparison to a non-eroding profile; thus, the luminescence depth profile is dependent upon both exposure age and the erosion rate (Sohbati et al. 2018; Lehmann et al. 2019a).

To test whether erosion rates could be determined for the Beinn Alligin boulders from the luminescence depth profiles, we performed erosion rate modelling following the inversion approach of Lehmann et al. (2019) and constrained by the re-calculated cosmogenic nuclide age (Ballantyne and Stone, 2004). This approach defines an erosion history that follows a step function with an initial period of zero erosion, followed by an immediate increase to a constant erosion rate at a defined time. It attempts to recover parameter combinations (erosion rate and timing of erosion initiation) that are both consistent with the cosmogenic nuclide concentration and produce modelled luminescence profiles that match observations. For ~~sample~~ BALL02, both the IR_{50} and $pIRIR_{150}$ signals suggested that the system had approached a steady-state with erosion rates of 66 mm/ka (IR_{50}) and 9 mm/ka ($pIRIR_{150}$) applied over time periods >73 a and 593 a, respectively. However, the $pIRIR_{225}$ signal suggested a transient erosion state, where the luminescence signal could be derived from numerous pairs of erosion rates and initiation times from a maximum erosion rate of 310 mm/ka over a minimum time interval of 4 a to a minimum erosion rate of 12 mm/ka over a minimum time interval of 90 a. All three IRSL signals from sample BALL03 consistently suggested a system undergoing a transient response to erosion, which was consistent with the $pIRIR_{225}$ signal of BALL02 (Fig. 7, Table 3). The IR_{50} signal for BALL03 derived a maximum erosion rate of 460 mm/ka over a minimum time interval of 3 a and a minimum erosion rate of 6 mm/ka over a minimum time interval of 231 a. The $pIRIR_{150}$ signal for BALL03 derived a maximum erosion rate of 100 mm/ka over minimum time interval of 19 a and a minimum erosion rate of 14 mm/ka over a minimum time interval of 137 a. The $pIRIR_{225}$ signal for BALL03 derived a maximum erosion rate of 180 mm/ka over a minimum time interval of 4 a and a minimum erosion rate of 11 mm/ka over a minimum time interval of 73 a.

At face value, the fit of the inferred erosion model to the experimental data for BALL02 using the IR_{50} (Fig. 5D) and $pIRIR_{150}$ (Fig. 5E) signals is better than the equivalent fits for BALL02 using the $pIRIR_{225}$ signal (Fig. 5F) and BALL03 using the IR_{50} (Fig. 5G), $pIRIR_{150}$ (Fig. 5H) and $pIRIR_{225}$ (Fig. 5I) signals. In the latter cases, the inferred erosion model is shallower than the experimental data. This could suggest that the $\overline{\sigma\varphi_0}$ and μ values were inaccurate, i.e. the attenuation of light with depth into the rock surface is lower in BALL02 ($pIRIR_{225}$ signal) and BALL03 (IR_{50}, $pIRIR_{150}$ and $pIRIR_{225}$ signals) than estimated by ROAD02. A possible explanation for this is that the surface of the roadcut sampled by ROAD02 (Fig. S1a) was orientated slightly differently to the Beinn Alligin rock avalanche boulders sampled by BALL02 and BALL03 (Fig. 1D), relative to the incoming sunlight (e.g. Gliganic et al. 2019). However, if the orientation of the known-age roadcut samples was even slightly inconsistent with the unknown samples, we would expect these inconsistencies to manifest similarly in all three MET signals for BALL02 and BALL03, which was not observed here. A factor that is common to ~~all~~ the less well~~poorly~~ fitting profiles ~~that are less well fit by the inferred erosion model~~ is that they ~~determined~~define transient erosion ~~rates~~states. This suggests that these surfaces experienced complex erosional histories over time whereby the erosion rate was time-varying. Consequently, it is possible that surficial weathering products may have

changed in thickness and composition over time, which in turn could slightly vary the attenuation of light (Meyer et al. 2018; Luo et al. 2018), meaning that the calibration of $\overline{\sigma\varphi_0}$ and μ from ROAD02 here introduced uncertainty into the inferred erosion model as it was not time-varying. It is also possible that sample-specific measurements of $\overline{\sigma\varphi_0}$ and μ (e.g. Ou et al. 2018), rather than calibration from known-age samples, could reduce the uncertainty introduced by time-varying light attenuation. However, further investigation is required into the physical mechanisms of time-varying light attenuation in the context of surficial weathering and subsequent erosion, and the impacts upon inferred transient erosion rates.

6. Discussion

6.1 Luminescence depth profiles ~~at~~ for the Beinn Alligin rock avalanche

Despite the similarity in rock opacity, grain ~~-~~size, aspect and exposure history, the luminescence depth profiles for samples BALL02 and BALL03 from the Beinn Alligin rock avalanche were inconsistent (Fig. 5). We consider it unlikely that this lack of consistency was caused by local variations in erosion rates (e.g. due to microclimate, aspect etc; Hall et al. 2005, 2008) as there were discrepancies between all three IRSL signals of BALL02. We would expect local erosion rate variations between samples to be consistently recorded across each of the IRSL signals, assuming the model parameterisation (μ and $\overline{\sigma\varphi_0}$) were accurate. Specifically, and with all other things being equal, a locally-variable erosion rate would translate the bleaching front(s) closer to the rock surface by a proportionally consistent amount for each signal of a given sample.

Analysis of the rock opacity with depth (Section 4.2; Meyer et al. 2018) showed that sample BALL02 was more positively skewed towards darker colours than ROAD02 and BALL03 (Fig. S3~~2~~, S~~3~~4), with higher surficial values caused by Fe-staining. Fe-staining can occur on rock surfaces with seasonal rock pools and trickle paths (Swantesson, 1989, 1992). The presence of a thin Fe-coating (<1 mm) on the rock surface would have changed the intensity and wavelength of the net daylight flux received by individual grains (e.g. Singhvi et al.,1986; Parish, 1994) and likely increased light attenuation with depth (e.g. Meyer et al. 2018; Luo et al. 2018). Consequently, the parameterisation of μ and $\overline{\sigma\varphi_0}$ derived from sample ROAD02 would be inaccurate for BALL02. Interestingly, the similarity between BALL02 and BALL03 for the $pIRIR_{225}$ signal suggests that the presence of an Fe-coating altered ~~may have preferentially attenuated the wavelengths that influence~~ the attenuation of the IR_{50} and $pIRIR_{150}$ signals to a lesser extent than~~, and not~~ the $pIRIR_{225}$ signal, but the reasons for this requires further investigation. The application of the MET-pIRIR rather than just the stand-alone IR_{50} signal protocol provided a major advantage as it identified samples where the parameterisation of μ and $\overline{\sigma\varphi_0}$ from known-age samples was complicated by factors such as surficial weathering coatings. Beyond this, it is possible that the MET-pIRIR protocol may be useful in identifying complex burial or exposure histories of rocks, similar to those that have been reported in previous studies but solely using the IR_{50} signal (e.g. Freiesleben et al. 2015; Brill et al. 2021). There is also potential to explore whether the different temperature IRSL signals of the MET protocol record different states of erosion (i.e. steady or transient states) within the same rock surface, whereby the post-IR IRSL signals that are attenuated greater would be more susceptible

to transient states of erosion in comparison to the lower temperature signals, which measure luminescence depth profiles to greater depths within the rock surface.

The boulders from the Beinn Alligin rock avalanche have been subject to a temperate climate for the last ~4 ka. The luminescence depth profiles from the boulders demonstrated that on these timeframes and under these climatic conditions the technique was an erosion-meter, rather than a chronometer, as expected (Sohbati et al. 2018; Lehmann et al. 2019a). Lehmann et al. (2018~~9~~a) noted that two of their samples, uncorrected for erosion, gave apparent luminescence exposure ages of ca. 640 a and <1 a compared to apparent ~~TCN~~ cosmogenic nuclide ages of ca. 16.5 ka and 6.5 ka, respectively. It has thus been inferred that erosion rates >1 mm/ka can make interpretation of luminescence depth profiles in terms of an exposure age difficult without accurately constraining the erosion rate (Sohbati et al., 2018; Lehmann et al., 2018). This is consistent with the underestimation of luminescence exposure ages measured here for the Beinn Alligin rock avalanche (Table 3), which have been independently-dated to 4.54 ± 0.27 ka using cosmogenic nuclides (Ballantyne and Stone, 2004). Consequently, luminescence depth profiles for the Beinn Alligin rock avalanche can only be inferred in terms of erosion rates.

6.2 Luminescence as an erosion-meter

The numerical approach of Lehmann et al. (2019a) exploits the different sensitivities of the luminescence (short-term) and cosmogenic nuclide (longer-term) techniques to erosion to infer erosion histories (steady state and transient over time) for rock surfaces. Their modelling shows that the higher erosion rates (>100 mm/ka) can only be sustained over shorter time durations (up to decadal) while at the same time being consistent with cosmogenic nuclide measurements. For BALL03, transient erosion rates were derived using the IR_{50} (6 - 460 mm/ka), $pIRIR_{150}$ (14 - 100 mm/ka) and $pIRIR_{225}$ (11 - 180 mm/ka) signals. These modelled transient erosion rates were broadly comparable to erosion rates inferred from luminescence depth profiles over comparable timeframes in previous studies: (i) rates between <0.038 ± 0.002 and 1.72 ± 0.04 mm/ka for glacial boulders and landslides (granite gneiss, granodorite and quartzite) in the Eastern Pamirs, China (Sohbati et al. 2018); and (ii) between 3.5 ± 1.2 mm/ka and 4,300 ± 600 mm/ka for glacially-modified, granitic bedrock in the French Alps (Lehmann et al., 2019b). This latter study modelled higher erosion rates (>100 mm/ka) over timescales from 10^1 to 10^3 a and lower erosion rates (<100 mm/ka) over longer time scales of 10^3 to 10^4 a. However, this comparison between modelled erosion rates does not account for the primary role that lithology has on weathering (e.g. Twidale, 1982; Ford and Williams, 1989). The sampled boulders in our study were composed of Torridonian sandstone, which has been reported to undergo granular disintegration (e.g. Ballantyne and Whittington, 1987), particularly around edges, and thus may have experienced higher erosion rates than the crystalline rocks (e.g. gneiss, granite) used in the studies of Sohbati et al. (2018) and Lehmann et al., 2019b.

A major advantage of applying this new erosion-meter technique to boulders of the Beinn Alligin rock avalanche was the existing constraints on Holocene erosion rates (~3.3 to 12 mm/ka) for Torridonian sandstones in NW Scotland inferred from boulder edge roundness measurements (Kirkbride and Bell, 2009). The long-term erosion rates inferred from luminescence depth profiles were consistent with the estimates provided by measuring the boulder-edge roundness, when

considering the differing approaches and assumptions of each method. Firstly, the sampling approach for the luminescence depth profiles targeted the flat-top surface of the boulders where granular disintegration would have been reduced relative to the boulder edges and corners. Thus, the boulder-edge roundness based erosion rates provided an upper constraint on the long-term erosion rate experienced by the boulders. Finally, the boulder-edge roundness measurements assumed steady-state erosion and could not identify the potential for a transient state of erosion, whereas the approach of Lehmann et al. (2019a,b) inferred some transient state of erosion (Table 3). Consequently, it is notable that the lower range of the transient erosion rates derived here using the IR_{50} (6 - 460 mm/ka), $pIRIR_{150}$ (14 - 100 mm/ka) and $pIRIR_{225}$ (11 - 180 mm/ka) signals were broadly consistent with the steady-state erosion rate derived from boulder edge roundness measurements for the Torridonian sandstones (in the range of ca. 3.3 to 12.0 mm/ka). Lehmann et al. (2019b) noted that their modelled steady-state erosion rates were one to two orders of magnitude higher than suggested by a global compilation of bedrock surface erosion rates based on ^{10}Be (Portenga and Bierman, 2011), and measurements of upstanding, resistant lithic components (ca. 0.2 – 5.0 mm/ka) in crystalline rock surfaces in Arctic Norway (André, 2002). The authors inferred that shorter-term erosion rates derived from luminescence measurements were higher than the longer-term averages due to the stochastic nature of weathering impacting upon shorter-term erosion rates, this is also suggested by the data presented here. These stochastic processes (i.e. varying over time) will be controlled by the in-situ weathering rates, which provided the material for erosion. For bare rock surfaces in wet, temperat~~ur~~e climates, weathering rates are primarily driven by rock-type and moisture availability (i.e. precipitation) (Hall et al. 2012; Swantesson, 1992). The Torridonian sandstones are hard, cemented rocks (Stewart, 1984; Stewart and Donnellson, 1992) susceptible to granular disintegration (e.g. Ballantyne and Whittington, 1987), which may have been stochastic in nature due to changing moisture availability for chemical weathering over time (Hall et al. 2012; Swantesson, 1992). Although ~~the~~ Torridonian sandstone<u>s</u> ~~is~~ <u>are</u> unlikely to be prone to frost shattering due to ~~its~~ <u>their</u> low permeability and porosity (Lautridou, 1985; Hudec 1973 in Hall et al. 2012), cracks, faults and joints in the rock may have facilitated stochastic physical weathering (Swantesson 1992; Whalley et al. 1982)<u>, but little field evidence of this was preserved</u>.

<u>The modelled erosion histories that we have calculated here using the luminescence erosion-meter for samples BALL02 and BALL03 would have had a minimal effect upon the cosmogenic nuclide exposure age (4.54 ± 0.27 ka; Ballantyne and Stone, 2004). Only the steady-state erosion rate of 66 mm/ka inferred for BALL02 using the IR_{50} signal, when applied for durations exceeding 1 ka, would ~~have~~ increase ~~d~~ the exposure age to any great degree. For example, when the steady-state erosion rate of 66 mm/ka was applied for 0.1 ka, the corrected cosmogenic nuclide exposure age would have been 4.58 ka and, when the same erosion rate was applied for 1 ka it would have been 4.99 ka; these corrected ages were consistent within ± 2 σ uncertainties of the uncorrected age of 4.54 ± 0.27 ka (reported at 1σ: Ballantyne and Stone, 2004). The higher, transient erosion rates inferred for BALL03 were all applied for such a short period of time (e.g. Table 3) that they had a minimal effect on the cosmogenic nuclide exposure age.</u>

Based on the long-term erosion rates derived here, the boulder sampled for BALL02 would have lost a total of 300 mm (IR_{50}), 41 mm ($pIRIR_{150}$) and 54 mm ($pIRIR_{225}$) from the surface over 4.54 ka, while the long-term erosion rates determined for BALL03 suggested that the boulder surface would have lost 27 mm (IR_{50}), 64 mm ($pIRIR_{150}$) and 50 mm ($pIRIR_{225}$). All of these values (except for the IR_{50} signal of BALL02) were broadly consistent with field observations of quartz protrusions on the surface of boulders >2 x 2 x 2 m that were densely distributed within the rock avalanche feature (Fig. 1). Alternatively, the maximum (shorter-term) erosion rate end members of the transient erosion histories would have removed 1407 mm (BALL02, $pIRIR_{225}$), 2088 mm (BALL03, IR_{50}), 454 mm (BALL03, $pIRIR_{150}$) and 817 mm (BALL03, $pIRIR_{225}$) from the boulder surface over the 4.54 ka. These large values were inconsistent with field evidence and so indicative of the transient state of erosion where high erosion rates were only sustained over short periods of time.

6.3 Late Holocene erosion history

The transient state of erosion inferred by the rock luminescence measurements reflected the stochastic nature of erosion over the last 4 ka, where a lower time-averaged erosion rate was interrupted by discrete intervals of higher time-averaged erosion rates. Rock weathering would have been dependent upon a variety of factors, primarily rock type and climate (Merrill 1906). The main constituents of the Torridonian sandstones are quartz, alkali and plagioclase feldspar (mostly albite), with precipitated quartz cementing the rock being resistant to chemical weathering (Stewart and Donnellan, 1992). However, the red colouring of the sandstones represents the presence of Fe within the rock (Stewart and Donnellsan, 1992), which is prone to chemical weathering via oxidation and reduction. Field evidence of quartz grain protrusions on the rock surfaces (Fig. 1) indicated that granular disintegration, rather than flaking or shattering, was the likely weathering process that produced material for erosion on these hard boulders (e.g. Swantesson, 1992). This is also supported by a lack of shattered material surrounding the large sampled boulders (and in fact on much of the Beinn Alligin rock avalanche deposit), despite the presence of dense, low-level vegetation surrounding the boulders (e.g. Fig. S6). Granular disintegration has been reported as responsible for much of the general microweathering in the temperate climate of Southern and Central Sweden during the Holocene (e.g. Swantesson, 1992).

Given the coupling between precipitation, ~~mean annual~~ temperature and erosion (e.g. Reiners et al., 2003; Portenga and Bierman, 2011), the stochastic processes producing transient erosion can relate to varying environmental conditions (Hall et al. 2012; Swantesson, 1992; Whalley et al. 1982). In an environment where moisture is abundant due to high precipitation rates (e.g. for NW Scotland, annual precipitation rates between 1981 and 2010 were ca. 2,300 mm/a; Met Office, 2021), chemical weathering dominates; this is~~, as~~ also reported for Holocene weathering processes in Sweden (Swantesson, 1989, 1992). Moisture availability, rather than temperature, is the limiting factor as studies have reported the presence of chemical weathering in natural settings subject to sub-zero temperatures (e.g. northern Canada, Hall, 2007; Antarctica, Balke et al. 1991). Proxy evidence from across the British Isles records variability in temperature and precipitation rates over the last 4.5 ka, where key increases in precipitation occurred at 2,750, 1,650 and 550 cal. years BP

correlated to Bond cycles (Charman, 2010). Thus, the transient erosion rates measured from boulders of the Beinn Alligin avalanche were potentially a representation of the fluctuations in moisture availability experienced over the last 4.5 ka. Such processes can only be inferred from luminescence depth profiles as they are sensitive to changing erosion on shorter timeframes than all other techniques.

7. Conclusion

This study applies ~~the~~ new rock luminescence techniques to a well-constrained test scenario provided by flat-topped boulders from the Beinn Alligin rock avalanche in NW Scotland (a wet, temperate climate), which are lithologically consistent (Torridonian sandstones), have known-age road-cuts for parameterisation of μ and $\overline{\sigma\varphi_0}$, have known cosmogenic nuclide exposure ages (4.54 ± 0.27 ka) and independently-derived Holocene erosion rates (ca. 3.3 to 12.0 mm/ka). Applying the rock luminescence techniques for exposure dating underestimated the cosmogenic nuclide ages for the Beinn Alligin rock avalanche expected due to high erosion rates (as supported by field evidence of quartz grain protrusions on the rock surfaces). Alternatively, the erosion rates determined were consistent with expected rates that were independently measured in the field from boulder-edge roundness when considering the relative timescales of the time-averaged erosion rates. The findings show that the luminescence erosion-meter has the resolution and sensitivity required to detect transient erosion of boulders over the last 4.5 ka. The transient erosion rates ~~-~~reflect~~ing~~ the stochastic nature of erosional processes in the wet, temperate region of NW Scotland, likely in response to the known fluctuations in moisture availability (and to a lesser extent temperature), which control the extent of chemical weathering. This study demonstrates that the luminescence erosion-meter has huge potential for inferring erosion rates on sub-millennial scales for both steady-state and transient states of erosion (i.e. stochastic processes), which is currently impossible with other techniques. Larger sample populations and careful sampling of rock surfaces (avoiding the potential for rock pools and trickle paths) will likely be key for accurate measurements of landscape-scale erosion, and the use of a MET-pIRIR protocol (50, 150 and 225 °C) is advantageous as it can identify samples suffering from the complexities introduced by within-sample variability (e.g. surficial coatings).

Author contributions

RS, DS and RSJ were involved in project conception. RS, DS, RSJ and SB performed the field sampling. RS, DS, JB and GJ performed the measurements, analysis and interpretations. All authors contributed to the writing of the manuscript, including the preparation of figures.

Acknowledgments

Field and laboratory work was funded by Durham University Department of Geography Research Development Fund to DS. The rock luminescence equipment in the Liverpool Luminescence Laboratory was funded by a Royal Society Research Grant (RG170194) to RKS. DS is supported by a NERC Independent Research Fellowship NE/T011963/1. We thank

Benjamin Lehmann, an anonymous reviewer and the Associate Editor Jim Feathers for their constructive comments which improved this manuscript.

References

Aitken, M.J. 1985. Thermoluminescence dating: Past progress and future trends. Nuclear Tracks and Radiation Measurements, 10, 3-6.

André, M.-F. 2002. Rates of postglacial rock weathering of granite roches moutonnées in northern Scandinavia (Abisko-Riksgränsen area, 68°N). Geografiska Annaler 64A, 139–150.

Balke, J., Haendel, D., Krüger, W. 1991. Contribution to the weathering-controlled removal of chemical elements from the active debris layer of the Schirmacher Oasis, East Antarctica. Zeitschrift für Geologische Wissenschaften, 19, 153–158.

Ballantyne, C.K. 1987. The Beinn Alligin 'rock glacier'. In Ballantyne, C.K. and Sutherland, D.G., editors, Wester Ross:field guide,Cambridge: Quaternary Research Association, 134-37.

Ballantyne, C.K. 2002. Paraglacial geomorphology. Quaternary Science Reviews, 21, 1935-2017.

Ballantyne, C.K. 2003. A Scottish sturzstrom: The Beinn Alligin rock avalanche, Wester Ross. Scottish Geographical Journal, 119, 159-167.

Ballantyne, C.K., Whittington, G. 1987. Niveo-aeolian sand deposits on An Teallach, Wester Ross, Scotland. Earth and Environmental Science Transactions of The Royal Society of Edinburgh, 78, 51 – 63.

Ballantyne, C.K., Stone, J.O. 2004. The Beinn Alligin rock avalanche, NW Scotland: cosmogenic ^{10}Be dating, interpretation and significance. The Holocene, 14, 448-453.

Bennett, M.R., Boulton, G.S. 1993. Deglaciation of the Younger Dryas or Loch Lomond Stadial ice-field in the northern Highlands, Scotland. Journal Quaternary Science, 8, 133–145.

Bowen, D.Q. 1992. The Pleistocene of North West Europe. Science Progress, 76, 209-223.

Brill, D., May, S.M., Mhammdi, N., King, G., Lehmann, B., Burow, C., Wolf, D., Zander, A., Brückner, H. 2021. Evaluating optically stimulated luminescence rock surface exposure dating as a novel approach for reconstructing coastal boulder movement on decadal to centennial timescales. Earth Surface Dynamics, 9, 205-234.

Brown, N.D. 2020. Which geomorphic processes can be informed by luminescence measurements. Geomorphology, 367, 107296.

Brown, N.D., Moon, S. 2019. Revisiting erosion rate estimates from luminescence profiles in exposed bedrock surfaces using stochastic erosion simulations. Earth and Planetary Science Letters, 528, 115842.

Chapot, M.S., Sohbati, R., Murray, A.S., Pederson, J.L., Rittenour, T.M. 2012. Constraining the age of rock art by dating a rockfall event using sediment and rock-surface luminescence dating techniques. Quaternary Geochronology, 13, 18-25.

Charman, D. 2010. Centennial climate variability in the British Isles during the mid–late Holocene. Quaternary Science Reviews, 29, 1539-1554.

Esri. "World Imagery" [basemap]. Scale Not Given. "World Imagery". December 12, 2009. https://services.arcgisonline.com/ArcGIS/rest/services/World_Imagery/MapServer. (Feb, 11, 2021).

Esri. "Topographic" [basemap]. Scale Not Given. "World Topographic Map". June 14, 2013. http://www.arcgis.com/home/item.html?id=30e5fe3149c34df1ba922e6f5bbf808f. (Feb, 11, 2021).

Ford, D., Williams, P. 1989. Karst Geomorphology and Hydrology. Unwin Hyman, London. 601 pp.

Freiesleben, T., Sohbati, R. Murray, A., Jain, M., al Khasawneh, S., Hvidt, S., Jakobsen, B. 2015. Mathematical model quantifies multiple daylight exposure and burial events for rock surfaces using luminescence dating. Radiation Measurements, 81, 16-22.

Gliganic, L.A., Meyer, M.C., Sohbati, R., Jain, M., Barrett, S. 2019. OSL surface exposure dating of a lithic quarry in Tibet: Laboratory validation and application. Quaternary Geochronology, 49, 199-204.

Golledge, N.R., Hubbard, A., Sugden, D.E. 2008. High-resolution numerical simulation of Younger Dryas glaciation in Scotland. Quaternary Science Reviews, 27, 888-904.

Gordon, J.E. 1993. Beinn Alligin. In Gordon, J.E. and Sutherland, D.G., editors Quaternary of Scotland, London: Chapman and Hall, 118-22.

Habermann, J., Schilles, T., Kalchgruber, R., Wagner, G.A., 2000. Steps towards surface dating using luminescence. Radiation Measurements 32, 847-851.
Hall, K. 2007. Evidence for freeze-thaw events and their implications for rock weathering in northern Canada, II: the temperature at which water freezes in rock. Earth Surface Processes and Landforms, 32, 249–259.
Hall, K., Arocena, J.M., Boelhouwers, J., Zhu, L. 2005. The influence of aspect on the biological weathering of granites: observations from the Kunlun Mountains, China. Geomorphology, 67, 171–188.
Hall, K., Guglielmin, M., Strini, A. 2008. Weathering of granite in Antarctica II: thermal data at t the grain scale. Earth Surface Processes and Landforms, 33, 475–493.
Hall, K., Thorn, C., Sumner, P. 2012. On the persistence of 'weathering'. Geomorphology, 149-150, 1-10.
Hanna, F.K. 1966. A technique for measuring the rate of erosion of cave passages. Proceedings University of Bristol Spelaeology Society, 11, 83–86.
Herman, F., Rhodes, E.J., Braun, J., Heiniger, L. 2010. Uniform erosion rates and relief amplitude during glacial cycles in the Southern Alps of New Zealand, as revealed from OSL-thermochronology. Earth and Planetary Science Letters, 297, 183-189.
High, C.J., Hanna, F.K. 1970. A method for the direct measurement of erosion on rock surfaces. British Geomorphological Research Group Technical Bulletin, 5, 1–25.
Hijmans, R.J. (2019). raster: Geographic Data Analysis and Modeling. R package version 2.9-23. https://CRAN.R-project.org/package=raster
Huntley, D.J., Lamothe, M. 2001. Ubiquity of anomalous fading in K-feldspars and the measurement and correction for it in optical dating, 38, 1093-1106.
Israelli, Y., Emmanuel, S. 2018. Impact of grain size and rock composition on simulated rock weathering. Earth Suface Dynamics, 6, 319-327.
Jenkins, G. T. H., Duller, G. A. T., Roberts, H. M., Chiverrell, R. C., Glasser, N. F. 2018. A new approach for luminescence dating glaciofluvial deposits – High precision optical dating of cobbles. Quaternary Science Reviews, 192, 263 – 273.
Kirkbride, M.P., Bell, C.M. 2010. Edge-roundness of boulders of Torridonian Sandstone (northwest Scotland): applications for relative dating and implications for warm and cold climate weathering rates. Boreas DOI 10.1111/j.1502-3885.2009.00131.
Kolb, T., Fuchs, M. 2018. Luminescence dating of pre-Eemian (pre-MIS 5e) fluvial terraces in Northern Bavaria (Germany) – Benefits and limitations of applying a pIRIR225-approach. Geomorphology, 321, 16-32.
Laskaris, N., Liritzis, I. 2011. A new mathematical approximation of sunlight penetrations in rocks for surface luminescence dating. Journal of Luminescence, 131, 1874-1884.
Lehmann, B., Valla, P.G., King, G.E., Herman, F. 2018. Investigation of OSL surface exposure dating to reconstruct post-LIA glacier fluctuations in the French Alps (Mer de Glace, Mont Blanc massif). Quaternary Geochronology, 44, 63-74.
Lehmann, B., Herman, F., Valla, P.G., King, G.E., Biswas, R.H. 2019a. Evaluating post-glacial bedrock erosion and surface exposure duration by coupling in situ optically stimulated luminescence and 10Be dating. Earth Surface Dynamics, 7, 633-662.
Lehmann, B., Herman, F., Valla, P.G., King, G.E., Biswas, R.H., Ivy-Ochs, S., Steinemann, O., Christl, M. 2019b. Postglacial erosion of bedrock surfaces and deglaciation timing: New insights from the Mont Blanc massif (western Alps). Geology, https://doi.org/10.1130/G46585.1
Li, B., Li, S-H. 2011. Luminescence dating of K-feldspar from sediments: A protocol without anomalous fading correction. Quaternary Geochronology. 6, 468-479.
Liu, J., Murray, A., Sohbati, R., Jain, M. 2016. The effect of test dose and first IR Stimulation temperature on post-IR IRSL measurements of rock slices. Geochronometria, 43, 179-187.
Luo, M., Chen, J., Liu, J., Qin, J., Owen, L., Han, F., Yang, H. Wang, H., Zhang, B., Yin, J., Li, Y. 2018. A test of rock surface luminescence dating using glaciofluvial boulders from the Chinese Pamir. Radiation Measurements, 120, 290-297.
Merrill, G.P. 1906. A Treatise on Rocks. Rock-Weathering and Soils, Macmillan, New York. 400 pp.
Met Office, 2021. UK Climate averages (1981-2010): Kinlochewe Met station (57.613°N, -5.308°W) https://www.metoffice.gov.uk/research/climate/maps-and-data/uk-climate-averages/gfhpz0nu4 [Accessed 18/01/2021].

618 Meyer, M.C., Gliganic, L.A., Jain, M., Schmidmair, D. 2018. Lithological controls on light penetration into rock surfaces –
619 Implications for OSL and IRSL surface exposure dating. Radiation Measurements, 120, 298-304.
620 Ou, X.J., Roberts, H.M., Duller, G.A.T., Gunn, M.D., Perkins, W.T. 2018. Attenuation of light in different rock types and
621 implications for rock surface luminescence dating. Radiation Measurements, 120, 305-311.
622 Parish, R. 1994. The influence of feldspar weathering on luminescence signals and the implications for luminescence dating
623 of sediments. In Robinson, D.A. and Williams, R.B.G., editors, Rock weathering and landform
624 evolution, Chichester: Wiley.
625 Pederson, J.L., Chapot, M.S., Simms, S.R., Sohbati, R., Rittenour, T.M., Murray, A.S., Cox, G. 2014. Age of Barrier
626 Canyon-style rock art constrained by cross-cutting relations and luminescence dating techniques. PNAS 111, 12986-
627 12991.
628 Polikreti, K., Michael, C.T., Maniatis, Y., 2002. Authenticating marble sculpture with thermoluminescence. Ancient TL 20,
629 11-18.
630 Polikreti, K. Michael, C.T. and Maniatis, Y. 2003. Thermoluminescence characteristics of marble and dating of freshly
631 excavated marble objects. Radiation Measurements, 37, 87–94.
632 Portenga, E.W., Bierman, P.R. 2011. Understanding Earth's eroding surface with ^{10}Be. GSA Today, 21, 4-10.
633 Prescott, J.R., Hutton, J.T. 1994. Cosmic ray and gamma ray dosimetry for TL and ESR. Nuclear Tracks and Radiation
634 Measurements, 14, 223-227.
635 Reiners, P.W., Brandon, M.T. 2006. Using thermochronology to understand orogenic erosion. Annual Review of Earth
636 Planetary Science,doi: 10.1146/ annurev.earth.34.031405.125202.
637 Riebe CS, Kirchner JW, Finkel RC. 2003. Long-term rates of weathering and physical erosion from cosmogenic nuclides
638 and geochemical mass balance. Geochim. Cosmochim. Acta, 67, 4411–27
639 Roberts, H.M. 2012. Testing Post-IR IRSL protocols for minimising fading in feldspars, using Alaskan loess with
640 independent chronological control. Radiation Measurements, 47, 716-724.
641 Robinson, D.A., Williams, R.B.G. 1987. Surface crusting of sandstones in southern England and northern France. In:
642 Gardner, V. (Ed.), International Geomorphology 1986, vol. 2. Wiley, Chichester, pp. 623–635.
643 Singhvi, A.K., Deraniyagala, S.U., Sengupta, D. 1986. Thermoluminescence dating of Quaternary red-sand beds: a case
644 study of coastal dunes in Sri Lanka. Earth and Planetary Science Letters, 80, 139-144.
645 Sissons, J.B. 1975. A fossil rock glacier in Wester Ross. Scottish Journal of Geology, 11, 83-86.
646 Sissons, J.B. 1976. A fossil rock glacier in Wester Ross. Reply to W.B. Whalley. Scottish Journal of Geology, 12, 178-79.
647 Smedley, R.K., Duller, G.A.T., Roberts, H.M. 2015. Assessing the bleaching potential of the post-IR IRSL signal for
648 individual K-feldspar grains: implications for single-grain dating. Radiation Measurements, 79, 33 – 42.
649 Smedley, R.K., Glasser, N.F., Duller, G.A.T. 2016. Luminescence dating of glacial advances at Lago Buenos Aires (~46 °S),
650 Patagonia. Quaternary Science Reviews, 134, 59 – 73.
651 Sohbati, R., Murray, A.S., Jain, M., Buylaert, J.P., Thomsen, K.J. 2011. Investigating the resetting of OSL signals in rock
652 surfaces. Geochronometria, 38, 249–258.
653 Sohbati, R., Murray, A.S., Buylaert, J.P., Almeida, N.A.C., Cunha, P.P. 2012a. Optically stimulated luminescence (OSL)
654 dating of quartzite cobbles from the Tapada do Montinho archaeological site (east-central Portugal). Boreas, 41, 452–
655 462.
656 Sohbati, R., Murray, A.S., Chapot, M.S., Jain, M., Pederson, J., 2012b. Optically stimulated luminescence (OSL) as a
657 chronometer for surface exposure dating. Journal of Geophysical Research Solid Earth, 117.
658 Sohbati, R., Liu, J., Jain, M., Murray, A.S., Egholm, D., Pairs, R., Guralnick, B. 2018. Centennial- to millennial-scale hard
659 rock erosion rates deduced from luminescence-depth profiles. Earth and Planetary Science Letter, 493, 218-230.
660 Stewart, A.D. 1982. Late Proterozoic rifting in NW Scotland: the genesis of the 'Torridonian'. Journal of Geological Society
661 of London, 139, 413-420.
662 Stewart, A.D. Donnellson, N.C.B. 1992. Geochemistry and provenance of red sandstones in the Upper Proterozoic Torridon
663 Group in Scotland. Scottish Journal of Geology, 28, 143-153.
664 Stocker, T.F., D. Qin, G.-K. Plattner, L.V. Alexander, S.K. Allen, N.L. Bindoff, F.-M. Bréon, J.A. Church, U. Cubasch, S.
665 Emori, P. Forster, P. Friedlingstein, N. Gillett, J.M. Gregory, D.L. Hartmann, E. Jansen, B. Kirtman, R. Knutti, K.
666 Krishna Kumar, P. Lemke, J. Marotzke, V. Masson-Delmotte, G.A. Meehl, I.I. Mokhov, S. Piao, V. Ramaswamy, D.
667 Randall, M. Rhein, M. Rojas, C. Sabine, D. Shindell, L.D. Talley, D.G. Vaughan and S.-P. Xie, 2013: Technical Sum-

668 mary. In: Climate Change 2013: The Physical Science Basis. Contribution of Working Group I to the Fifth Assessment
669 Report of the Intergovernmental Panel on Climate Change [Stocker, T.F., D. Qin, G.-K. Plattner, M. Tignor, S.K. Allen,
670 J. Boschung, A. Nauels, Y. Xia, V. Bex and P.M. Midgley (eds.)]. Cambridge University Press, Cambridge, United
671 Kingdom and New York, NY, USA.
672 Swantesson, J.O.H. 1989.Weathering phenomena in a cool temperate climate. Göteborgs University, Naturgeogr. Inst., Guni.
673 Rapport, 28.
674 Swantesson, J.O.H. 1992. Recent microweathering phenomena in Southern and Central Sweden. Permafrost and Periglacial
675 Processes, 3, 275-292.
676 Swantesson, J.O.H., Moses, C.A., Berg, G.E., Jansson, K.M. 2006. Methods for measuring shore platform micro-erosion: a
677 comparison of the micro-erosion meter and laser scanner. Z. Geomorpholology, 144, 1–17.
678 Thomsen, K. J., Murray, A. S., Jain, M. and Bøtter-Jensen, L. 2008. Laboratory fading rates of various luminescence signals
679 from feldspar-rich sediment extracts. Radiation Measurements, 43, 1474 –1486.
680 Thomsen, K.J., Murray, A.S., Jain, M. 2011. Stability of IRSL signals from sedimentary K-feldspar samples.
681 Geochronometria, 38, 1-13.
682 Thomsen, K.J., Kook, M., Murray, A.S., Jain, M. 2018. Resolving luminescence in spatial and compositional domains.
683 Radiation Measurements, 15, 260-266.
684 Thorn, C.E., Darmody, R.G., Dixon, J.C., Schlyter, P. 2001. The chemical weathering regime of Kärkevagge, arctic-alpine
685 Sweden. Geomorphology, 41, 37–52.
686 Trauerstein, M., Lowick, S.E., Preusser, F., Schlunegger, F. 2014. Small aliquot and single grain IRSL and post-IR IRSL
687 dating of fluvial and alluvial sediments from the Pativilca valley, Peru. Quaternary Geochronology, 22, 163-174.
688 Trudgill, S.T., Viles, H., Inkpen, R.J., Cooke, R.U. 1989. Remeasurement of weathering rates, St. Paul's Cathedral, London.
689 Earth Surface Processes and Landforms, 14, 175–196.
690 Twidale, C.R., 1982. Granite Landforms. Elsevier, Amsterdam. 372 pp.
691 Vafiadou, A., Murray, A.S., Liritzis, I., 2007. Optically stimulated luminescence (OSL) dating investigations of rock and
692 underlying soil from three case studies. Journal of Archaeological Science 34, 1659-1669.
693
694
695
696

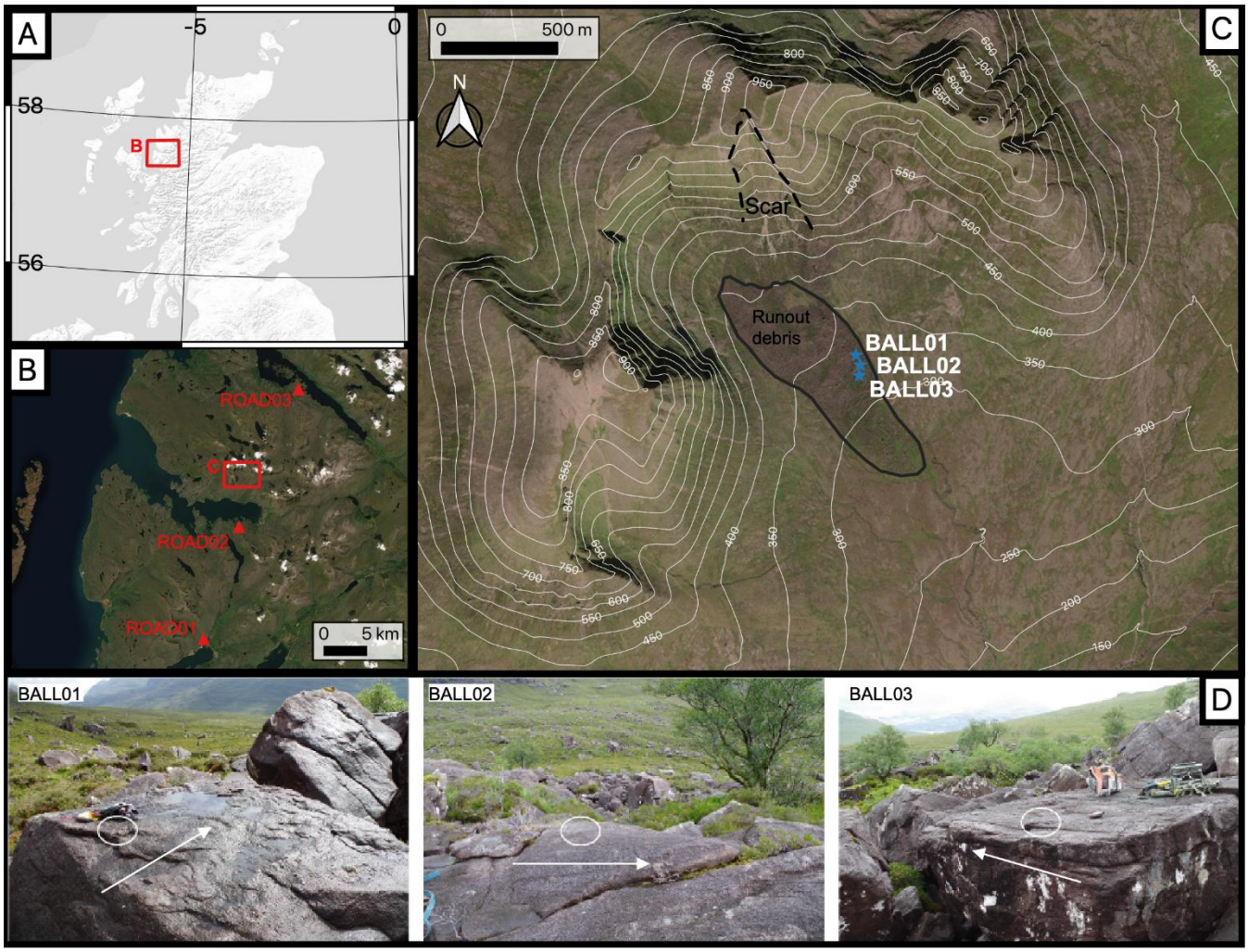

Figure 1. Location of the Beinn Alligin rock avalanche (57°35'N, 05°34'W) and roadcut sections in NW Scotland (A,B). Sample sites on the rock avalanche deposit (C). ~~**The backgrounds used are ESRI World Terrain Base (A) and ESRI World Imagery (B,C). Contains OS data © Crown copyright and database right (2021).**~~ **Photographs of flat-topped boulders sampled** **and the general rock avalanche flow direction (white arrow)** **for BALL01, BALL02 and BALL03 (D).** **The backgrounds used are ESRI World Terrain Base (A) and ESRI World Imagery (B,C). Contains OS data © Crown copyright and database right (2021). Scar and runout debris locations mapped in (C) follow Ballantyne and Stone (2004).**

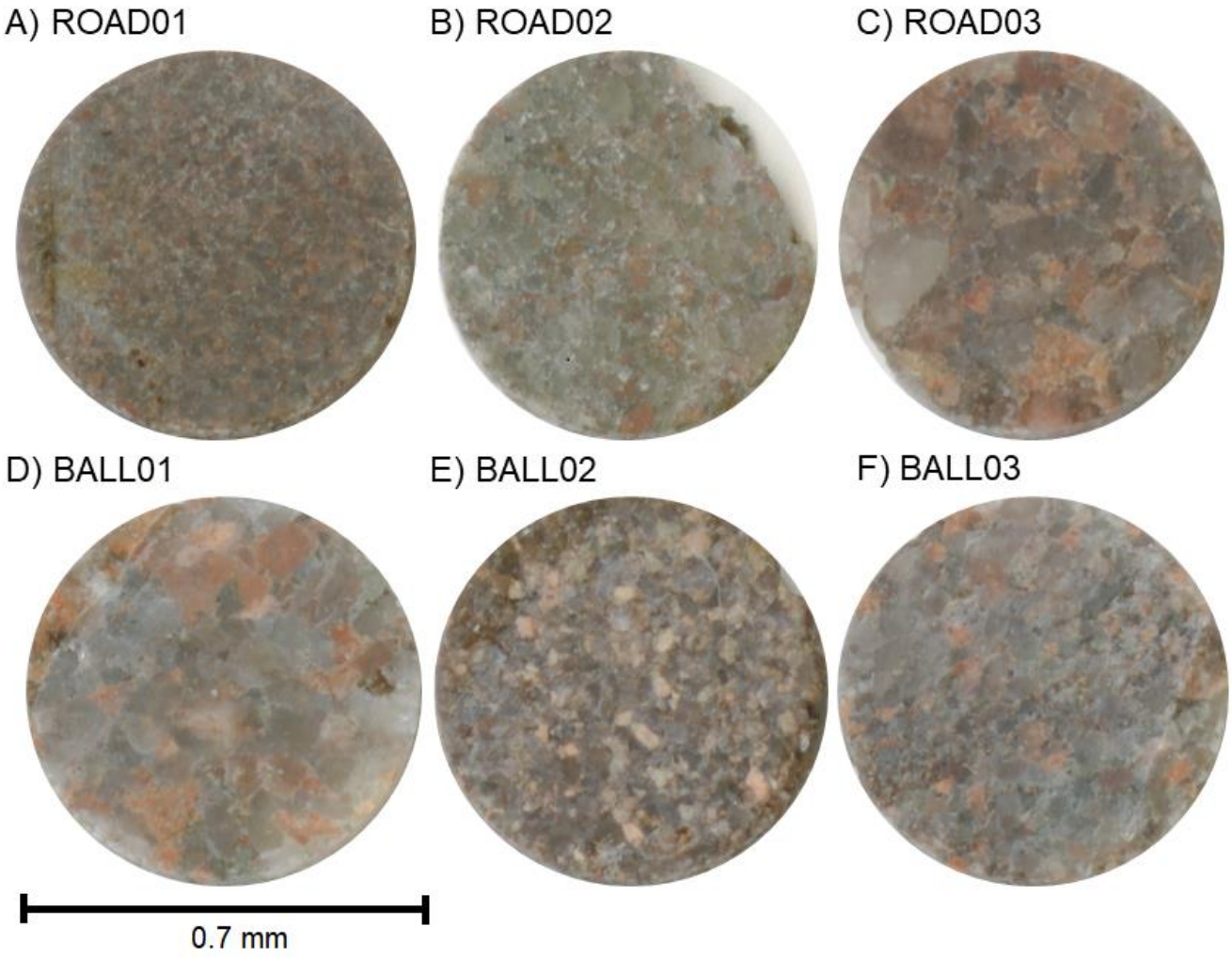

Figure 2. Images of example rock slices (0.7 mm diameter) for each sample taken using the EPSON Expression 11000XL flatbed scanner.

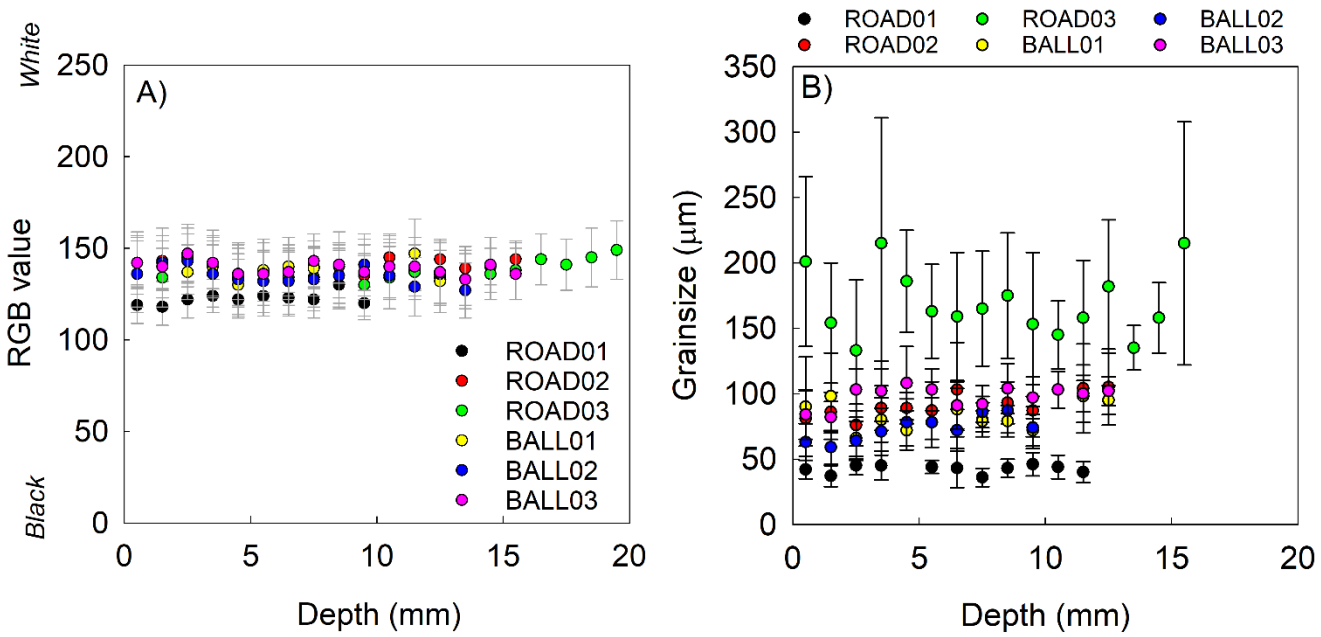

Figure 3. (A) RGB values (0 = black and 255 = white) and (B) grainsize for each sample, calculated as the mean (± standard deviation) of the slices at each depth in all of the replicate cores analysed. Note that the RGB values and grainsize measurements were not derived from exactly the same cores, but example cores for each sample.

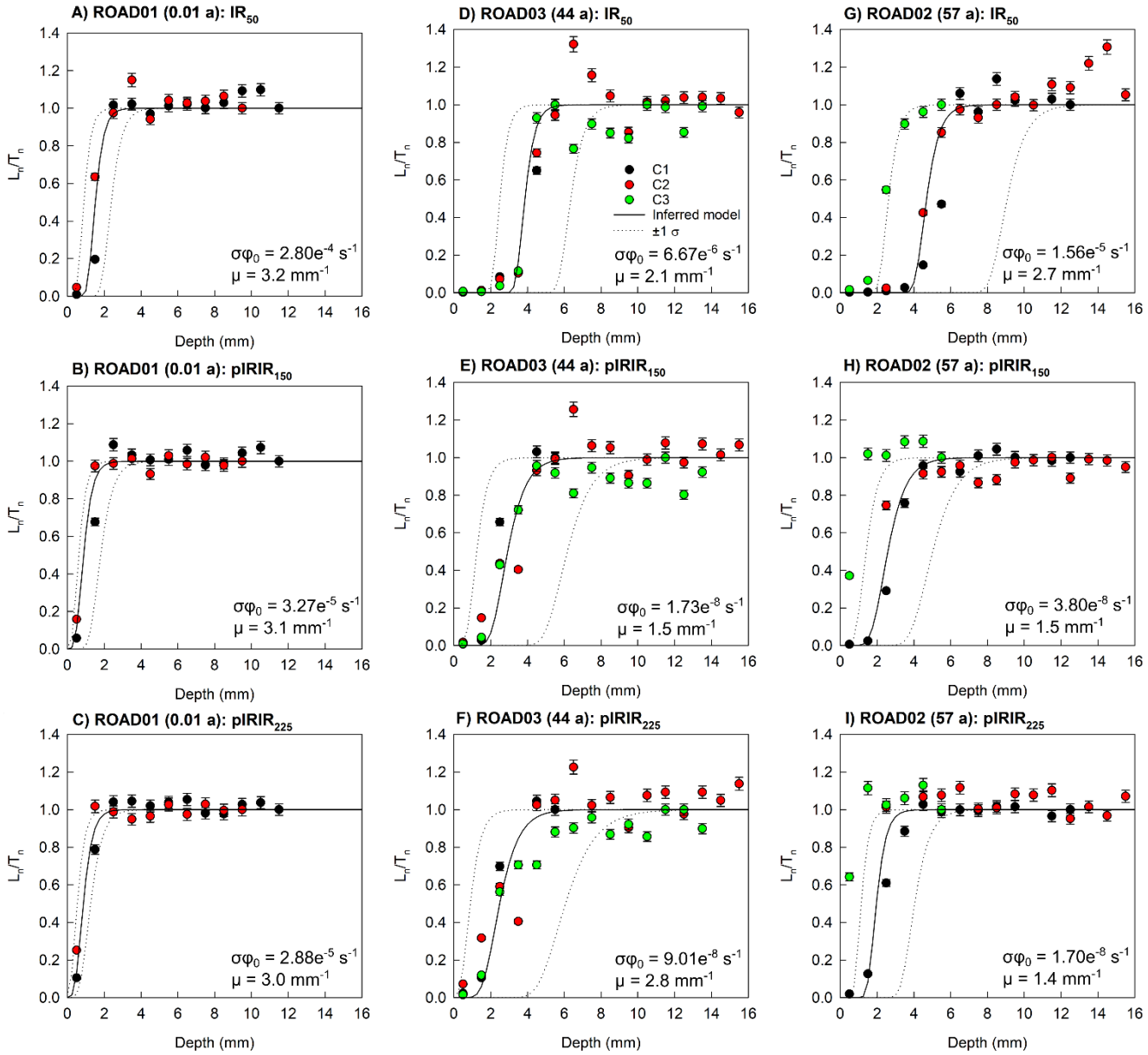

Figure 4. Presented in age-order are the IRSL-depth profiles for each of the three replicate cores analysed per sample using the IR_{50} (A,D,G), $pIRIR_{150}$ (B,E,H) and $pIRIR_{225}$ (C,F,I) signals for samples ROAD01 (0.01 a; A-C), ROAD03 (44 a; D-F) and ROAD02 (57 a; G-I). All of the raw L_n/T_n data presented in this figure (Table S2-S4) were normalised individually for each core, and subsequent analysis uses the data in this format. The black line shown is the inferred model that was fitted to derive the corresponding $\overline{\sigma\varphi_0}$ and μ values included in each figure. The dotted lines show the corresponding fits modelled using the ± 1 σ $\overline{\sigma\varphi_0}$ and μ values (Table 2). Note that core 3 of ROAD02 was not considered for fitting.

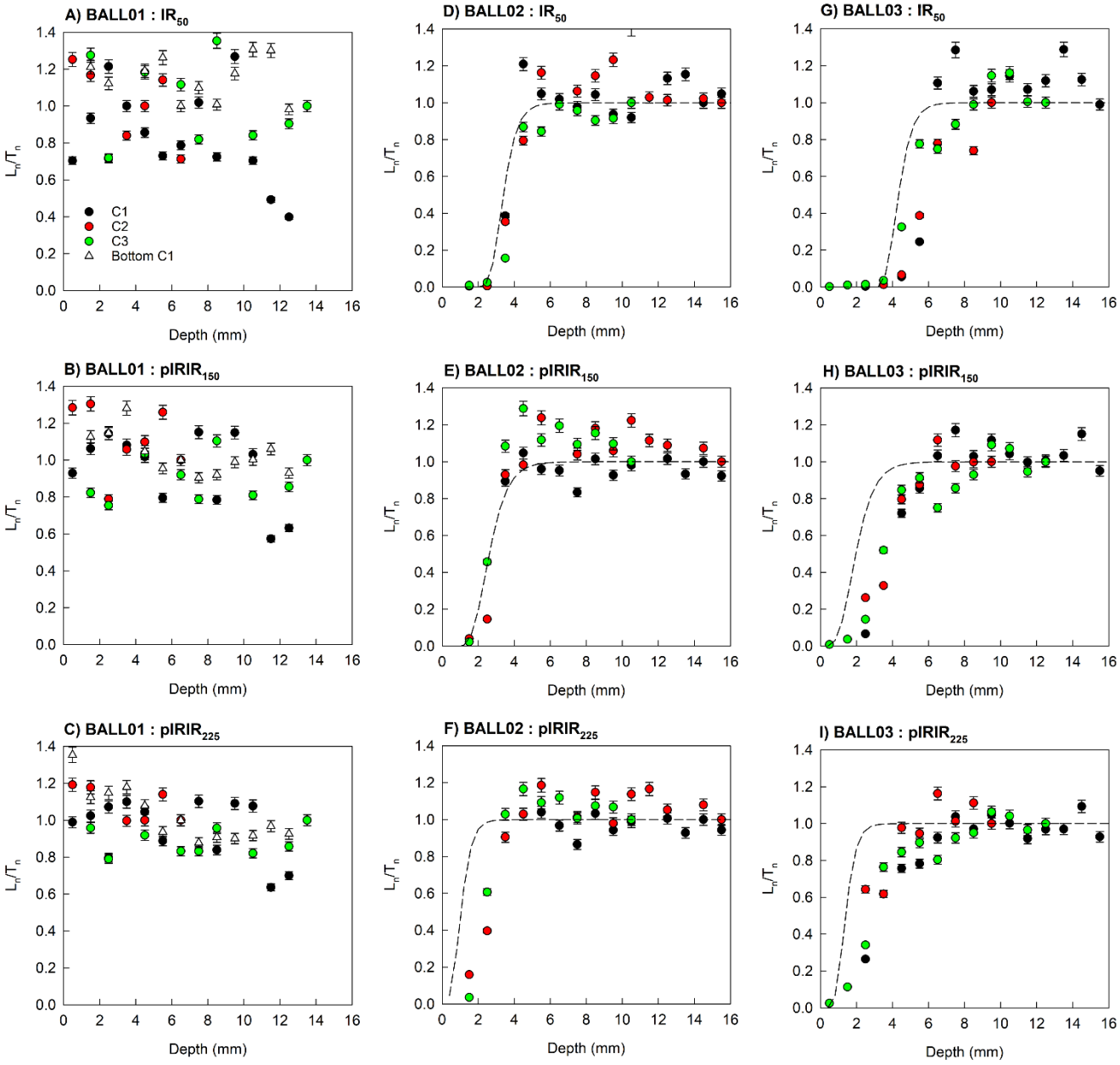

Figure 5. IRSL-depth profiles for each replicate cores analysed using the IR_{50} (A,D,G), $pIRIR_{150}$ (B,E,H) and $pIRIR_{225}$ (C,F,I) signals for samples BALL01 (A-C), BALL02 (D-F) and BALL03 (G-I). All of the raw L_n/T_n data (Table S5-S7) were normalised individually for each core, and subsequent analysis uses the data in this format. The dashed line is the inferred erosion model for each luminescence depth profile derived from the probability distributions shown in Fig. 7, where erosion rates are included in Table 3.

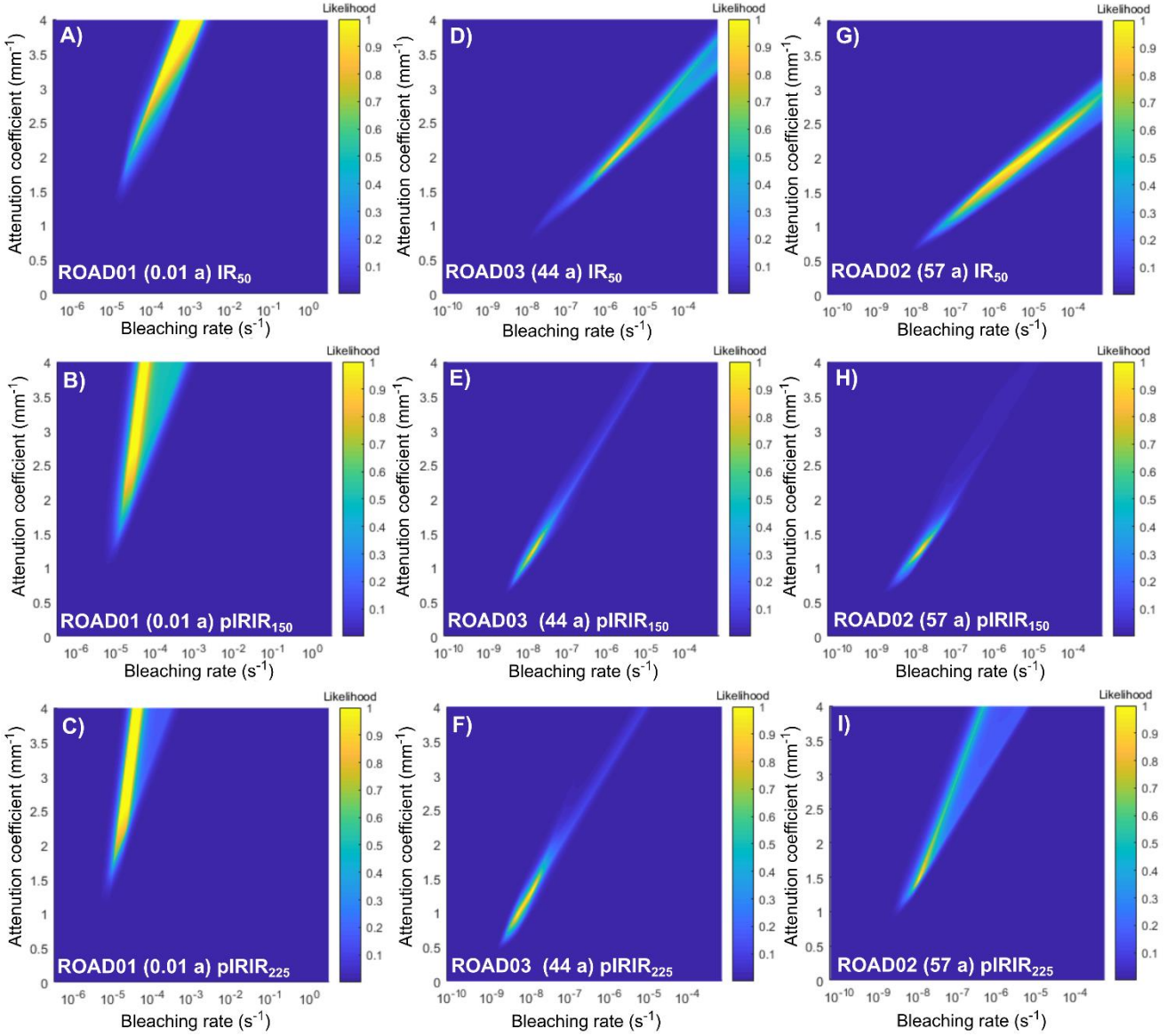

Figure 6. Presented in age-order is the relationship between $\overline{\sigma\varphi_0}$ and μ parameters for ROAD01 (A-C), ROAD03 (D-F) and ROAD02 (G-I) using the IR_{50} (A,D,G), $pIRIR_{150}$ (B,E,H) and $pIRIR_{225}$ (C,F,I) signals using the approach of Lehmann et al. (2018).

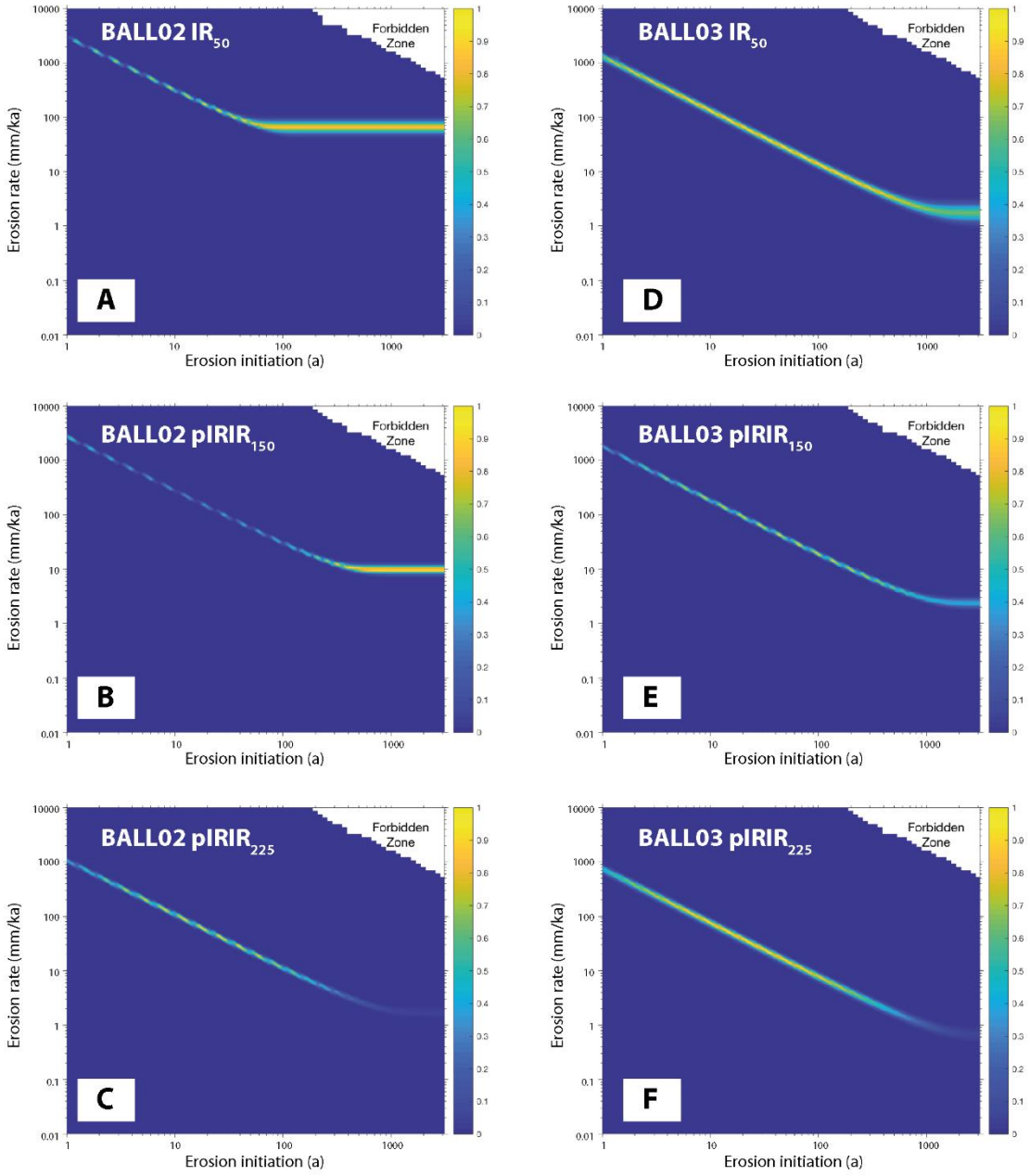

Figure 7. Probability distributions inverted from the respective plots of luminescence depth profiles derived from the inversion results (using the approach of Lehmann et al. 2019a) for samples BALL02 (A-C) and BALL03 (D-F) using the IR_{50}, (A,D), $pIRIR_{150}$ (B,E) and $pIRIR_{225}$ (C,F) signals. Forbidden zones define the range of solutions with high erosion rates and durations that are not feasible within the bounds of the experimental ^{10}Be and luminescence data.

Table 1. Luminescence results for the rock slices analysed in this study. Environmental dose-rates were determined using high-resolution gamma spectrometry. The dose-rates were calculated using the conversion factors of Guerin et al. (2011) and alpha (Bell, 1980) and beta (Guerin et al. 2012) dose-rate attenuation factors. An internal K-content of 10 ± 2 % (Smedley et al. 2012) and internal U and Th concentrations of 0.3 ± 0.1 ppm and 1.7 ± 0.4 ppm (Smedley and Pearce, 2016) were used to determine the internal alpha and beta dose-rates. An a-value of 0.10 ± 0.02 (Balescu and Lamothe, 1993) was used to calculate the alpha dose-rates. Cosmic dose-rates were determined after Prescott and Hutton (1994). Dose-rates were calculated using the Dose Rate and Age Calculator (DRAC; Durcan et al. 2015). Grain size was measured by randomly selecting grains in the rock slices for each sample and calculating ±1 standard deviation around the mean grain size.

Sample	Grain size (μm)	U (ppm)	Th (ppm)	K (%)	Internal alpha dose-rate (Gy/ka)	Internal beta dose-rate (Gy/ka)	External alpha dose-rate (Gy/ka)	External beta dose-rate (Gy/ka)	External gamma dose-rate (Gy/ka)	External cosmic dose-rate (Gy/ka)	Total dose-rate (Gy/ka)
BALL02	56-91	1.02±0.15	4.85±0.28	1.73±0.29	0.14±0.04	0.27±0.06	0.21±0.05	1.62±0.00	0.78±0.08	0.31±0.03	3.32±0.12
BALL03	79-117	1.02±0.14	5.21±0.28	1.86±0.29	0.16±0.04	0.35±0.08	0.17±0.04	1.71±0.00	0.83±0.08	0.31±0.03	3.52±0.12
ROAD01	33-51	2.07±0.27	7.80±0.42	2.45±0.43	0.10±0.03	0.16±0.03	0.61±0.12	2.43±0.00	1.22±0.11	0.30±0.03	4.81±0.18
ROAD02	67-113	1.55±0.18	5.67±0.38	2.88±0.40	0.15±0.04	0.32±0.08	0.23±0.05	2.59±0.00	1.16±0.10	0.30±0.03	4.76±0.15
ROAD03	112-225	1.93±0.21	5.30±0.30	1.96±0.31	0.18±0.04	0.58±0.20	0.14±0.04	1.85±0.00	0.96±0.08	0.29±0.03	4.00±0.22

Table 2. Calibration factors determined by fitting depth profiles. Note that values presented are medians.

Sample	IRSL signal	$\overline{\sigma\varphi_0}$ (s^{-1})	Range ±1 σ (s^{-1})	μ (mm^{-1})	Range ±1 σ (mm^{-1})
ROAD01	IR_{50}	$2.80e^{-4}$	$8.41e^{-4} – 6.43e^{-5}$	3.2	2.5 – 3.8
	$pIRIR_{150}$	$3.27e^{-5}$	$1.16e^{-4} – 2.14e^{-5}$	3.1	2.2 – 3.7
	$pIRIR_{225}$	$2.88e^{-5}$	$3.99e^{-5} – 1.51e^{-5}$	3.0	2.3 – 3.6
ROAD02	IR_{50}	$6.67e^{-6}$	$1.27e^{-4} – 3.50e^{-7}$	2.1	1.4 – 2.6
	$pIRIR_{150}$	$1.73e^{-8}$	$9.64e^{-8} – 9.75e^{-9}$	1.5	1.1 – 2.3
	$pIRIR_{225}$	$9.01e^{-8}$	$5.53e^{-7} – 2.31e^{-8}$	2.8	1.8 – 3.6
ROAD03	IR_{50}	$1.56e^{-5}$	$1.64e^{-4} – 1.48e^{-6}$	2.7	2.0 – 3.2
	$pIRIR_{150}$	$3.80e^{-8}$	$4.40e^{-7} – 1.12e^{-8}$	1.5	1.1 – 2.5
	$pIRIR_{225}$	$1.70e^{-8}$	$1.17e^{-7} – 4.70e^{-9}$	1.4	0.9 – 2.5

Table 3. Luminescence exposure ages and erosion rates determined using the approach of Lehmann et al. (2018) and Lehmann et al. (2019a), respectively. The values of $\overline{\sigma\varphi_0}$ and μ were determined from known-age sample ROAD02 (57 a).

Sample	Signal	$\overline{\sigma\varphi_0}$ (s^{-1})	μ (mm^{-1})	$\dot{D}$ (Gy/ka)	D_0 (Gy)	Exposure age (a)	Steady-state erosion rate (mm/ka)	Min. initiation time (a)	Max. transient erosion rate (mm/ka)	Initiation time (a)	Min. transient erosion rate (mm/ka)	Initiation time (a)
BALL02	IR_{50}	$6.67e^{-6}$	2.1	3.32 ± 0.12	500	8 ± 2	66	73	-	-	-	-
	$pIRIR_{150}$	$1.73e^{-8}$	1.5	3.32 ± 0.12	350	66 ± 16	9	593	-	-	-	-
	$pIRIR_{225}$	$9.01e^{-8}$	2.8	3.32 ± 0.12	350	263 ± 30	-	-	310	4	12	90
BALL03	IR_{50}	$6.67e^{-6}$	2.1	3.52 ± 0.12	500	387 ± 103	-	-	460	3	6	231
	$pIRIR_{150}$	$1.73e^{-8}$	1.5	3.52 ± 0.12	350	296 ± 54	-	-	100	19	14	137
	$pIRIR_{225}$	$9.01e^{-8}$	2.8	3.52 ± 0.12	350	362 ± 49	-	-	180	4	11	73

Supplementary material: Smedley et al.

Erosion rates in a wet, temperate climate derived from rock luminescence techniques

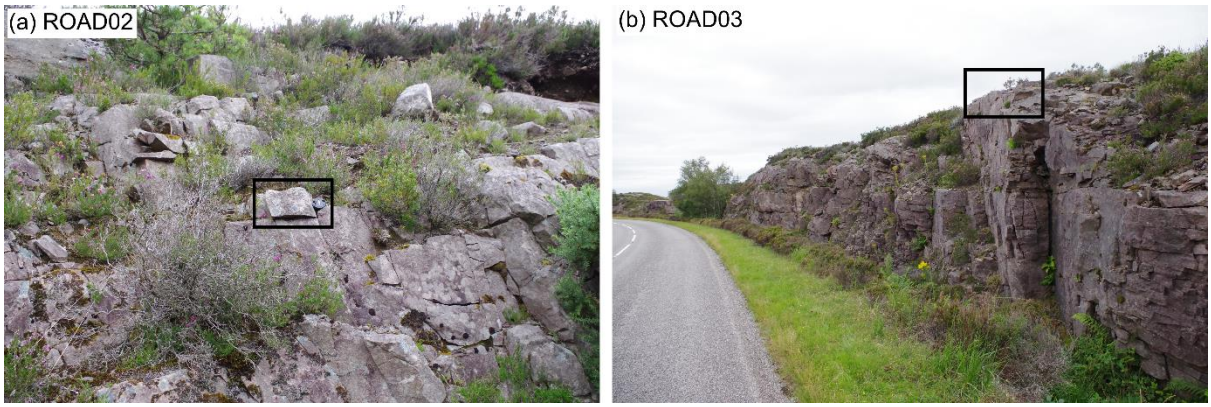

Fig. S1. Photographs of the known-age roadcut sections sampled for ROAD02 (a) and ROAD03 (b) constrained to 57 a and 44 a, respectively.

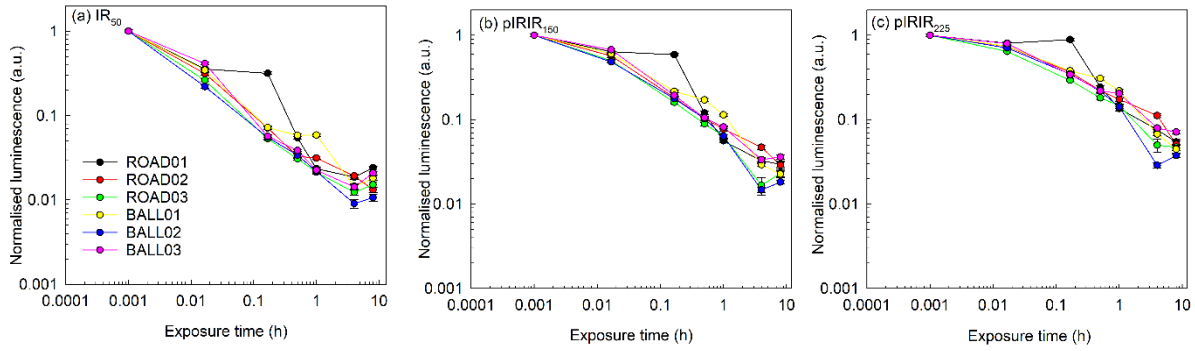

Fig. S2. Normalised luminescence signal remaining for individual discs from each sample after a given dose of 105 Gy and subsequent exposure to the solar simulator (0 m, 1 m, 10 m, 30 m, 1 h, 4 h and 8 h). Note that each disc had already been analysed for the natural luminescence signal.

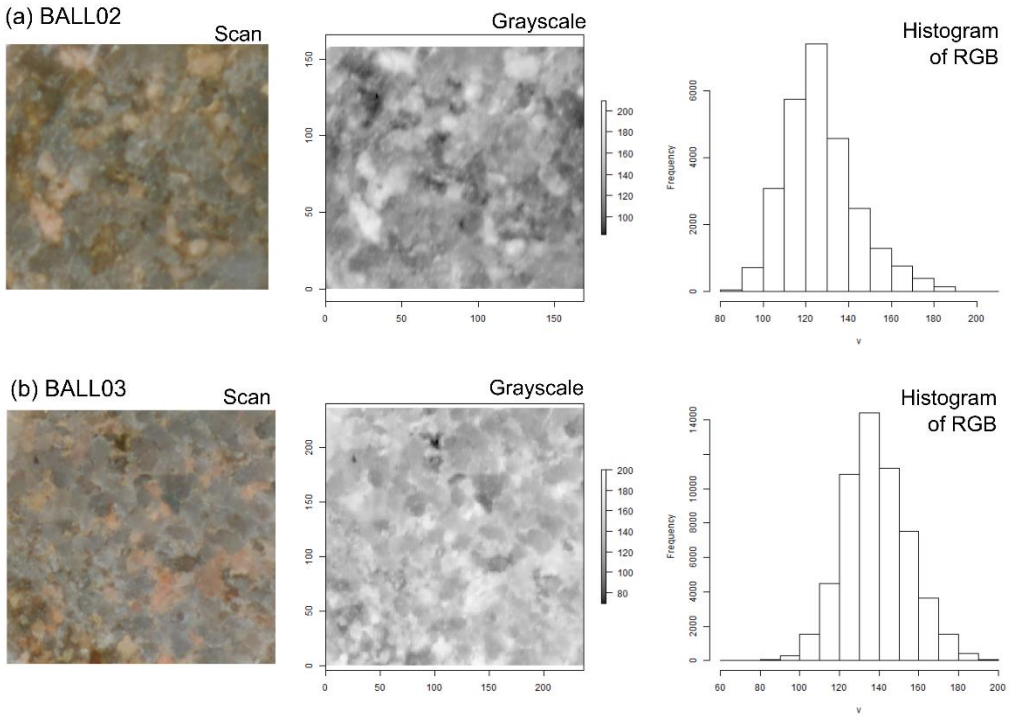

Fig. S3. Examples of true-colour and grayscale images for example slices of samples BALL02 and BALL03 using the EPSON Expression 11000XL flatbed scanner.

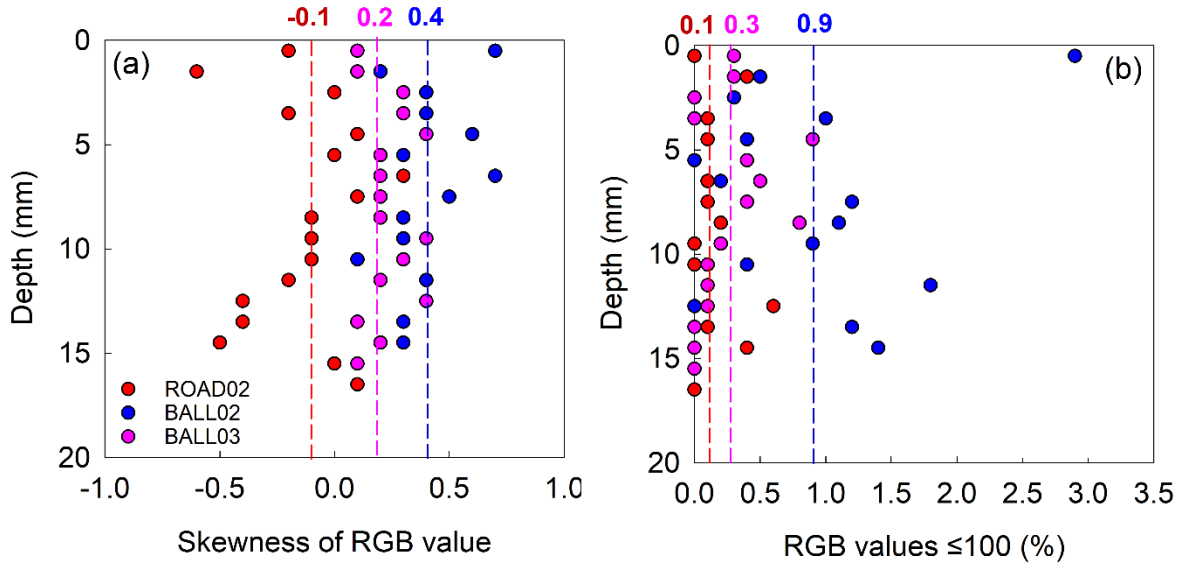

Fig. S4. Analysis of RGB values with depth for samples ROAD02, BALL02 and BALL03: (a) skewness of the pixel values for each images; (b) percentage of RGB values that are ≤100 (i.e. dark coloured).

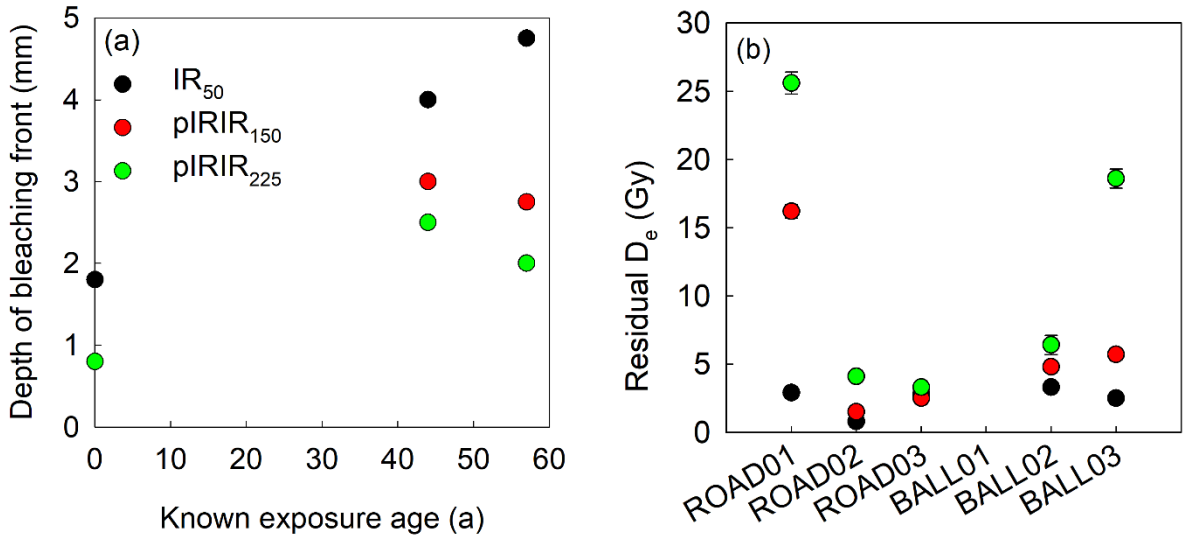

Fig. S5. (a) Depth of bleaching fronts for the known-age samples ROAD01 (0.01 a), ROAD02 (57 a) and ROAD03 (44 a). Note that the depth of the $pIRIR_{150}$ and $pIRIR_{225}$ bleaching fronts were identical for ROAD01 (0.01 a known-age sample). (b) Residual D_e values determined for the surface slice (0-1 mm depth) of each sample. Note that sample BALL01 is not plotted on this figure as the residual D_e values were large for all the IRSL signals: IR_{50} (477.5 ± 20.7 Gy), $pIRIR_{150}$ (574.6 ± 36.5 Gy) and $pIRIR_{225}$ (could not be interpolated on to the dose-response curve).

Fig. S6. Photograph of the Beinn Alligin rock avalanche to illustrate the nature of the area surrounding the sampled boulders, which includes dense vegetation, the small-scale topography of the boulders and little evidence of shattered material.

Table S1. Multi-elevated temperature post- IR IRSL sequence used for analysis.

Step	Procedure
1	Natural or regenerative dose
2	Preheat 250 °C for 100 s
3	IR LEDs 50 °C for 200 s
4	IR LEDs 150 °C for 200 s
5	IR LEDs 225 °C for 200 s
6	Test-dose 53 Gy
7	Preheat 250 °C for 100 s
8	IR LEDs 50 °C for 200 s
9	IR LEDs 150 °C for 200 s
10	IR LEDs 225 °C for 200 s
11	IR LEDs 290 °C for 200 s

Table S2. Raw L_n/T_n data used for fitting sample ROAD01 in Fig. 4A-C. Note that two rather than three cores were analysed for this sample.

	Core 1						Core 2					
	IR_{50}		$pIRIR_{150}$		$pIRIR_{225}$		IR_{50}		$pIRIR_{150}$		$pIRIR_{225}$	
Depth (mm)	L_n/T_n	Error	L_n/T_n	Error	L_n/T_n	Error	L_n/T_n	Error	L_n/T_n	Error	L_n/T_n	Error
0.5	0.01	0.00	0.06	0.00	0.11	0.00	0.05	0.00	0.16	0.01	0.25	0.01
1.5	0.20	0.01	0.68	0.02	0.79	0.03	0.64	0.02	0.98	0.03	1.02	0.03
2.5	1.02	0.03	1.09	0.03	1.04	0.03	0.98	0.03	0.99	0.03	0.99	0.03
3.5	1.02	0.03	1.03	0.03	1.05	0.03	1.15	0.04	1.01	0.03	0.95	0.03
4.5	0.97	0.03	1.01	0.03	1.02	0.03	0.94	0.03	0.93	0.03	0.97	0.03
5.5	1.01	0.03	1.01	0.03	1.04	0.03	1.04	0.03	1.03	0.03	1.03	0.03
6.5	1.02	0.03	1.06	0.03	1.05	0.03	1.03	0.03	0.99	0.03	0.98	0.03
7.5	1.00	0.03	0.98	0.03	0.98	0.03	1.04	0.03	1.02	0.03	1.03	0.03
8.5	1.03	0.03	0.99	0.03	0.98	0.03	1.06	0.03	0.98	0.03	1.00	0.03
9.5	1.09	0.03	1.04	0.03	1.03	0.03	1.00	0.03	1.00	0.03	1.00	0.03
10.5	1.10	0.03	1.07	0.03	1.04	0.03						
11.5	1.00	0.03	1.00	0.03	1.00	0.03						
12.5												
13.5												
14.5												
15.5												
16.5												
17.5												
18.5												
19.5												

Table S3. Raw L_n/T_n data used for fitting sample ROAD02 in Fig. 4G-I.

	Core 1						Core 2						Core 3					
	IR_{50}		$pIRIR_{150}$		$pIRIR_{225}$		IR_{50}		$pIRIR_{150}$		$pIRIR_{225}$		IR_{50}		$pIRIR_{150}$		$pIRIR_{225}$	
Depth (mm)	L_n/T_n	Error	L_n/T_n	Error	L_n/T_n	Error	L_n/T_n	Error	L_n/T_n	Error	L_n/T_n	Error	L_n/T_n	Error	L_n/T_n	Error	L_n/T_n	Error
0.5	0.00	0.00	0.01	0.00	0.02	0.00							0.02	0.00	0.37	0.01	0.64	0.02
1.5	0.00	0.00	0.02	0.00	0.13	0.00							0.07	0.00	1.02	0.03	1.12	0.04
2.5	0.01	0.00	0.29	0.01	0.61	0.02	0.02	0.00	0.75	0.02	1.01	0.03	0.55	0.02	1.01	0.03	1.03	0.03
3.5	0.03	0.00	0.76	0.02	0.89	0.03							0.90	0.03	1.08	0.03	1.06	0.03
4.5	0.15	0.00	0.96	0.03	1.03	0.03	0.43	0.01	0.92	0.03	1.07	0.03	0.96	0.03	1.09	0.03	1.13	0.04
5.5	0.47	0.01	0.93	0.03	0.99	0.03	0.85	0.03	0.92	0.03	1.08	0.03	1.00	0.03	1.00	0.03	1.00	0.03
6.5	1.06	0.03	0.93	0.03	1.00	0.03	0.98	0.03	0.96	0.03	1.12	0.03						
7.5	0.96	0.03	1.01	0.03	1.00	0.03	0.93	0.03	0.87	0.03	1.00	0.03						
8.5	1.14	0.03	1.05	0.03	1.02	0.03	1.00	0.03	0.88	0.03	1.01	0.03						
9.5	1.02	0.03	1.00	0.03	1.02	0.03	1.04	0.03	0.98	0.03	1.08	0.03						
10.5							1.00	0.03	0.99	0.03	1.08	0.03						
11.5	1.03	0.03	0.98	0.03	0.97	0.03	1.11	0.03	1.00	0.03	1.10	0.03						
12.5	1.00	0.03	1.00	0.03	1.00	0.03	1.09	0.03	0.89	0.03	0.95	0.03						
13.5							1.22	0.04	0.99	0.03	1.02	0.03						
14.5							1.31	0.04	0.99	0.03	0.97	0.03						
15.5							1.05	0.03	0.95	0.03	1.07	0.03						
16.5							1.25	0.04	1.00	0.03	1.00	0.03						
17.5																		
18.5																		
19.5																		

Table S4. Raw L_n/T_n data used for fitting sample ROAD03 in Fig. 4D-F.

	Core 1						Core 2						Core 3					
	IR_{50}		$pIRIR_{150}$		$pIRIR_{225}$		IR_{50}		$pIRIR_{150}$		$pIRIR_{225}$		IR_{50}		$pIRIR_{150}$		$pIRIR_{225}$	
Depth (mm)	L_n/T_n	Error	L_n/T_n	Error	L_n/T_n	Error	L_n/T_n	Error	L_n/T_n	Error	L_n/T_n	Error	L_n/T_n	Error	L_n/T_n	Error	L_n/T_n	Error
0.5	0.00	0.00	0.01	0.00	0.02	0.00	0.00	0.00	0.02	0.00	0.07	0.00	0.01	0.00	0.01	0.00	0.02	0.00
1.5	0.01	0.00	0.03	0.00	0.11	0.00	0.01	0.00	0.15	0.01	0.32	0.01	0.01	0.00	0.04	0.00	0.12	0.00
2.5	0.09	0.00	0.66	0.02	0.70	0.02	0.07	0.00	0.44	0.01	0.59	0.02	0.04	0.00	0.43	0.01	0.56	0.02
3.5							0.10	0.00	0.40	0.01	0.41	0.01	0.12	0.00	0.72	0.02	0.71	0.02
4.5	0.65	0.02	1.03	0.03	1.05	0.03	0.74	0.02	0.93	0.03	1.03	0.03	0.93	0.03	0.96	0.03	0.71	0.02
5.5	1.00	0.03	1.00	0.03	1.00	0.03	0.95	0.03	0.99	0.03	1.05	0.03	1.00	0.03	0.92	0.03	0.88	0.03
6.5							1.32	0.04	1.26	0.04	1.23	0.04	0.77	0.02	0.81	0.02	0.90	0.03
7.5							1.16	0.04	1.06	0.03	1.02	0.03	0.90	0.03	0.95	0.03	0.96	0.03
8.5							1.05	0.03	1.05	0.03	1.07	0.03	0.85	0.03	0.89	0.03	0.87	0.03
9.5							0.85	0.03	0.91	0.03	0.90	0.03	0.82	0.03	0.87	0.03	0.92	0.03
10.5							1.01	0.03	0.99	0.03	1.08	0.03	1.00	0.03	0.86	0.03	0.86	0.03
11.5							1.02	0.03	1.08	0.03	1.09	0.03	0.99	0.03	1.00	0.03	1.00	0.03
12.5							1.04	0.03	0.97	0.03	0.98	0.03	0.85	0.03	0.80	0.02	1.00	0.03
13.5							1.04	0.03	1.07	0.03	1.09	0.03	0.99	0.03	0.92	0.03	0.90	0.03
14.5							1.03	0.03	1.02	0.03	1.05	0.03						
15.5							0.96	0.03	1.07	0.03	1.14	0.04						
16.5							0.93	0.03	0.98	0.03	1.04	0.03						
17.5							1.08	0.03	1.05	0.03	1.07	0.03						
18.5							1.09	0.03	1.17	0.04	1.14	0.04						
19.5							1.00	0.03	1.00	0.03	1.00	0.03						

Table S5. Raw L_n/T_n data used for fitting sample BALL01 in Fig. 5A-C.

	Core 1						Core 2						Core 3						Core 4					
	IR_{50}		$pIRIR_{150}$		$pIRIR_{225}$		IR_{50}		$pIRIR_{150}$		$pIRIR_{225}$		IR_{50}		$pIRIR_{150}$		$pIRIR_{225}$		IR_{50}		$pIRIR_{150}$		$pIRIR_{225}$	
Depth (mm)	L_n/T_n	Error	L_n/T_n	Error	L_n/T_n	Error	L_n/T_n	Error	L_n/T_n	Error	L_n/T_n	Error	L_n/T_n	Error	L_n/T_n	Error	L_n/T_n	Error	L_n/T_n	Error	L_n/T_n	Error	L_n/T_n	Error
0.5	0.70	0.02	0.93	0.03	0.99	0.03	1.25	0.04	1.28	0.04	1.19	0.04							1.99	0.06	1.50	0.05	1.35	0.04
1.5	0.93	0.03	1.06	0.03	1.02	0.03	1.17	0.04	1.30	0.04	1.18	0.04	1.28	0.04	0.82	0.03	0.96	0.03	1.21	0.04	1.13	0.03	1.13	0.04
2.5	1.21	0.04	1.14	0.03	1.07	0.03	0.71	0.02	0.79	0.02	0.80	0.02	0.72	0.02	0.75	0.02	0.79	0.02	1.12	0.03	1.15	0.04	1.15	0.04
3.5	1.00	0.03	1.08	0.03	1.10	0.03	0.84	0.03	1.06	0.03	1.00	0.03							1.55	0.05	1.28	0.04	1.18	0.04
4.5	0.86	0.03	1.02	0.03	1.05	0.03	1.00	0.03	1.10	0.03	1.00	0.03	1.18	0.04	1.03	0.03	0.92	0.03	1.19	0.04	1.05	0.03	1.08	0.03
5.5	0.73	0.02	0.80	0.02	0.89	0.03	1.14	0.03	1.26	0.04	1.14	0.04							1.26	0.04	0.96	0.03	0.94	0.03
6.5	0.79	0.02	1.00	0.03	1.00	0.03	0.71	0.02	1.00	0.03	1.00	0.03	1.12	0.03	0.92	0.03	0.83	0.03	1.00	0.03	1.00	0.03	1.00	0.03
7.5	1.02	0.03	1.15	0.04	1.10	0.03							0.82	0.03	0.79	0.02	0.83	0.03	1.10	0.03	0.90	0.03	0.88	0.03
8.5	0.72	0.02	0.78	0.02	0.84	0.03							1.35	0.04	1.10	0.03	0.96	0.03	1.01	0.03	0.92	0.03	0.91	0.03
9.5	1.27	0.04	1.15	0.04	1.09	0.03													1.18	0.04	0.99	0.03	0.90	0.03
10.5	0.70	0.02	1.03	0.03	1.08	0.03							0.84	0.03	0.81	0.02	0.82	0.03	1.31	0.04	1.00	0.03	0.92	0.03
11.5	0.49	0.02	0.57	0.02	0.64	0.02													1.30	0.04	1.06	0.03	0.97	0.03
12.5	0.40	0.01	0.63	0.02	0.70	0.02							0.90	0.03	0.86	0.03	0.86	0.03	0.98	0.03	0.93	0.03	0.93	0.03
13.5													1.00	0.03	1.00	0.03	1.00	0.03						
14.5																								
15.5																								
16.5																								
17.5																								
18.5																								
19.5																								

Table S6. Raw L_n/T_n data used for fitting sample BALL02 in Fig. 5D-F.

	Core 1						Core 2						Core 3					
	IR_{50}		$pIRIR_{150}$		$pIRIR_{225}$		IR_{50}		$pIRIR_{150}$		$pIRIR_{225}$		IR_{50}		$pIRIR_{150}$		$pIRIR_{225}$	
Depth (mm)	L_n/T_n	Error	L_n/T_n	Error	L_n/T_n	Error	L_n/T_n	Error	L_n/T_n	Error	L_n/T_n	Error	L_n/T_n	Error	L_n/T_n	Error	L_n/T_n	Error
0.5																		
1.5							0.00	0.00	0.04	0.00	0.16	0.01	0.01	0.00	0.02	0.00	0.04	0.00
2.5							0.01	0.00	0.15	0.01	0.40	0.01	0.03	0.00	0.46	0.01	0.61	0.02
3.5	0.39	0.01	0.89	0.03	0.91	0.03	0.35	0.01	0.93	0.03	0.91	0.03	0.16	0.01	1.08	0.03	1.03	0.03
4.5	1.21	0.04	1.05	0.03	1.03	0.03	0.80	0.02	0.98	0.03	1.03	0.03	0.87	0.03	1.29	0.04	1.17	0.04
5.5	1.05	0.03	0.96	0.03	1.04	0.03	1.16	0.04	1.24	0.04	1.19	0.04	0.84	0.03	1.12	0.03	1.09	0.03
6.5	1.02	0.03	0.95	0.03	0.97	0.03							0.99	0.03	1.20	0.04	1.12	0.04
7.5	0.98	0.03	0.83	0.03	0.87	0.03	1.06	0.03	1.04	0.03	1.01	0.03	0.96	0.03	1.09	0.03	1.01	0.03
8.5	1.04	0.03	1.02	0.03	1.03	0.03	1.15	0.03	1.18	0.04	1.15	0.04	0.90	0.03	1.16	0.04	1.08	0.03
9.5	0.94	0.03	0.93	0.03	0.94	0.03	1.23	0.04	1.06	0.03	0.98	0.03	0.92	0.03	1.10	0.03	1.07	0.03
10.5	0.92	0.03	0.98	0.03	0.99	0.03	1.40	0.04	1.22	0.04	1.14	0.04	1.00	0.03	1.00	0.03	1.00	0.03
11.5							1.03	0.03	1.12	0.03	1.17	0.04						
12.5	1.13	0.03	1.02	0.03	1.01	0.03	1.01	0.03	1.09	0.03	1.05	0.03						
13.5	1.15	0.04	0.93	0.03	0.93	0.03												
14.5	1.00	0.03	1.00	0.03	1.00	0.03	1.02	0.03	1.07	0.03	1.08	0.03						
15.5	1.05	0.03	0.92	0.03	0.94	0.03	1.00	0.03	1.00	0.03	1.00	0.03						
16.5	1.14	0.03	1.06	0.03	1.04	0.03												
17.5																		
18.5																		
19.5																		

Table S7. Raw L_n/T_n data used for fitting sample BALL03 in Fig. 5G-I.

	Core 1						Core 2						Core 3					
	IR_{50}		$pIRIR_{150}$		$pIRIR_{225}$		IR_{50}		$pIRIR_{150}$		$pIRIR_{225}$		IR_{50}		$pIRIR_{150}$		$pIRIR_{225}$	
Depth (mm)	L_n/T_n	Error	L_n/T_n	Error	L_n/T_n	Error	L_n/T_n	Error	L_n/T_n	Error	L_n/T_n	Error	L_n/T_n	Error	L_n/T_n	Error	L_n/T_n	Error
0.5													0.00	0.00	0.01	0.00	0.03	0.00
1.5													0.01	0.00	0.04	0.00	0.11	0.00
2.5	0.00	0.00	0.07	0.00	0.26	0.01	0.01	0.00	0.26	0.01	0.64	0.02	0.01	0.00	0.15	0.00	0.34	0.01
3.5							0.01	0.00	0.33	0.01	0.62	0.02	0.04	0.00	0.52	0.02	0.76	0.02
4.5	0.06	0.00	0.72	0.02	0.76	0.02	0.07	0.00	0.80	0.02	0.98	0.03	0.33	0.01	0.85	0.03	0.85	0.03
5.5	0.25	0.01	0.86	0.03	0.78	0.02	0.39	0.01	0.88	0.03	0.95	0.03	0.78	0.02	0.91	0.03	0.90	0.03
6.5	1.11	0.03	1.03	0.03	0.92	0.03	0.78	0.02	1.12	0.03	1.16	0.04	0.75	0.02	0.75	0.02	0.80	0.02
7.5	1.29	0.04	1.17	0.04	1.04	0.03	0.88	0.03	0.98	0.03	1.01	0.03	0.88	0.03	0.86	0.03	0.92	0.03
8.5	1.06	0.03	1.03	0.03	0.97	0.03	0.74	0.02	1.00	0.03	1.11	0.03	0.99	0.03	0.93	0.03	0.95	0.03
9.5	1.07	0.03	1.12	0.03	1.05	0.03	1.00	0.03	1.00	0.03	1.00	0.03	1.15	0.04	1.09	0.03	1.06	0.03
10.5	1.15	0.03	1.04	0.03	1.00	0.03							1.16	0.04	1.07	0.03	1.04	0.03
11.5	1.07	0.03	1.00	0.03	0.92	0.03							1.01	0.03	0.95	0.03	0.97	0.03
12.5	1.12	0.03	1.01	0.03	0.97	0.03							1.00	0.03	1.00	0.03	1.00	0.03
13.5	1.29	0.04	1.03	0.03	0.97	0.03												
14.5	1.13	0.03	1.15	0.04	1.09	0.03												
15.5	0.99	0.03	0.95	0.03	0.93	0.03												
16.5	1.00	0.03	1.00	0.03	1.00	0.03												
17.5																		
18.5																		
19.5																		

Erosion rates in a wet, temperate climate derived from rock luminescence techniques

Rachel K. Smedley[1], David Small[2], Richard S. Jones[2, 3], Stephen Brough[1], Jennifer Bradley[1], Geraint T.H. Jenkins[4]

[1] School of Environmental Sciences, University of Liverpool, Liverpool, UK.

[2] Department of Geography, Durham University, South Road, Durham, UK.

[3] School of Earth, Atmosphere and Environment, Monash University, Melbourne, Australia.

[4] Independent researcher: Powys, Wales, UK

Correspondence to: Rachel K. Smedley (rachel.smedley@liverpool.ac.uk)

Abstract

A new luminescence erosion-meter has huge potential for inferring erosion rates on sub-millennial scales for both steady and transient states of erosion, which is not currently possible with any existing techniques capable of measuring erosion. This study applies new rock luminescence techniques to a well-constrained scenario provided by the Beinn Alligin rock avalanche, NW Scotland. Boulders in this deposit are lithologically consistent, have known cosmogenic nuclide ages, and independently-derived Holocene erosion rates. We find that luminescence-derived exposure ages for the Beinn Alligin rock avalanche were an order of magnitude younger than existing cosmogenic nuclide exposure ages, suggestive of high erosion rates (as supported by field evidence of quartz grain protrusions on the rock surfaces). Erosion rates determined by luminescence were consistent with independently-derived rates measured from boulder-edge roundness. Inversion modelling indicates a transient state of erosion reflecting the stochastic nature of erosional processes over the last ~4.5 ka in the wet, temperate climate of NW Scotland. Erosion was likely modulated by known fluctuations in moisture availability, and to a lesser extent temperature, which controlled the extent of chemical weathering of these highly-lithified rocks prior to erosion. The use of a multi-elevated temperature, post-infra-red, infra-red stimulated luminescence (MET-pIRIR) protocol (50, 150 and 225°C) was advantageous as it identified samples with complexities introduced by within-sample variability (e.g. surficial coatings). This study demonstrates that the luminescence erosion-meter can infer accurate erosion rates on sub-millennial scales and identify transient states of erosion (i.e. stochastic processes) in agreement with independently-derived erosion rates for the same deposit.

1. Introduction

Rock erosion is dependent upon a variety of internal (e.g. mineralogy, grainsize, porosity, structures) and external (e.g. temperature, moisture availability, snow cover, wind, aspect) factors. Chemical and/or physical weathering of rocks (or rock

decay; Hall et al. 2012) breaks down the surficial materials making them available for transportation (i.e. erosion), where the rates and processes of degradation is primarily controlled by the rock lithology (e.g. Twidale, 1982; Ford and Williams, 1989). For boulders with similar lithologies, the erosion rate is conditioned by weathering principally caused by moisture availability, but also temperature, and in some cases biological factors (Hall et al. 2012). It is widely reported that warmer temperatures increase most rates of chemical activity, while sub-zero temperatures arrest chemical activity on a seasonal basis. However, cold temperatures alone do not preclude chemical weathering (Thorn et al. 2001). As such, rock erosion rates will be sensitive to changing climate (moisture availability, temperature) such as that experienced throughout the Late Holocene (i.e. last 4 ka) (e.g. Charman, 2010), in addition to that forecast for the future due to anthropogenic climate change (e.g. Stocker et al. 2013). Measuring erosion rates over shorter ($\leq 10^3$ a) and longer ($\geq 10^4$ a) integration times is advantageous as each targets a different phenomenon of erosion. Longer timeframes will inform on how landscapes respond to changing large-scale climatic and tectonic conditions (e.g. Herman et al. 2010), whereas shorter timeframes assess local or regional responses to shorter-lived environmental conditions (e.g. climate fluctuations). A number of techniques can constrain long-term, landscape erosion rates on $\geq 10^4$ a timeframes, such as cosmogenic nuclides (e.g. Lal,1991; Braun et al. 2006; Balco et al. 2008) or thermochronology (Reiners and Brandon, 2006). While observational measurements on very short timeframes $\leq 10^2$ a are performed with both direct contact (e.g. Hanna, 1966; High and Hanna, 1970; Trudgill et al. 1989) and non-contact (e.g. Swantesson, 1989; Swantesson et al. 2006) techniques. However, until now it has been difficult to constrain erosion rates on 10^2 to 10^3 a timeframes due to a lack of techniques with the required sensitivity and resolution.

The luminescence signal within mineral grains (quartz and feldspar) is reset when a rock surface is exposed to sunlight for the first time (e.g. Habermann et al. 2000; Polikreti et al. 2002; Vafiadou et al. 2007). With continued exposure the luminescence signal resetting in the mineral grains propagates to increasing depths (i.e. the luminescence depth profile is a function of time). Improved understanding of this fundamental principle has led to the development of new applications of luminescence; constraining the timing of rock exposure events (Laskaris and Liritzis, 2011; Sohbati et al. 2011; Lehmann et al. 2018) and rock surface erosion rates (Sohbati et al. 2018; Lehmann et al. 2019a,b). Brown (2020) combine these phenomena within model simulations to explore different sample histories of exposure and burial, informing geomorphological interpretations of luminescence depth profiles measured in samples collected from the natural environment. Here, we investigate erosion rates, rather than weathering rates as the luminescence technique specifically measures the light penetration into a rock surface after the removal of material (i.e. erosion), occurring after the in-situ rock breakdown (i.e. weathering). Luminescence depth profiles are a product of the competing effects of time (which allows the bleaching front to propagate to greater depths) and erosion (which exhumes the bleaching front closer to the surface). Existing studies have suggested that rock luminescence exposure dating is only feasible for very short timeframes (e.g. <300 a; Sohbati et al. 2018) as light penetrates faster than the material can be removed, and/or in settings where erosion rates are <1 mm/ka (Lehmann et al. 2018). Beyond this, the dominant control on the luminescence depth profile is erosion, rather than time, hence if time can be parameterised, then erosion can be determined (and vice versa). Recent findings from erosion simulations compared with

measured data have shown that the erosion rates derived from luminescence depth profiles can be accurate even where stochastic erosion was experienced in nature (Brown and Moon, 2019).

New luminescence techniques have the potential to derive 10^2 to 10^3 a scale erosion rates because of two important characteristics: (1) measurable luminescence depth profiles can develop in a rock surface over extremely short durations of sunlight exposure (e.g. days; Polikreti et al. 2003, or years; Lehmann et al. 2018); and (2) luminescence depth profiles are sensitive to mm-scale erosion. Conversely, cosmogenic nuclides are sensitive to m-scale erosion, depending on the density (e.g. Lal, 1991). Therefore, the new luminescence erosion-meter has the potential to provide a step-change in capabilities of measuring erosion rates on currently impossible 10^2 to 10^3 a timeframes. However, its application has been limited to few studies (e.g. Sohbati et al. 2018; Lehmann et al. 2019b) validated against long-term erosion rates of landscape evolution from global or regional datasets rather than local, independently-constrained erosion rates derived from the same rock type.

This study tests the accuracy and applicability of rock erosion rates inferred from luminescence techniques in a new latitudinal (57°N) and climate (wet, temperate) setting with independently-constrained erosion rates. The Beinn Alligin rock avalanche in NW Scotland (Fig. 1) provides a well-constrained test scenario as: (1) the boulders were sourced from a single fault-bounded failure scarp occurring within sandstones of the Torridonian group (i.e. rocks are likely to be lithologically consistent); (2) all boulder samples share an identical exposure history as they were deposited by a single, instantaneous event (Ballantyne and Stone, 2004); (3) independent cosmogenic exposure ages constrain the timing of the rock avalanche (Ballantyne and Stone, 2004); and (4) independently-derived erosion rates over the last ~4 ka for the boulders of the Beinn Alligin rock avalanche uniquely provide constraints on erosion rates (Kirkbride and Bell, 2010).

2. Theoretical background

The propagation of a bleaching front (i.e. the depth at which the luminescence signal has been reduced by 50 %) into a rock surface can be described by a double exponential function (Eq. 1), where L_x is the luminescence measured with depth (x) from the rock surface, L_0 is the saturation limit for this sample (determined experimentally), t is the exposure time, $\overline{\sigma\varphi_0}$ is the intensity of light of a specific wavelength at the rock surface, and μ is the light attenuation coefficient. To determine the exposure time (t) of a rock surface (and also erosion rates), it is necessary to parameterise μ and $\overline{\sigma\varphi_0}$, which are likely unique to any specific rock lithology and natural sunlight conditions (e.g. latitude, cloudiness) of the sample being dated, respectively. Therefore, to provide accurate luminescence exposure ages (and also erosion rates), μ and $\overline{\sigma\varphi_0}$ must be calibrated using samples of known-age with the same lithology and natural sunlight conditions (e.g. a nearby road-cutting).

$$L_x = L_0 e^{\overline{-\sigma\varphi_0} t e^{-\mu x}} \quad (1)$$

Studies have applied rock luminescence techniques (mostly exposure dating) to a variety of lithologies including granites, gneisses (Lehmann et al. 2018, 2019a,b; Meyer et al. 2019), sandstones (Sohbati et al. 2012; Chapot et al. 2012; Pederson et al. 2014), quartzites (Gliganic et al. 2019) and carbonate limestone (Brill et al. 2021). These studies showed that μ is highly dependent upon the rock lithology, where mineralogy has a strong control on the rock transparency. This is supported by direct measurements of μ for a variety of lithologies (greywacke, sandstone, granite, and quartzite) using a spectrometer (Ou et al.

2018). In addition to mineralogy, it has also been shown that the precipitation of dark Fe-hydroxides (Meyer et al. 2018) and rock varnishing (or weathering crusts) (e.g. Luo et al. 2019) can influence μ by changing the rock transparency principally at the rock surface. Mineralogy is broadly a constant variable over time. However, the formation of precipitates or rock varnishing can be time-variable due to changing environmental factors external to the rock; thus, we should consider the possibility that μ may be time-variable. Consequently, investigating the rock opacity of each sample is important to assess whether the known-age samples used to parameterise μ and $\overline{\sigma\varphi_0}$ were consistent with the unknown-age samples used for exposure dating or erosion rates.

Since the introduction of the new rock luminescence techniques, most studies on K-feldspar (except Luo et al. 2019) have only utilised the IR_{50} signal as it bleaches more efficiently with depth into rock surfaces compared to higher temperature post-IR IRSL signals (e.g. Luo et al. 2019; Ou et al. 2018). However, electron multiplying charged coupled device (EMCCD) measurements of four rock types (quartzite, orthoclase and two different granites) have shown that the post-IR IRSL signals of rock slices were dominated by K-feldspars, while Na-rich feldspars can contribute towards the IR_{50} signal (Thomsen et al. 2018). It is possible that the different IRSL signals will have different luminescence characteristics (e.g. bleaching rates, fading rates, saturation levels, light attenuation, internal mineral composition) that could be exploited during measurements. Luo et al. (2019) used the post-IR IRSL signals with a multiple elevated temperature (MET) protocol (50, 110, 170, 225 °C) to demonstrate that all the IRSL signals provide luminescence depth profiles, but the lower temperature signals penetrated further into the rock with depth. The authors fit the four IRSL signals to improve the accuracy of their parameterisation of μ and $\overline{\sigma\varphi_0}$. However, no study has yet used the MET-post IR IRSL protocol to exploit the differing luminescence characteristics of the successively-measured IRSL signals to provide an internal quality control check on the reliability of the measured data, i.e. the luminescence depth profile will penetrate deeper in to the rock for the IR_{50} signal than the $pIRIR_{150}$ signal, which in turn will penetrate deeper than the $pIRIR_{225}$ signal. However, all three signals should determine the same erosion rates if the model parameterisation (i.e. μ and $\overline{\sigma\varphi_0}$) is accurate. To maximise the potential information that could be derived from the samples, this study applied a MET-post IR IRSL protocol (50, 150 and 225 °C).

For determining erosion rates for rock surfaces of known exposure age, Sohbati et al. (2018) used a confluent hypergeometric function to provide an analytical solution, but assuming only steady-state erosion. Lehmann et al. (2019a) provide a numerical approach that exploits the differential sensitivities to erosion of the luminescence (short-term) and cosmogenic nuclide (longer-term) techniques to erosion to infer erosion histories (steady state and transient over time) for rock surfaces. This approach uses the experimental data from the luminescence depth profiles and the ^{10}Be concentrations for each sample. Modelling of the luminescence depth profiles accounts for the electron trapping dependent upon the environmental dose-rate and D_0 but does not consider athermal loss of the signal (i.e. anomalous fading) as it has been demonstrated to have a negligible impact upon the luminescence depth profiles (Lehmann et al. 2019a). Modelling of the ^{10}Be concentrations assumes no inheritance of cosmogenic nuclides from prior exposure, and that the ^{10}Be concentrations have been corrected for sample depth, density and topographical shielding. The luminescence depth profiles and cosmogenic nuclide concentrations

are solved simultaneously for two unknowns: the exposure duration and the erosion history as defined by a step function (e.g. zero erosion for an initial period of time followed by an instant increase to a constant erosion rate). Forward modelling is used to calculate all of the possible luminescence depth profiles for these synthetic erosion and exposure histories, which are then validated using inversion models against the experimental data to determine the combinations with the highest likelihood. A forbidden zone is defined by combinations of erosion rate and duration that are not possible given the measured ^{10}Be concentrations; these solutions are excluded from the parameter ranges used for the inversion model. For example, the forbidden zone identified in the inversion model profile shown in Fig. 7A is restricted to ranges from ca. 10^4 mm/ka for durations of ca. 100 a to ca. 10^3 mm/ka for ca. >3000 a.

The approach of Lehmann et al. (2019a) can model synthetic erosion histories in both steady and transient states. Steady state erosion is defined as a constant erosion rate over a portion of the total duration of surface exposure. Transient erosion is typical of shorter exposure histories where a steady state of erosion has not yet been reached and is defined by erosion rates that decrease linearly with increased timing of erosion onset within the parameter space. An illustration of this is provided by Fig. 7A where transient erosion rates of between ca. 10^4 mm/ka were inferred for a minimum duration of ca. ≤1 a, and extending up to ca. 10^3 mm/ka for durations up to ca. 50 a. Beyond ca. 50 a, a steady state of erosion was reached at a constant erosion rate of ca. 10^3 mm/ka, represented by the flattening of the profile with the highest likelihood. Alternatively, a profile indicative of a transient state of erosion where no steady state has been established is illustrated by Fig. 7D where transient erosion rates of between ca. 10^2 mm/ka were inferred for a minimum duration of ca. ≤1 a, and extending up to ca. 10^1 mm/ka for durations beyond ca. 200 a. This numerical approach (Lehmann et al. 2019a) allows erosion history to be considered as non-constant in time (i.e. transient), in addition to steady-state, and so it is more indicative of the stochastic erosional processes (driven by temperature, precipitation, snow cover, wind) in nature.

3. The Beinn Alligin rock avalanche

Today, average winter and summer temperatures in NW Scotland are 7°C and 18°C, respectively, while average annual precipitation (mostly rainfall) is high (ca. 2,300 mm/a) (Met Office, 2021). The Beinn Alligin rock avalanche (57°35'N, 05°34'W) is a distinct, lobate deposit of large boulders that is 1.25 km long and covers an area of 0.38 km^2 (Fig. 1). It has previously been ascribed various origins including a rockslide onto a former corrie glacier (e.g. Ballantyne, 1987; Gordon, 1993) and a former rock glacier (Sissons, 1975; 1976). However, on the basis of cosmogenic exposure dates that constrain its deposition to the Late Holocene it is now widely accepted to have been deposited by a rock-slope failure that experienced excess run-out (e.g. a rock avalanche). The source is a distinct, fault-bounded failure scar on the southern flank of Sgurr Mor, the highest peak of Beinn Alligin (Ballantyne, 2003; Ballantyne and Stone, 2004). The rock avalanche is comprised of large, poorly-sorted boulders and is calculated to comprise a total volume of 3.3 – 3.8 x 10^6 m^3, equivalent to a mass of 8.3 – 9.5 Mt (Ballantyne and Stone, 2004). The source lithology is Late Precambrian Torridonian sandstone strata. The Torridonian sandstones are reddish or reddish brown terrestrial sedimentary rocks deposited under fluvial or shallow lake conditions (Stewart, 1982). The sandstones maintained a common origin throughout deposition (Stewart, 1982) and are thus largely

consistent in mineralogy (dominated by quartz, and alkali and plagioclase feldspar) although there are some local variations in grain size (Stewart and Donnellan, 1992).

The ^{10}Be concentrations of three boulders used for cosmogenic nuclide exposure dating were internally consistent evidencing a single, catastrophic mass movement event which occurred 4.54 ± 0.27 ka (re-calculated from Ballantyne and Stone, 2004). Consequently, the boulders were very unlikely to have previously been exposed to cosmic rays or sunlight prior to transport and deposition. Moreover, the large size of the flat-topped boulders (>2 x 2 x 2 m) and lack of finer sediment matrix within the rock avalanche deposit, suggested that post-depositional movement or exhumation is unlikely. The Torridonian sandstones are hard, cemented rocks (Stewart, 1984; Stewart and Donnellson, 1992) susceptible to granular disintegration (e.g. Ballantyne and Whittington, 1987). Given its inland location, salt weathering is likely negligible. Kirkbride and Bell (2010) estimated edge-rounding rates of ~3.3 mm/ka for a suite of Torridonian sandstone boulder samples from a range of sites in NW Scotland under the warmer, wetter climates of the Holocene. A notably higher erosion rate of 12 mm/ka was specifically determined for the Beinn Alligin rock avalanche. Kirkbride and Bell (2010) suggest that this higher erosion rate, in comparison to the other sites, is likely due to inherited rock roundness caused by abrasion during the high-magnitude depositional event. Additionally, minor differences in lithology cannot be ruled out (e.g. Twidale, 1982; Ford and Williams, 1989). Consequently, we consider the range ~3.3 to 12 mm/ka as a reasonable estimation of the Holocene erosion rate of the Torridonian sandstone boulders that comprise the Beinn Alligin rock avalanche.

4. Methods

A total of six rock samples were taken from the Torridonian sandstones in NW Scotland (Fig. 1). Three samples were taken from three different road-cuttings of known age to calibrate the values of μ and $\overline{\sigma\varphi_0}$: ROAD01 (0.01 a), ROAD02 (57 a; Fig. S1a), ROAD03 (44 a; Fig. S1b). Three further samples were taken from flat-topped, angular boulders that were part of the Beinn Alligin rock avalanche deposit: BALL01, BALL02 and BALL03 (Fig. 1D). Portions of the original boulder or bedrock sample were collected in the field in daylight and immediately placed into opaque, black sample bags. All samples were taken from surfaces perpendicular to incoming sunlight to ensure that the daylight irradiation geometry was similar between calibration and dating samples (cf. Gliganic et al. 2019).

4.1 Luminescence measurements

To calculate the environmental dose-rate throughout burial for each sample (Table 1), U, Th and K concentrations were measured for ca. 80 g of crushed bulk sample using high-resolution gamma spectrometry. Internal dose-rates were calculated assuming an internal K-content of 10 ± 2 % (Smedley et al. 2012) and internal U and Th concentrations of 0.3 ± 0.1 ppm and 1.7 ± 0.4 ppm (Smedley and Pearce, 2016), in addition to the measured average grain sizes for each sample. Cosmic dose-rates were calculated after Prescott and Hutton (1994). For measuring the luminescence depth profiles, sample preparation was performed under subdued-red lighting conditions to prevent contamination of the luminescence signal. Rock cores ~7 mm in diameter and up to 20 mm long were drilled into the rock surface using an Axminster bench-top, pillar drill equipped with a water-cooled, diamond-tipped drillbit (~9 mm diameter). Each core was sliced at a thickness of ~0.7 mm using a Buehler

IsoMet low-speed saw equipped with a water-cooled, 0.3 mm diameter diamond-tipped wafer blade. All slices were then mounted in stainless steel cups for luminescence measurements.

Luminescence measurements were performed on a Risø TL/OSL reader (TL-DA-15) with a $^{90}Sr/^{90}Y$ beta irradiation source. Heating was performed at 1°C/s and the rock slices were held at the stimulation temperature (i.e. 50, 150 and 225°C) for 60 s prior to IR stimulation to ensure all of the disc was at temperature before stimulating (cf. Jenkins et al. 2018). IRSL signals were detected in blue wavelengths using a photo-multiplier tube fitted with Schott BG-39 (2 mm thickness) and Corning 7-59 (2 mm thickness) filters. A MET-post-IR IRSL sequence (Table S1) was used to determine IRSL signals at three different temperatures (50, 150 and 225°C) successively, hereafter termed the IR_{50}, $pIRIR_{150}$ and $pIRIR_{225}$ signals. Luminescence depth profiles were determined for each core by measuring the natural signal (L_n) normalised using the signal measured in response to a 53 Gy test-dose (T_n), hereafter termed the L_n/T_n signal. The IRSL signal was determined by subtracting the background signal (final 20 s, 40 channels) from the initial signal (0 – 3.5 s, 7 channels). The large test-dose (53 Gy) was used to reduce the impact of thermal transfer/incomplete resetting of the IRSL signal between measurements (after Liu et al. 2016).

D_e values were determined for the shallowest disc and the deepest disc from one core of each sample to quantify the natural residual dose and saturation limit (L_0, Eq. 1), respectively. Fading rates (*g*-values, Aitken 1985) were determined for three discs of each sample and normalised to a t_c of two days (Huntley and Lamothe 2001). The weighted mean and standard error of the g-values for all discs were 3.7 ± 0.4 %/dec. (IR_{50}), 1.0 ± 0.5 %/dec. ($pIRIR_{150}$) and 1.0 ± 0.5 %/dec. ($pIRIR_{225}$). The large uncertainties on the individual *g*-values measured were derived from uncertainty in the fit of the data, which is typical of fading measurements (e.g. Smedley et al. 2016). The fading rates were in line with previous measurements of IRSL signals (e.g. Roberts 2012; Trauerstein et al. 2014; Kolb and Fuchs 2018). Lehmann et al. (2019a) performed sensitivity tests of the shape of the luminescence depth profiles (IR_{50}) with a high and low g-value end-members and these simulations demonstrated that athermal loss of signal has a minimal impact upon the IRSL depth profile shape; thus, athermal loss (i.e. fading rates) was not considered in calculations.

Previous studies have shown that the IR_{50} signal bleached faster than the pIRIR signals (Smedley et al., 2015). To test the inherent bleaching rates of the feldspars in our samples, artificial bleaching experiments were performed on seven discs from all six samples (n.b. these experiments do not test for variations in light attenuation with depth). All previously-analysed discs were given a 105 Gy dose, then subjected to different exposure times in a solar simulator (0 m, 1 m, 10 m, 30 m, 1 h, 4 h and 8 h) and the normalised luminescence signals (IR_{50}, $pIRIR_{150}$ and $pIRIR_{225}$) were measured (Fig. S2). The results show some variations after 1 m of solar simulator exposure. However, luminescence signals reduced to 2 – 6 % (IR_{50}), 6 – 11 % ($pIRIR_{150}$) and 14 – 22 % ($pIRIR_{225}$) of the unexposed light levels after 1 h and 1 – 2 % (IR_{50}), 2 – 3 % ($pIRIR_{150}$) and 4 – 7 % ($pIRIR_{225}$) after 8 h. This indicates that within our samples the minerals emitting the IRSL signals (i.e. K-feldspar) have similar inherent bleaching rates when exposed to longer durations of time (i.e. > 8 h in the solar simulator).

4.2 Rock composition

After luminescence measurements were performed, each rock slice (e.g. Fig. 2) was analysed to investigate potential changes in rock composition with depth (inferred by opacity and grainsize). The average down-core grainsize of each sample was measured under an optical microscope using *Infinity Analyze*. For each rock slice of an example core per sample, ten randomly-selected grains were measured and the mean and standard deviation grainsize were calculated per core and plotted against the core depths (Fig. 3B). Down-core red-green-blue (RGB) values were determined for each sample to investigate whether there was any colour variation within the sample, and externally between samples; thus, providing a semi-quantitative tool to detect variability in rock opacity (Meyer et al. 2018). Raster images of RGB were obtained for each rock slice using an EPSON Expression 11000XL flatbed scanner at 1200 dpi resolution (e.g. Fig. S3). Mean and standard deviations of the RGB values (e.g. Fig. 3A) for each rock slice were calculated using the *raster* package in R (version 2.9-23; Hijmans, 2019).

5. Results

5.1 Luminescence depth profiles

The luminescence depth profiles (IR_{50}, $pIRIR_{150}$ and $pIRIR_{225}$) (Fig. 4) record bleaching fronts caused by sunlight exposure for all of the known-age samples. The luminescence depth profile measured for core 3 of sample ROAD02 (Fig. 4 G,H,J) was inconsistent with cores 1 and 2, giving high standard deviation values for the IR_{50} (1.2), $pIRIR_{150}$ (1.1) and $pIRIR_{225}$ (0.9) signals; thus, core 3 was removed from subsequent analysis (likely sample preparation issues related to drilling preservation of the weathered surface). The luminescence depth profiles for the remaining replicate cores for all three samples were broadly consistent within each rock sample with mean standard deviations ranging from 0.2 – 0.8.

The luminescence depth profiles (Fig. 4) for the IR_{50} signal were consistent with the increasing sunlight exposure ages for ROAD01 (0.01 a), ROAD03 (44 a) and ROAD02 (57 a), with bleaching fronts at 0.75 mm, 4.00 mm and 4.75 mm, respectively (Fig. S5a). This indicated that the depth of the IR_{50} bleaching front was dominated by exposure duration for the known-age samples as expected. Similarly, the $pIRIR_{150}$ and $pIRIR_{225}$ bleaching fronts were shallower in sample ROAD01 (0.75 mm) compared to ROAD02 and ROAD03 (2.00 – 3.00 mm), reflecting the younger exposure duration of ROAD01. However, the $pIRIR_{150}$ and $pIRIR_{225}$ bleaching fronts were at similar depths (2.75 and 3.00 mm and 2.00 and 2.50 mm respectively) for both ROAD02 (57 a) and ROAD03 (44 a). This suggests that either another factor is influencing light penetration with depth in these rocks (e.g. small differences in the orientation of the sampled rock faces; Fig. S1) or that the pIRIR signals cannot resolve between a 57 a and 44 a exposure history (difference of only 13 a). Note that the inferred models shown in Fig. 4 were fitted using the $\overline{\sigma\varphi_0}$ and μ values included in each figure. See Section 5.2 for further explanation of the estimation of the model parameters.

The luminescence depth profiles measured for the unknown-age samples BALL02 and BALL03 using the IR_{50}, $pIRIR_{150}$ and $pIRIR_{225}$ signals (Fig. 5) recorded bleaching fronts caused by sunlight exposure. Conversely, the luminescence depth profile for sample BALL01 had saturated IRSL signals throughout the core and did not display any evidence of IRSL signal resetting with depth (Fig. 5A-C). A luminescence depth profile measured for a core drilled into the bottom surface (Bottom C1; Fig. 5A-C) confirmed that the bottom surface of BALL01 was also saturated. The lack of a bleaching front in

sample BALL01 is difficult to explain as the sample was taken in daylight and had seemingly identical characteristics to samples BALL02 and BALL03 (i.e. no lichen-cover or coatings preventing light penetration in the rock). Although all the samples were similar in colour/opacity (Fig. 3A), the surface of sample BALL01 was coarser grained than BALL02 and BALL03 (Fig. 2; Fig. 3B). Studies have shown that coarser grain sizes are more susceptible to mechanical weathering via grain detachment induced by chemical weathering (Israelli and Emmanuel, 2018). Thus, although care was taken when sampling to mark the surface of the rock and to measure the length of the rock cores before and after slicing, it is possible that the luminescence depth profile (likely <10 mm based on BALL02 and BALL03) was lost during sampling and/or sample preparation due to the presence of a fragile weathering crust, potentially with a sub-surface zone of weakness (e.g. Robinson and Williams, 1987). Furthermore, field observations showed the presence of a rock pool on the surface of the boulder sampled for BALL01, which is not present on BALL02 and BALL03 (Fig. 1D); thus, there is also potential that the surface sampled for BALL01 had experienced enhanced chemical weathering via trickle paths draining the rock pool. These are commonly linked to a greater density of micro-cracks in the uppermost millimetres of the rock (Swantesson, 1989, 1992). Consequently, we did not derive exposure ages or erosion rates from BALL01. Where rock pools are likely on boulders, the highest rock surface should be sampled for luminescence techniques to avoid the potential for pooling or trickle paths.

5.2 Estimation of model parameters

To determine an apparent exposure age or erosion rate from the measured luminescence depth profiles, the variables that control the evolution of a luminescence depth profile in a rock surface must be parameterised; specifically, the dose-rate ($\dot{D}$) (see Section 4.1), saturation level (D_0), $\overline{\sigma\varphi_0}$ and μ. D_0 was determined experimentally from saturated dose-response curves measured for the deepest rock slices of each sample. $\overline{\sigma\varphi_0}$ and μ were calibrated using Eq. (1) and the known-age samples (ROAD01, ROAD02 and ROAD03) of similar, suitable rock composition as determined by the down-core profiles of RGB and grainsize (Section 4.2). Note that ($\dot{D}$) is not considered in Eq. (1) but is used to determine an apparent exposure age or erosion rate and so needs to be measured for each sample (see Section 2). Down-core RGB values for all samples were internally consistent (Fig. 3A) as indicated by the relative standard deviation (RSD) range between 8 and 12 %. The down-core RGB values were also externally consistent between all samples (Fig. 3A), with the exception of the slightly darker-coloured sample ROAD01. However, measurements of grainsize (Fig. 3B) showed that the known-age sample ROAD02 (90 ± 23 μm) had a similar grainsize to the unknown-age samples BALL02 (73 ± 18 μm) and BALL03 (98 ± 19 μm), whereas ROAD01 (42 ± 9 μm) and ROAD03 (168 ± 56 μm) were finer and coarser grained, respectively. Given the similarity in colour and grainsize, it was considered most appropriate to calibrate $\overline{\sigma\varphi_0}$ and μ for the unknown age samples (BALL02 and BALL03) using known-age sample ROAD02.

The values of $\overline{\sigma\varphi_0}$ and μ were determined by fitting Eqn. (1) using the approach of Lehmann et al. (2019a). The inferred model (Eq. 1) had a good fit to the measured data for all samples and signals (Fig. 4) and μ and $\overline{\sigma\varphi_0}$ were calculated (Table 2; Fig. 6). For ROAD01, the parameters determined using the IR_{50} ($\mu = 3.2$ mm^{-1}, $\overline{\sigma\varphi_0} = 2.80e^{-4}$ s^{-1}), $pIRIR_{150}$ ($\mu = 3.1$ mm^{-1}, $\overline{\sigma\varphi_0} = 3.27e^{-5}$ s^{-1}) and $pIRIR_{225}$ ($\mu = 3.0$ mm^{-1}, $\overline{\sigma\varphi_0} = 2.88e^{-5}$ s^{-1}) signals were broadly consistent. For ROAD02, the

parameters differed between the IR_{50} ($\mu = 2.1$ mm^{-1}, $\overline{\sigma\varphi_0} = 6.67e^{-6}$ s^{-1}), $pIRIR_{150}$ ($\mu = 1.5$ mm^{-1}, $\overline{\sigma\varphi_0} = 1.73e^{-8}$ s^{-1}) and $pIRIR_{225}$ ($\mu = 2.8$ mm^{-1}, $\overline{\sigma\varphi_0} = 9.01e^{-8}$ s^{-1}) signals, but the values for each signal were broadly similar to the equivalent values determined for ROAD03 using the IR_{50} ($\mu = 2.7$ mm^{-1}, $\overline{\sigma\varphi_0} = 1.56e^{-5}$ s^{-1}), $pIRIR_{150}$ ($\mu = 1.5$ mm^{-1}, $\overline{\sigma\varphi_0} = 3.80e^{-8}$ s^{-1}) and $pIRIR_{225}$ ($\mu = 1.4$ mm^{-1}, $\overline{\sigma\varphi_0} = 1.70e^{-8}$ s^{-1}) signals. Given the similarity of $\overline{\sigma\varphi_0}$ and μ determined using all three IRSL signals for ROAD02 and ROAD03 and the difference in grainsizes (Fig. 3B), it suggests that grainsize has a minimal impact upon the attenuation of light into a rock surface in comparison to other factors (e.g. mineralogy, surficial coatings). The μ values for samples ROAD01, ROAD02 and ROAD03 determined using the IR_{50} signal in this study were comparable to μ values in existing literature for sandstones using K-feldspar e.g. 3.06 mm^{-1} (Ou et al. 2018). For sample ROAD01, μ and $\overline{\sigma\varphi_0}$ were similar for all three IRSL signals with large uncertainties (Fig. 6A-C) which is likely related to the shorter exposure age of this sample (0.01 a). The finer grain size and darker rock opacity of sample ROAD01 in comparison to ROAD02 and ROAD03 likely explained the larger values of μ (i.e. greater light attenuation with depth into the rock surface).

5.3 Apparent exposure ages and erosion rates

Luminescence exposure ages were determined from the luminescence depth profiles using μ and $\overline{\sigma\varphi_0}$ derived from sample ROAD02 for each of the IRSL signals (Table 3). For BALL03, the IR_{50} (387 ± 103 a), $pIRIR_{150}$ (296 ± 54 a) and $pIRIR_{225}$ (362 ± 49 a) signals all gave luminescence exposure ages in agreement within uncertainties. For BALL02, the three signals were inconsistent with one another. The $pIRIR_{225}$ signal (263 ± 30 a) was consistent with BALL03, but the IR_{50} (8 ± 2 a) and $pIRIR_{150}$ (66 ± 16 a) signals for BALL02 were younger than BALL03. All apparent exposure ages based on the different luminescence signals were at least one order of magnitude younger than the apparent exposure age based cosmogenic nuclide dating (4.54 ± 0.27 ka; Ballantyne and Stone, 2004). This was likely because erosion over time in this wet, temperate climate has removed material from the surface of the rock and created shallower luminescence depth profiles in comparison to a non-eroding profile; thus, the luminescence depth profile is dependent upon both exposure age and the erosion rate (Sohbati et al. 2018; Lehmann et al. 2019a).

To test whether erosion rates could be determined for the Beinn Alligin boulders from the luminescence depth profiles, we performed erosion rate modelling following the inversion approach of Lehmann et al. (2019) and constrained by the re-calculated cosmogenic nuclide age (Ballantyne and Stone, 2004). This approach defines an erosion history that follows a step function with an initial period of zero erosion, followed by an immediate increase to a constant erosion rate at a defined time. It attempts to recover parameter combinations (erosion rate and timing of erosion initiation) that are both consistent with the cosmogenic nuclide concentration and produce modelled luminescence profiles that match observations. For BALL02, both the IR_{50} and $pIRIR_{150}$ signals suggested that the system had approached a steady-state with erosion rates of 66 mm/ka (IR_{50}) and 9 mm/ka ($pIRIR_{150}$) applied over time periods >73 a and 593 a, respectively. However, the $pIRIR_{225}$ signal suggested a transient erosion state, where the luminescence signal could be derived from numerous pairs of erosion rates and initiation times from a maximum erosion rate of 310 mm/ka over a minimum time interval of 4 a to a minimum erosion rate of 12 mm/ka over a minimum time interval of 90 a. All three IRSL signals from sample BALL03 consistently suggested a system undergoing

a transient response to erosion, which was consistent with the $pIRIR_{225}$ signal of BALL02 (Fig. 7, Table 3). The IR_{50} signal for BALL03 derived a maximum erosion rate of 460 mm/ka over a minimum time interval of 3 a and a minimum erosion rate of 6 mm/ka over a minimum time interval of 231 a. The $pIRIR_{150}$ signal for BALL03 derived a maximum erosion rate of 100 mm/ka over minimum time interval of 19 a and a minimum erosion rate of 14 mm/ka over a minimum time interval of 137 a. The $pIRIR_{225}$ signal for BALL03 derived a maximum erosion rate of 180 mm/ka over a minimum time interval of 4 a and a minimum erosion rate of 11 mm/ka over a minimum time interval of 73 a.

At face value, the fit of the inferred erosion model to the experimental data for BALL02 using the IR_{50} (Fig. 5D) and $pIRIR_{150}$ (Fig. 5E) signals is better than the equivalent fits for BALL02 using the $pIRIR_{225}$ signal (Fig. 5F) and BALL03 using the IR_{50} (Fig. 5G), $pIRIR_{150}$ (Fig. 5H) and $pIRIR_{225}$ (Fig. 5I) signals. In the latter cases, the inferred erosion model is shallower than the experimental data. This could suggest that the $\overline{\sigma\varphi_0}$ and μ values were inaccurate, i.e. the attenuation of light with depth into the rock surface is lower in BALL02 ($pIRIR_{225}$ signal) and BALL03 (IR_{50}, $pIRIR_{150}$ and $pIRIR_{225}$ signals) than estimated by ROAD02. A possible explanation for this is that the surface of the roadcut sampled by ROAD02 (Fig. S1a) was orientated slightly differently to the Beinn Alligin rock avalanche boulders sampled by BALL02 and BALL03 (Fig. 1D), relative to the incoming sunlight (e.g. Gliganic et al. 2019). However, if the orientation of the known-age roadcut samples was even slightly inconsistent with the unknown samples, we would expect these inconsistencies to manifest similarly in all three MET signals for BALL02 and BALL03, which was not observed here. A factor that is common to the less well fitting profiles is that they define transient erosion states. This suggests that these surfaces experienced complex erosional histories over time whereby the erosion rate was time-varying. Consequently, it is possible that surficial weathering products may have changed in thickness and composition over time, which in turn could slightly vary the attenuation of light (Meyer et al. 2018; Luo et al. 2018), meaning that the calibration of $\overline{\sigma\varphi_0}$ and μ from ROAD02 here introduced uncertainty into the inferred erosion model as it was not time-varying. It is also possible that sample-specific measurements of $\overline{\sigma\varphi_0}$ and μ (e.g. Ou et al. 2018), rather than calibration from known-age samples, could reduce the uncertainty introduced by time-varying light attenuation. However, further investigation is required into the physical mechanisms of time-varying light attenuation in the context of surficial weathering and subsequent erosion, and the impacts upon inferred transient erosion rates.

6. Discussion

6.1 Luminescence depth profiles for the Beinn Alligin rock avalanche

Despite the similarity in rock opacity, grainsize, aspect and exposure history, the luminescence depth profiles for samples BALL02 and BALL03 from the Beinn Alligin rock avalanche were inconsistent (Fig. 5). We consider it unlikely that this lack of consistency was caused by local variations in erosion rates (e.g. due to microclimate, aspect etc; Hall et al. 2005, 2008) as there were discrepancies between all three IRSL signals of BALL02. We would expect local erosion rate variations between samples to be consistently recorded across each of the IRSL signals, assuming the model parameterisation (μ and $\overline{\sigma\varphi_0}$) were accurate. Specifically, and with all other things being equal, a locally-variable erosion rate would translate the bleaching front(s) closer to the rock surface by a proportionally consistent amount for each signal of a given sample.

Analysis of the rock opacity with depth (Section 4.2; Meyer et al. 2018) showed that sample BALL02 was more positively skewed towards darker colours than ROAD02 and BALL03 (Fig. S3, S4), with higher surficial values caused by Fe-staining. Fe-staining can occur on rock surfaces with seasonal rock pools and trickle paths (Swantesson, 1989, 1992). The presence of a thin Fe-coating (<1 mm) on the rock surface would have changed the intensity and wavelength of the net daylight flux received by individual grains (e.g. Singhvi et al.,1986; Parish, 1994) and likely increased light attenuation with depth (e.g. Meyer et al. 2018; Luo et al. 2018). Consequently, the parameterisation of μ and $\overline{\sigma\varphi_0}$ derived from sample ROAD02 would be inaccurate for BALL02. Interestingly, the similarity between BALL02 and BALL03 for the $pIRIR_{225}$ signal suggests that the presence of an Fe-coating altered the attenuation of the IR_{50} and $pIRIR_{150}$ signals to a lesser extent than the $pIRIR_{225}$ signal, but the reasons for this requires further investigation. The application of the MET-pIRIR rather than just the stand-alone IR_{50} signal protocol provided a major advantage as it identified samples where the parameterisation of μ and $\overline{\sigma\varphi_0}$ from known-age samples was complicated by factors such as surficial weathering coatings. Beyond this, it is possible that the MET-pIRIR protocol may be useful in identifying complex burial or exposure histories of rocks, similar to those that have been reported in previous studies but solely using the IR_{50} signal (e.g. Freiesleben et al. 2015; Brill et al. 2021). There is also potential to explore whether the different temperature IRSL signals of the MET protocol record different states of erosion (i.e. steady or transient states) within the same rock surface, whereby the post-IR IRSL signals that are attenuated greater would be more susceptible to transient states of erosion in comparison to the lower temperature signals, which measure luminescence depth profiles to greater depths within the rock surface.

The boulders from the Beinn Alligin rock avalanche have been subject to a temperate climate for the last ~4 ka. The luminescence depth profiles from the boulders demonstrated that on these timeframes and under these climatic conditions the technique was an erosion-meter, rather than a chronometer, as expected (Sohbati et al. 2018; Lehmann et al. 2019a). Lehmann et al. (2019a) noted that two of their samples, uncorrected for erosion, gave apparent luminescence exposure ages of ca. 640 a and <1 a compared to apparent cosmogenic nuclide ages of ca. 16.5 ka and 6.5 ka, respectively. It has thus been inferred that erosion rates >1 mm/ka can make interpretation of luminescence depth profiles in terms of an exposure age difficult without accurately constraining the erosion rate (Sohbati et al., 2018; Lehmann et al., 2018). This is consistent with the underestimation of luminescence exposure ages measured here for the Beinn Alligin rock avalanche (Table 3), which have been independently-dated to 4.54 ± 0.27 ka using cosmogenic nuclides (Ballantyne and Stone, 2004). Consequently, luminescence depth profiles for the Beinn Alligin rock avalanche can only be inferred in terms of erosion rates.

6.2 Luminescence as an erosion-meter

The numerical approach of Lehmann et al. (2019a) exploits the different sensitivities of the luminescence (short-term) and cosmogenic nuclide (longer-term) techniques to erosion to infer erosion histories (steady state and transient over time) for rock surfaces. Their modelling shows that the higher erosion rates (>100 mm/ka) can only be sustained over shorter time durations (up to decadal) while at the same time being consistent with cosmogenic nuclide measurements. For BALL03, transient erosion rates were derived using the IR_{50} (6 - 460 mm/ka), $pIRIR_{150}$ (14 - 100 mm/ka) and $pIRIR_{225}$ (11 - 180 mm/ka) signals. These

modelled transient erosion rates were broadly comparable to erosion rates inferred from luminescence depth profiles over comparable timeframes in previous studies: (i) rates between <0.038 ± 0.002 and 1.72 ± 0.04 mm/ka for glacial boulders and landslides (granite gneiss, granodorite and quartzite) in the Eastern Pamirs, China (Sohbati et al. 2018); and (ii) between 3.5 ± 1.2 mm/ka and 4,300 ± 600 mm/ka for glacially-modified, granitic bedrock in the French Alps (Lehmann et al., 2019b). This latter study modelled higher erosion rates (>100 mm/ka) over timescales from 10^1 to 10^3 a and lower erosion rates (<100 mm/ka) over longer time scales of 10^3 to 10^4 a. However, this comparison between modelled erosion rates does not account for the primary role that lithology has on weathering (e.g. Twidale, 1982; Ford and Williams, 1989). The sampled boulders in our study were composed of Torridonian sandstone, which has been reported to undergo granular disintegration (e.g. Ballantyne and Whittington, 1987), particularly around edges, and thus may have experienced higher erosion rates than the crystalline rocks (e.g. gneiss, granite) used in the studies of Sohbati et al. (2018) and Lehmann et al., 2019b.

A major advantage of applying this new erosion-meter technique to boulders of the Beinn Alligin rock avalanche was the existing constraints on Holocene erosion rates (~3.3 to 12 mm/ka) for Torridonian sandstones in NW Scotland inferred from boulder edge roundness measurements (Kirkbride and Bell, 2009). The long-term erosion rates inferred from luminescence depth profiles were consistent with the estimates provided by measuring the boulder-edge roundness, when considering the differing approaches and assumptions of each method. Firstly, the sampling approach for the luminescence depth profiles targeted the flat-top surface of the boulders where granular disintegration would have been reduced relative to the boulder edges and corners. Thus, the boulder-edge roundness based erosion rates provided an upper constraint on the long-term erosion rate experienced by the boulders. Finally, the boulder-edge roundness measurements assumed steady-state erosion and could not identify the potential for a transient state of erosion, whereas the approach of Lehmann et al. (2019a,b) inferred some transient state of erosion (Table 3). Consequently, it is notable that the lower range of the transient erosion rates derived here using the IR_{50} (6 - 460 mm/ka), $pIRIR_{150}$ (14 - 100 mm/ka) and $pIRIR_{225}$ (11 - 180 mm/ka) signals were broadly consistent with the steady-state erosion rate derived from boulder edge roundness measurements for the Torridonian sandstones (in the range of ca. 3.3 to 12.0 mm/ka). Lehmann et al. (2019b) noted that their modelled steady-state erosion rates were one to two orders of magnitude higher than suggested by a global compilation of bedrock surface erosion rates based on ^{10}Be (Portenga and Bierman, 2011), and measurements of upstanding, resistant lithic components (ca. 0.2 – 5.0 mm/ka) in crystalline rock surfaces in Arctic Norway (André, 2002). The authors inferred that shorter-term erosion rates derived from luminescence measurements were higher than the longer-term averages due to the stochastic nature of weathering impacting upon shorter-term erosion rates, this is also suggested by the data presented here. These stochastic processes (i.e. varying over time) will be controlled by the in-situ weathering rates, which provided the material for erosion. For bare rock surfaces in wet, temperate climates, weathering rates are primarily driven by rock-type and moisture availability (i.e. precipitation) (Hall et al. 2012; Swantesson, 1992). The Torridonian sandstones are hard, cemented rocks (Stewart, 1984; Stewart and Donnellson, 1992) susceptible to granular disintegration (e.g. Ballantyne and Whittington, 1987), which may have been stochastic in nature due to changing moisture availability for chemical weathering over time (Hall et al. 2012; Swantesson, 1992). Although

Torridonian sandstones are unlikely to be prone to frost shattering due to their low permeability and porosity (Lautridou, 1985; Hudec 1973 in Hall et al. 2012), cracks, faults and joints in the rock may have facilitated stochastic physical weathering (Swantesson 1992; Whalley et al. 1982), but little field evidence of this was preserved.

The modelled erosion histories that we have calculated here using the luminescence erosion-meter for samples BALL02 and BALL03 would have had a minimal effect upon the cosmogenic nuclide exposure age (4.54 ± 0.27 ka; Ballantyne and Stone, 2004). Only the steady-state erosion rate of 66 mm/ka inferred for BALL02 using the IR_{50} signal, when applied for durations exceeding 1 ka, would increase the exposure age to any great degree. For example, when the steady-state erosion rate of 66 mm/ka was applied for 0.1 ka, the corrected cosmogenic nuclide exposure age would have been 4.58 ka and, when the same erosion rate was applied for 1 ka it would have been 4.99 ka; these corrected ages were consistent within ± 2 σ uncertainties of the uncorrected age of 4.54 ± 0.27 ka (reported at 1σ: Ballantyne and Stone, 2004). The higher, transient erosion rates inferred for BALL03 were all applied for such a short period of time (e.g. Table 3) that they had a minimal effect on the cosmogenic nuclide exposure age.

Based on the long-term erosion rates derived here, the boulder sampled for BALL02 would have lost a total of 300 mm (IR_{50}), 41 mm ($pIRIR_{150}$) and 54 mm ($pIRIR_{225}$) from the surface over 4.54 ka, while the long-term erosion rates determined for BALL03 suggested that the boulder surface would have lost 27 mm (IR_{50}), 64 mm ($pIRIR_{150}$) and 50 mm ($pIRIR_{225}$). All of these values (except for the IR_{50} signal of BALL02) were broadly consistent with field observations of quartz protrusions on the surface of boulders >2 x 2 x 2 m that were densely distributed within the rock avalanche feature (Fig. 1). Alternatively, the maximum (shorter-term) erosion rate end members of the transient erosion histories would have removed 1407 mm (BALL02, $pIRIR_{225}$), 2088 mm (BALL03, IR_{50}), 454 mm (BALL03, $pIRIR_{150}$) and 817 mm (BALL03, $pIRIR_{225}$) from the boulder surface over the 4.54 ka. These large values were inconsistent with field evidence and so indicative of the transient state of erosion where high erosion rates were only sustained over short periods of time.

6.3 Late Holocene erosion history

The transient state of erosion inferred by the rock luminescence measurements reflected the stochastic nature of erosion over the last 4 ka, where a lower time-averaged erosion rate was interrupted by discrete intervals of higher time-averaged erosion rates. Rock weathering would have been dependent upon a variety of factors, primarily rock type and climate (Merrill 1906). The main constituents of the Torridonian sandstones are quartz, alkali and plagioclase feldspar (mostly albite), with precipitated quartz cementing the rock being resistant to chemical weathering (Stewart and Donnellan, 1992). However, the red colouring of the sandstones represents the presence of Fe within the rock (Stewart and Donnellsan, 1992), which is prone to chemical weathering via oxidation and reduction. Field evidence of quartz grain protrusions on the rock surfaces (Fig. 1) indicated that granular disintegration, rather than flaking or shattering, was the likely weathering process that produced material for erosion on these hard boulders (e.g. Swantesson, 1992). This is also supported by a lack of shattered material surrounding the large sampled boulders (and in fact on much of the Beinn Alligin rock avalanche deposit), despite the presence of dense,

low-level vegetation surrounding the boulders (e.g. Fig. S6). Granular disintegration has been reported as responsible for much of the general microweathering in the temperate climate of Southern and Central Sweden during the Holocene (e.g. Swantesson, 1992).

Given the coupling between precipitation, temperature and erosion (e.g. Reiners et al., 2003; Portenga and Bierman, 2011), the stochastic processes producing transient erosion can relate to varying environmental conditions (Hall et al. 2012; Swantesson, 1992; Whalley et al. 1982). In an environment where moisture is abundant due to high precipitation rates (e.g. for NW Scotland, annual precipitation rates between 1981 and 2010 were ca. 2,300 mm/a; Met Office, 2021), chemical weathering dominates; this is also reported for Holocene weathering processes in Sweden (Swantesson, 1989, 1992). Moisture availability, rather than temperature, is the limiting factor as studies have reported the presence of chemical weathering in natural settings subject to sub-zero temperatures (e.g. northern Canada, Hall, 2007; Antarctica, Balke et al. 1991). Proxy evidence from across the British Isles records variability in temperature and precipitation rates over the last 4.5 ka, where key increases in precipitation occurred at 2,750, 1,650 and 550 cal. years BP correlated to Bond cycles (Charman, 2010). Thus, the transient erosion rates measured from boulders of the Beinn Alligin avalanche were potentially a representation of the fluctuations in moisture availability experienced over the last 4.5 ka. Such processes can only be inferred from luminescence depth profiles as they are sensitive to changing erosion on shorter timeframes than all other techniques.

7. Conclusion

This study applies new rock luminescence techniques to a well-constrained test scenario provided by flat-topped boulders from the Beinn Alligin rock avalanche in NW Scotland (a wet, temperate climate), which are lithologically consistent (Torridonian sandstones), have known-age road-cuts for parameterisation of μ and $\overline{\sigma\varphi_0}$, have known cosmogenic nuclide exposure ages (4.54 ± 0.27 ka) and independently-derived Holocene erosion rates (ca. 3.3 to 12.0 mm/ka). Applying the rock luminescence techniques for exposure dating underestimated the cosmogenic nuclide ages for the Beinn Alligin rock avalanche expected due to high erosion rates (as supported by field evidence of quartz grain protrusions on the rock surfaces). Alternatively, the erosion rates determined were consistent with expected rates that were independently measured in the field from boulder-edge roundness when considering the relative timescales of the time-averaged erosion rates. The findings show that the luminescence erosion-meter has the resolution and sensitivity required to detect transient erosion of boulders over the last 4.5 ka. The transient erosion rates reflect the stochastic nature of erosional processes in the wet, temperate region of NW Scotland, likely in response to the known fluctuations in moisture availability (and to a lesser extent temperature), which control the extent of chemical weathering. This study demonstrates that the luminescence erosion-meter has huge potential for inferring erosion rates on sub-millennial scales for both steady-state and transient states of erosion (i.e. stochastic processes), which is currently impossible with other techniques. Larger sample populations and careful sampling of rock surfaces (avoiding the potential for rock pools and trickle paths) will likely be key for accurate measurements of landscape-scale erosion, and the use of a MET-pIRIR protocol (50, 150 and 225 °C) is advantageous as it can identify samples suffering from the complexities introduced by within-sample variability (e.g. surficial coatings).

Author contributions

RS, DS and RSJ were involved in project conception. RS, DS, RSJ and SB performed the field sampling. RS, DS, JB and GJ performed the measurements, analysis and interpretations. All authors contributed to the writing of the manuscript, including the preparation of figures.

Acknowledgments

Field and laboratory work was funded by Durham University Department of Geography Research Development Fund to DS. The rock luminescence equipment in the Liverpool Luminescence Laboratory was funded by a Royal Society Research Grant (RG170194) to RKS. DS is supported by a NERC Independent Research Fellowship NE/T011963/1. We thank Benjamin Lehmann, an anonymous reviewer and the Associate Editor Jim Feathers for their constructive comments which improved this manuscript.

References

Aitken, M.J. 1985. Thermoluminescence dating: Past progress and future trends. Nuclear Tracks and Radiation Measurements, 10, 3-6.

André, M.-F. 2002. Rates of postglacial rock weathering of granite roches moutonnées in northern Scandinavia (Abisko-Riksgränsen area, 68°N). Geografiska Annaler 64A, 139–150.

Balke, J., Haendel, D., Krüger, W. 1991. Contribution to the weathering-controlled removal of chemical elements from the active debris layer of the Schirmacher Oasis, East Antarctica. Zeitschrift für Geologische Wissenschaften, 19, 153–158.

Ballantyne, C.K. 1987. The Beinn Alligin 'rock glacier'. In Ballantyne, C.K. and Sutherland, D.G., editors, Wester Ross:field guide,Cambridge: Quaternary Research Association, 134-37.

Ballantyne, C.K. 2002. Paraglacial geomorphology. Quaternary Science Reviews, 21, 1935-2017.

Ballantyne, C.K. 2003. A Scottish sturzstrom: The Beinn Alligin rock avalanche, Wester Ross. Scottish Geographical Journal, 119, 159-167.

Ballantyne, C.K., Whittington, G. 1987. Niveo-aeolian sand deposits on An Teallach, Wester Ross, Scotland. Earth and Environmental Science Transactions of The Royal Society of Edinburgh, 78, 51 – 63.

Ballantyne, C.K., Stone, J.O. 2004. The Beinn Alligin rock avalanche, NW Scotland: cosmogenic ^{10}Be dating, interpretation and significance. The Holocene, 14, 448-453.

Bennett, M.R., Boulton, G.S. 1993. Deglaciation of the Younger Dryas or Loch Lomond Stadial ice-field in the northern Highlands, Scotland. Journal Quaternary Science, 8, 133–145.

Bowen, D.Q. 1992. The Pleistocene of North West Europe. Science Progress, 76, 209-223.

Brill, D., May, S.M., Mhammdi, N., King, G., Lehmann, B., Burow, C., Wolf, D., Zander, A., Brückner, H. 2021. Evaluating optically stimulated luminescence rock surface exposure dating as a novel approach for reconstructing coastal boulder movement on decadal to centennial timescales. Earth Surface Dynamics, 9, 205-234.

Brown, N.D. 2020. Which geomorphic processes can be informed by luminescence measurements. Geomorphology, 367, 107296.

Brown, N.D., Moon, S. 2019. Revisiting erosion rate estimates from luminescence profiles in exposed bedrock surfaces using stochastic erosion simulations. Earth and Planetary Science Letters, 528, 115842.

Chapot, M.S., Sohbati, R., Murray, A.S., Pederson, J.L., Rittenour, T.M. 2012. Constraining the age of rock art by dating a rockfall event using sediment and rock-surface luminescence dating techniques. Quaternary Geochronology, 13, 18-25.

Charman, D. 2010. Centennial climate variability in the British Isles during the mid–late Holocene. Quaternary Science Reviews, 29, 1539-1554.

Esri. "World Imagery" [basemap]. Scale Not Given. "World Imagery". December 12, 2009. https://services.arcgisonline.com/ArcGIS/rest/services/World_Imagery/MapServer. (Feb, 11, 2021).
Esri. "Topographic" [basemap]. Scale Not Given. "World Topographic Map". June 14, 2013. http://www.arcgis.com/home/item.html?id=30e5fe3149c34df1ba922e6f5bbf808f. (Feb, 11, 2021).
Ford, D., Williams, P. 1989. Karst Geomorphology and Hydrology. Unwin Hyman, London. 601 pp.
Freiesleben, T., Sohbati, R. Murray, A., Jain, M., al Khasawneh, S., Hvidt, S., Jakobsen, B. 2015. Mathematical model quantifies multiple daylight exposure and burial events for rock surfaces using luminescence dating. Radiation Measurements, 81, 16-22.
Gliganic, L.A., Meyer, M.C., Sohbati, R., Jain, M., Barrett, S. 2019. OSL surface exposure dating of a lithic quarry in Tibet: Laboratory validation and application. Quaternary Geochronology, 49, 199-204.
Golledge, N.R., Hubbard, A., Sugden, D.E. 2008. High-resolution numerical simulation of Younger Dryas glaciation in Scotland. Quaternary Science Reviews, 27, 888-904.
Gordon, J.E. 1993. Beinn Alligin. In Gordon, J.E. and Sutherland, D.G., editors Quaternary of Scotland, London: Chapman and Hall, 118-22.
Habermann, J., Schilles, T., Kalchgruber, R., Wagner, G.A., 2000. Steps towards surface dating using luminescence. Radiation Measurements 32, 847-851.
Hall, K. 2007. Evidence for freeze-thaw events and their implications for rock weathering in northern Canada, II: the temperature at which water freezes in rock. Earth Surface Processes and Landforms, 32, 249–259.
Hall, K., Arocena, J.M., Boelhouwers, J., Zhu, L. 2005. The influence of aspect on the biological weathering of granites: observations from the Kunlun Mountains, China. Geomorphology, 67, 171–188.
Hall, K., Guglielmin, M., Strini, A. 2008. Weathering of granite in Antarctica II: thermal data at t the grain scale. Earth Surface Processes and Landforms, 33, 475–493.
Hall, K., Thorn, C., Sumner, P. 2012. On the persistence of 'weathering'. Geomorphology, 149-150, 1-10.
Hanna, F.K. 1966. A technique for measuring the rate of erosion of cave passages. Proceedings University of Bristol Spelaeology Society, 11, 83–86.
Herman, F., Rhodes, E.J., Braun, J., Heiniger, L. 2010. Uniform erosion rates and relief amplitude during glacial cycles in the Southern Alps of New Zealand, as revealed from OSL-thermochronology. Earth and Planetary Science Letters, 297, 183-189.
High, C.J., Hanna, F.K. 1970. A method for the direct measurement of erosion on rock surfaces. British Geomorphological Research Group Technical Bulletin, 5, 1–25.
Hijmans, R.J. (2019). raster: Geographic Data Analysis and Modeling. R package version 2.9-23. https://CRAN.R-project.org/package=raster
Huntley, D.J., Lamothe, M. 2001. Ubiquity of anomalous fading in K-feldspars and the measurement and correction for it in optical dating, 38, 1093-1106.
Israelli, Y., Emmanuel, S. 2018. Impact of grain size and rock composition on simulated rock weathering. Earth Suface Dynamics, 6, 319-327.
Jenkins, G. T. H., Duller, G. A. T., Roberts, H. M., Chiverrell, R. C., Glasser, N. F. 2018. A new approach for luminescence dating glaciofluvial deposits – High precision optical dating of cobbles. Quaternary Science Reviews, 192, 263 – 273.
Kirkbride, M.P., Bell, C.M. 2010. Edge-roundness of boulders of Torridonian Sandstone (northwest Scotland): applications for relative dating and implications for warm and cold climate weathering rates. Boreas DOI 10.1111/j.1502-3885.2009.00131.
Kolb, T., Fuchs, M. 2018. Luminescence dating of pre-Eemian (pre-MIS 5e) fluvial terraces in Northern Bavaria (Germany) – Benefits and limitations of applying a pIRIR225-approach. Geomorphology, 321, 16-32.
Laskaris, N., Liritzis, I. 2011. A new mathematical approximation of sunlight penetrations in rocks for surface luminescence dating. Journal of Luminescence, 131, 1874-1884.
Lehmann, B., Valla, P.G., King, G.E., Herman, F. 2018. Investigation of OSL surface exposure dating to reconstruct post-LIA glacier fluctuations in the French Alps (Mer de Glace, Mont Blanc massif). Quaternary Geochronology, 44, 63-74.
Lehmann, B., Herman, F., Valla, P.G., King, G.E., Biswas, R.H. 2019a. Evaluating post-glacial bedrock erosion and surface exposure duration by coupling in situ optically stimulated luminescence and 10Be dating. Earth Surface Dynamics, 7, 633-662.

Lehmann, B., Herman, F., Valla, P.G., King, G.E., Biswas, R.H., Ivy-Ochs, S., Steinemann, O., Christl, M. 2019b. Postglacial erosion of bedrock surfaces and deglaciation timing: New insights from the Mont Blanc massif (western Alps). Geology, https://doi.org/10.1130/G46585.1

Li, B., Li, S-H. 2011. Luminescence dating of K-feldspar from sediments: A protocol without anomalous fading correction. Quaternary Geochronology. 6, 468-479.

Liu, J., Murray, A., Sohbati, R., Jain, M. 2016. The effect of test dose and first IR Stimulation temperature on post-IR IRSL measurements of rock slices. Geochronometria, 43, 179-187.

Luo, M., Chen, J., Liu, J., Qin, J., Owen, L., Han, F., Yang, H. Wang, H., Zhang, B., Yin, J., Li, Y. 2018. A test of rock surface luminescence dating using glaciofluvial boulders from the Chinese Pamir. Radiation Measurements, 120, 290-297.

Merrill, G.P. 1906. A Treatise on Rocks. Rock-Weathering and Soils, Macmillan, New York. 400 pp.

Met Office, 2021. UK Climate averages (1981-2010): Kinlochewe Met station (57.613°N, -5.308°W) https://www.metoffice.gov.uk/research/climate/maps-and-data/uk-climate-averages/gfhpz0nu4 [Accessed 18/01/2021].

Meyer, M.C., Gliganic, L.A., Jain, M., Schmidmair, D. 2018. Lithological controls on light penetration into rock surfaces – Implications for OSL and IRSL surface exposure dating. Radiation Measurements, 120, 298-304.

Ou, X.J., Roberts, H.M., Duller, G.A.T., Gunn, M.D., Perkins, W.T. 2018. Attenuation of light in different rock types and implications for rock surface luminescence dating. Radiation Measurements, 120, 305-311.

Parish, R. 1994. The influence of feldspar weathering on luminescence signals and the implications for luminescence dating of sediments. In Robinson, D.A. and Williams, R.B.G., editors, Rock weathering and landform evolution, Chichester: Wiley.

Pederson, J.L., Chapot, M.S., Simms, S.R., Sohbati, R., Rittenour, T.M., Murray, A.S., Cox, G. 2014. Age of Barrier Canyon-style rock art constrained by cross-cutting relations and luminescence dating techniques. PNAS 111, 12986-12991.

Polikreti, K., Michael, C.T., Maniatis, Y., 2002. Authenticating marble sculpture with thermoluminescence. Ancient TL 20, 11-18.

Polikreti, K. Michael, C.T. and Maniatis, Y. 2003. Thermoluminescence characteristics of marble and dating of freshly excavated marble objects. Radiation Measurements, 37, 87–94.

Portenga, E.W., Bierman, P.R. 2011. Understanding Earth's eroding surface with ^{10}Be. GSA Today, 21, 4-10.

Prescott, J.R., Hutton, J.T. 1994. Cosmic ray and gamma ray dosimetry for TL and ESR. Nuclear Tracks and Radiation Measurements, 14, 223-227.

Reiners, P.W., Brandon, M.T. 2006. Using thermochronology to understand orogenic erosion. Annual Review of Earth Planetary Science,doi: 10.1146/ annurev.earth.34.031405.125202.

Riebe CS, Kirchner JW, Finkel RC. 2003. Long-term rates of weathering and physical erosion from cosmogenic nuclides and geochemical mass balance. Geochim. Cosmochim. Acta, 67, 4411–27

Roberts, H.M. 2012. Testing Post-IR IRSL protocols for minimising fading in feldspars, using Alaskan loess with independent chronological control. Radiation Measurements, 47, 716-724.

Robinson, D.A., Williams, R.B.G. 1987. Surface crusting of sandstones in southern England and northern France. In: Gardner, V. (Ed.), International Geomorphology 1986, vol. 2. Wiley, Chichester, pp. 623–635.

Singhvi, A.K., Deraniyagala, S.U., Sengupta, D. 1986. Thermoluminescence dating of Quaternary red-sand beds: a case study of coastal dunes in Sri Lanka. Earth and Planetary Science Letters, 80, 139-144.

Sissons, J.B. 1975. A fossil rock glacier in Wester Ross. Scottish Journal of Geology, 11, 83-86.

Sissons, J.B. 1976. A fossil rock glacier in Wester Ross. Reply to W.B. Whalley. Scottish Journal of Geology, 12, 178-79.

Smedley, R.K., Duller, G.A.T., Roberts, H.M. 2015. Assessing the bleaching potential of the post-IR IRSL signal for individual K-feldspar grains: implications for single-grain dating. Radiation Measurements, 79, 33 – 42.

Smedley, R.K., Glasser, N.F., Duller, G.A.T. 2016. Luminescence dating of glacial advances at Lago Buenos Aires (~46 °S), Patagonia. Quaternary Science Reviews, 134, 59 – 73.

Sohbati, R., Murray, A.S., Jain, M., Buylaert, J.P., Thomsen, K.J. 2011. Investigating the resetting of OSL signals in rock surfaces. Geochronometria, 38, 249–258.

Sohbati, R., Murray, A.S., Buylaert, J.P., Almeida, N.A.C., Cunha, P.P. 2012a. Optically stimulated luminescence (OSL) dating of quartzite cobbles from the Tapada do Montinho archaeological site (east-central Portugal). Boreas, 41, 452–462.

Sohbati, R., Murray, A.S., Chapot, M.S., Jain, M., Pederson, J., 2012b. Optically stimulated luminescence (OSL) as a chronometer for surface exposure dating. Journal of Geophysical Research Solid Earth, 117.

Sohbati, R., Liu, J., Jain, M., Murray, A.S., Egholm, D., Pairs, R., Guralnick, B. 2018. Centennial- to millennial-scale hard rock erosion rates deduced from luminescence-depth profiles. Earth and Planetary Science Letter, 493, 218-230.

Stewart, A.D. 1982. Late Proterozoic rifting in NW Scotland: the genesis of the 'Torridonian'. Journal of Geological Society of London, 139, 413-420.

Stewart, A.D. Donnellson, N.C.B. 1992. Geochemistry and provenance of red sandstones in the Upper Proterozoic Torridon Group in Scotland. Scottish Journal of Geology, 28, 143-153.

Stocker, T.F., D. Qin, G.-K. Plattner, L.V. Alexander, S.K. Allen, N.L. Bindoff, F.-M. Bréon, J.A. Church, U. Cubasch, S. Emori, P. Forster, P. Friedlingstein, N. Gillett, J.M. Gregory, D.L. Hartmann, E. Jansen, B. Kirtman, R. Knutti, K. Krishna Kumar, P. Lemke, J. Marotzke, V. Masson-Delmotte, G.A. Meehl, I.I. Mokhov, S. Piao, V. Ramaswamy, D. Randall, M. Rhein, M. Rojas, C. Sabine, D. Shindell, L.D. Talley, D.G. Vaughan and S.-P. Xie, 2013: Technical Summary. In: Climate Change 2013: The Physical Science Basis. Contribution of Working Group I to the Fifth Assessment Report of the Intergovernmental Panel on Climate Change [Stocker, T.F., D. Qin, G.-K. Plattner, M. Tignor, S.K. Allen, J. Boschung, A. Nauels, Y. Xia, V. Bex and P.M. Midgley (eds.)]. Cambridge University Press, Cambridge, United Kingdom and New York, NY, USA.

Swantesson, J.O.H. 1989.Weathering phenomena in a cool temperate climate. Göteborgs University, Naturgeogr. Inst., Guni. Rapport, 28.

Swantesson, J.O.H. 1992. Recent microweathering phenomena in Southern and Central Sweden. Permafrost and Periglacial Processes, 3, 275-292.

Swantesson, J.O.H., Moses, C.A., Berg, G.E., Jansson, K.M. 2006. Methods for measuring shore platform micro-erosion: a comparison of the micro-erosion meter and laser scanner. Z. Geomorpholology, 144, 1–17.

Thomsen, K. J., Murray, A. S., Jain, M. and Bøtter-Jensen, L. 2008. Laboratory fading rates of various luminescence signals from feldspar-rich sediment extracts. Radiation Measurements, 43, 1474 –1486.

Thomsen, K.J., Murray, A.S., Jain, M. 2011. Stability of IRSL signals from sedimentary K-feldspar samples. Geochronometria, 38, 1-13.

Thomsen, K.J., Kook, M., Murray, A.S., Jain, M. 2018. Resolving luminescence in spatial and compositional domains. Radiation Measurements, 15, 260-266.

Thorn, C.E., Darmody, R.G., Dixon, J.C., Schlyter, P. 2001. The chemical weathering regime of Kärkevagge, arctic-alpine Sweden. Geomorphology, 41, 37–52.

Trauerstein, M., Lowick, S.E., Preusser, F., Schlunegger, F. 2014. Small aliquot and single grain IRSL and post-IR IRSL dating of fluvial and alluvial sediments from the Pativilca valley, Peru. Quaternary Geochronology, 22, 163-174.

Trudgill, S.T., Viles, H., Inkpen, R.J., Cooke, R.U. 1989. Remeasurement of weathering rates, St. Paul's Cathedral, London. Earth Surface Processes and Landforms, 14, 175–196.

Twidale, C.R., 1982. Granite Landforms. Elsevier, Amsterdam. 372 pp.

Vafiadou, A., Murray, A.S., Liritzis, I., 2007. Optically stimulated luminescence (OSL) dating investigations of rock and underlying soil from three case studies. Journal of Archaeological Science 34, 1659-1669.

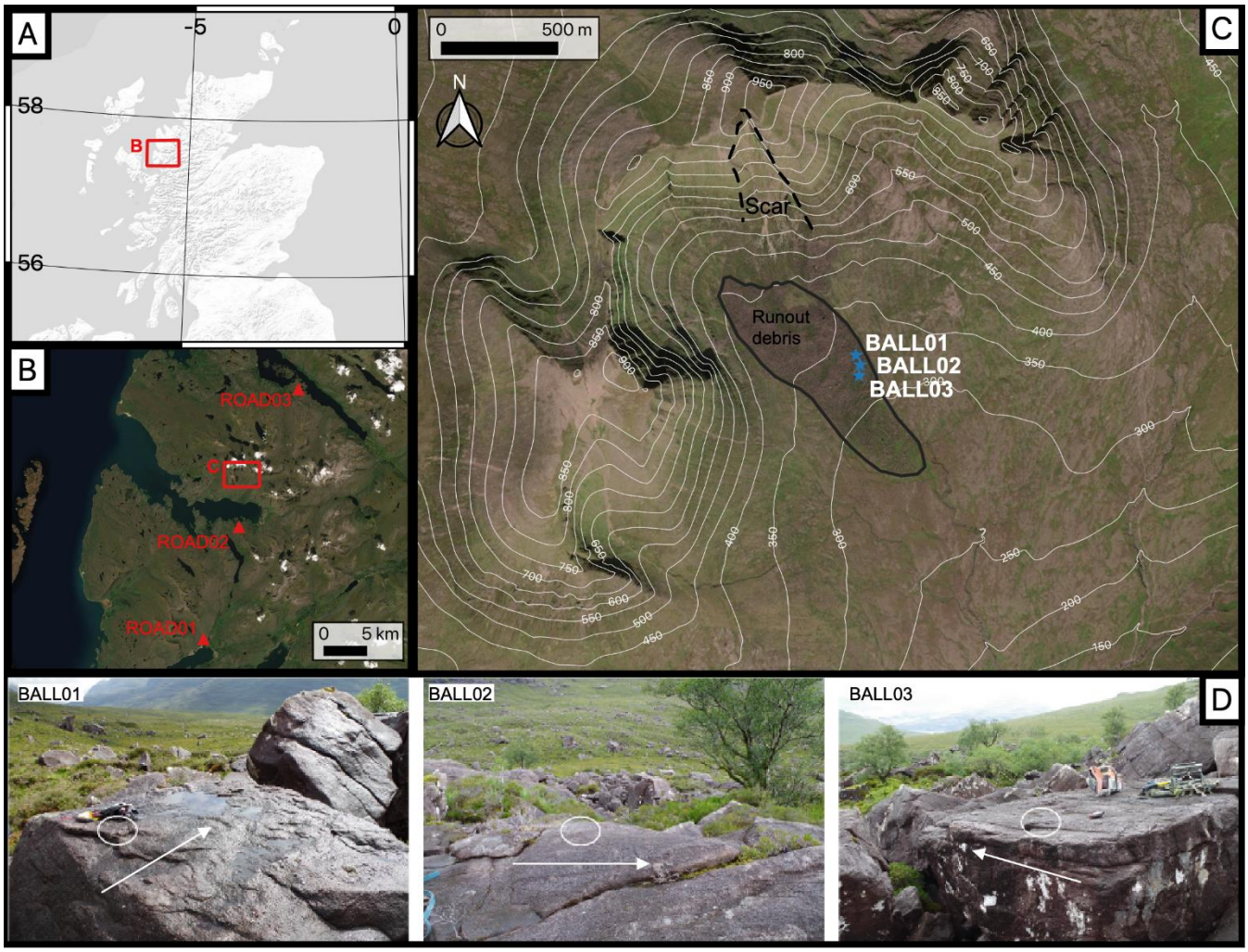

Figure 1. Location of the Beinn Alligin rock avalanche (57°35'N, 05°34'W) and roadcut sections in NW Scotland (A,B). Sample sites on the rock avalanche deposit (C). Photographs of flat-topped boulders sampled and the general rock avalanche flow direction (white arrow) for BALL01, BALL02 and BALL03 (D). The backgrounds used are ESRI World Terrain Base (A) and ESRI World Imagery (B,C). Contains OS data © Crown copyright and database right (2021). Scar and runout debris locations mapped in (C) follow Ballantyne and Stone (2004).

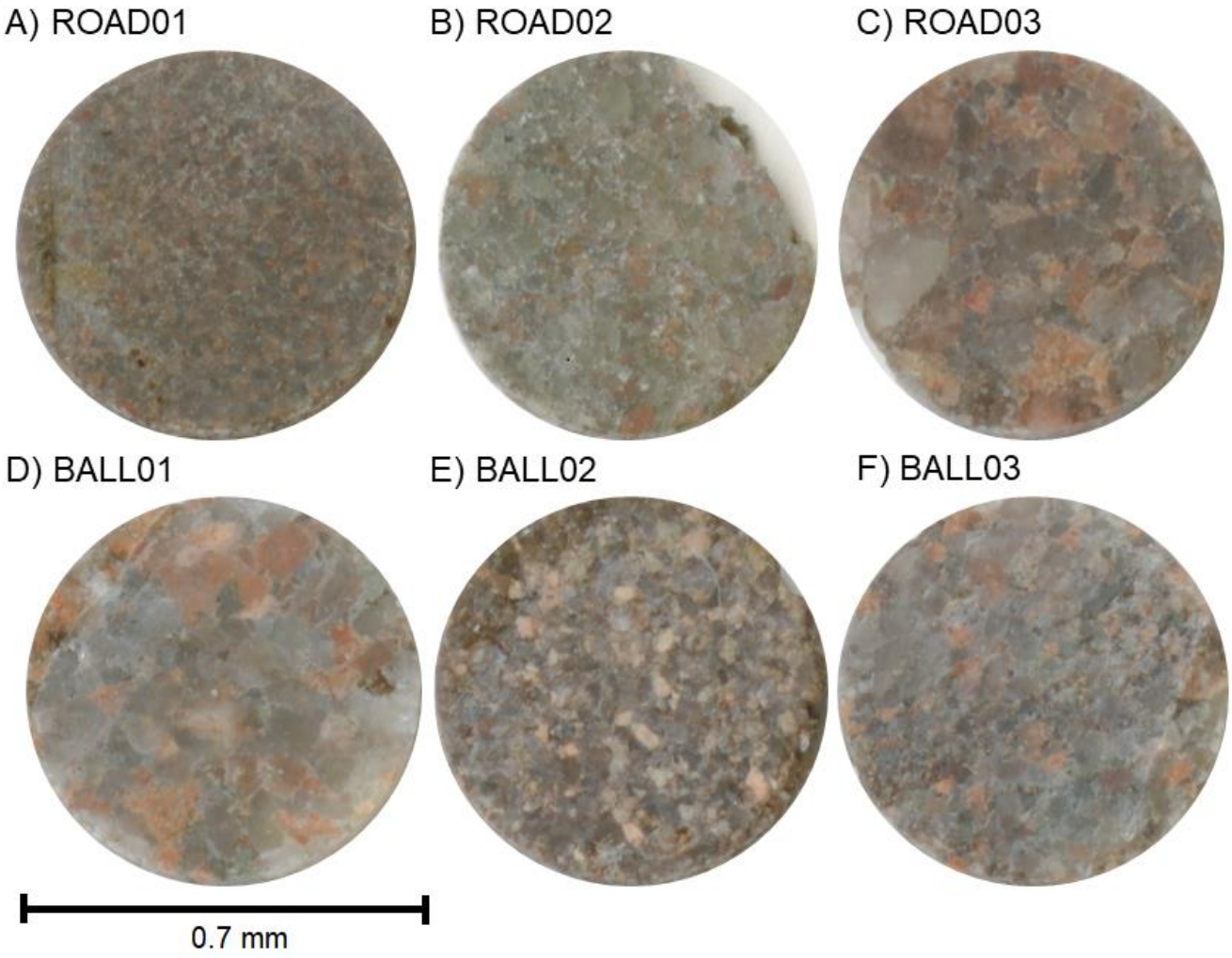

Figure 2. Images of example rock slices (0.7 mm diameter) for each sample taken using the EPSON Expression 11000XL flatbed scanner.

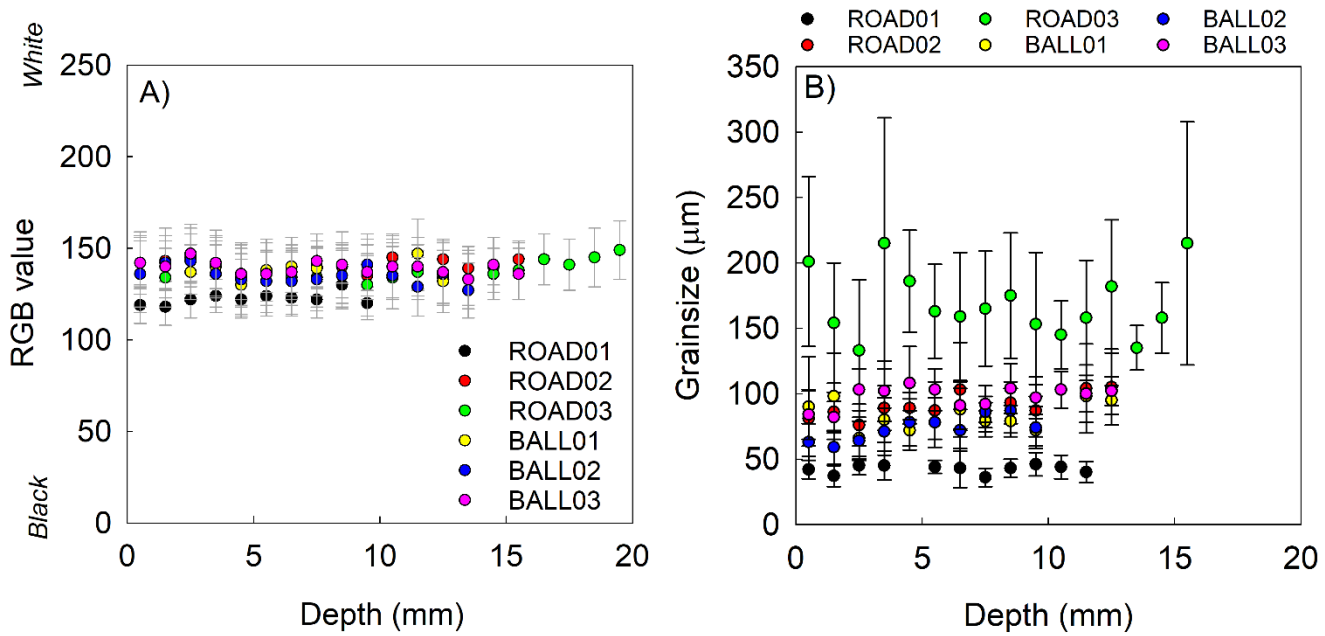

Figure 3. (A) RGB values (0 = black and 255 = white) and (B) grainsize for each sample, calculated as the mean (± standard deviation) of the slices at each depth in all of the replicate cores analysed. Note that the RGB values and grainsize measurements were not derived from exactly the same cores, but example cores for each sample.

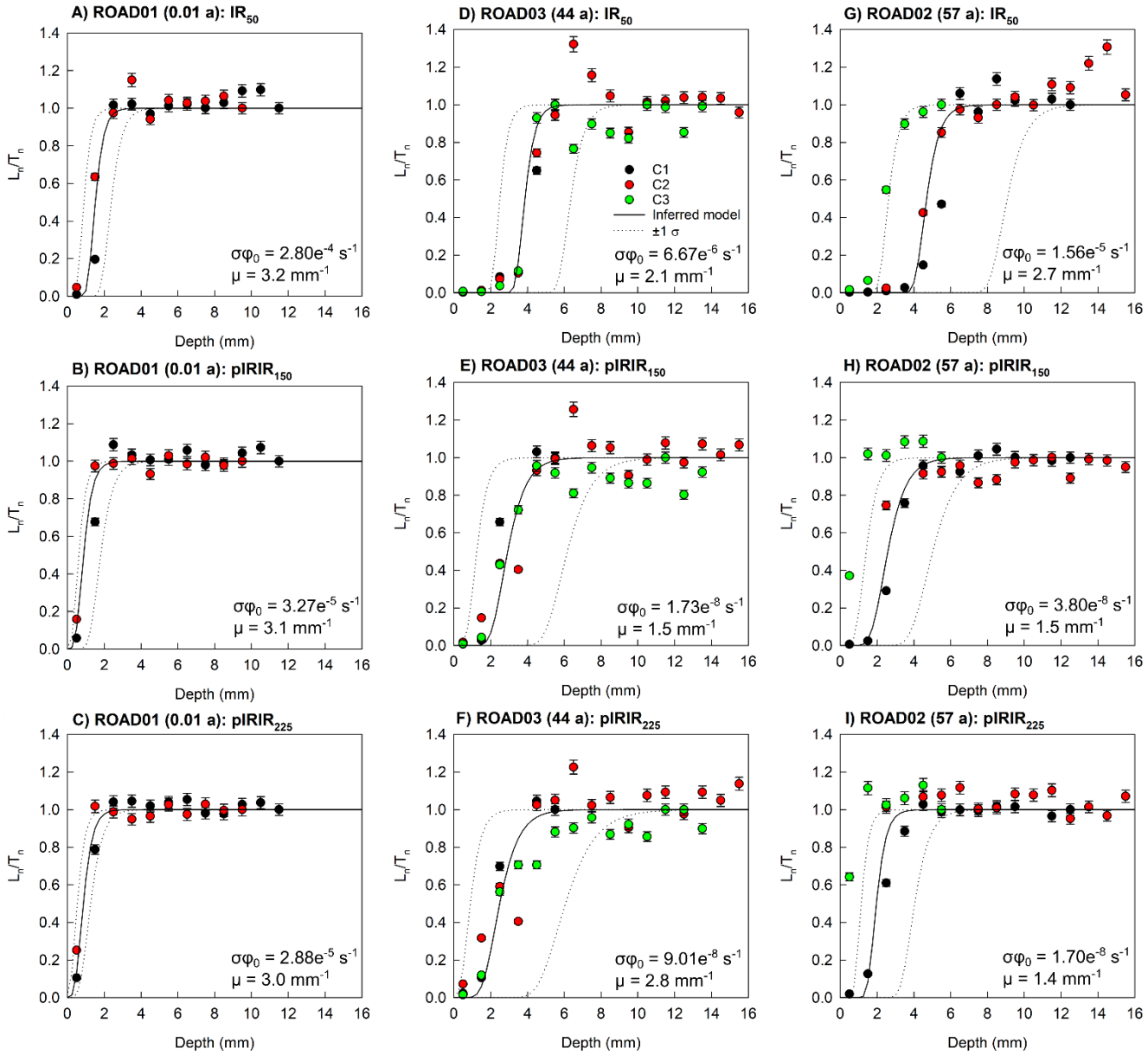

Figure 4. Presented in age-order are the IRSL-depth profiles for each of the three replicate cores analysed per sample using the IR_{50} (A,D,G), $pIRIR_{150}$ (B,E,H) and $pIRIR_{225}$ (C,F,I) signals for samples ROAD01 (0.01 a; A-C), ROAD03 (44 a; D-F) and ROAD02 (57 a; G-I). All of the raw L_n/T_n data presented in this figure (Table S2-S4) were normalised individually for each core, and subsequent analysis uses the data in this format. The black line shown is the inferred model that was fitted to derive the corresponding $\overline{\sigma\varphi_0}$ and μ values included in each figure. The dotted lines show the corresponding fits modelled using the ± 1 σ $\overline{\sigma\varphi_0}$ and μ values (Table 2). Note that core 3 of ROAD02 was not considered for fitting.

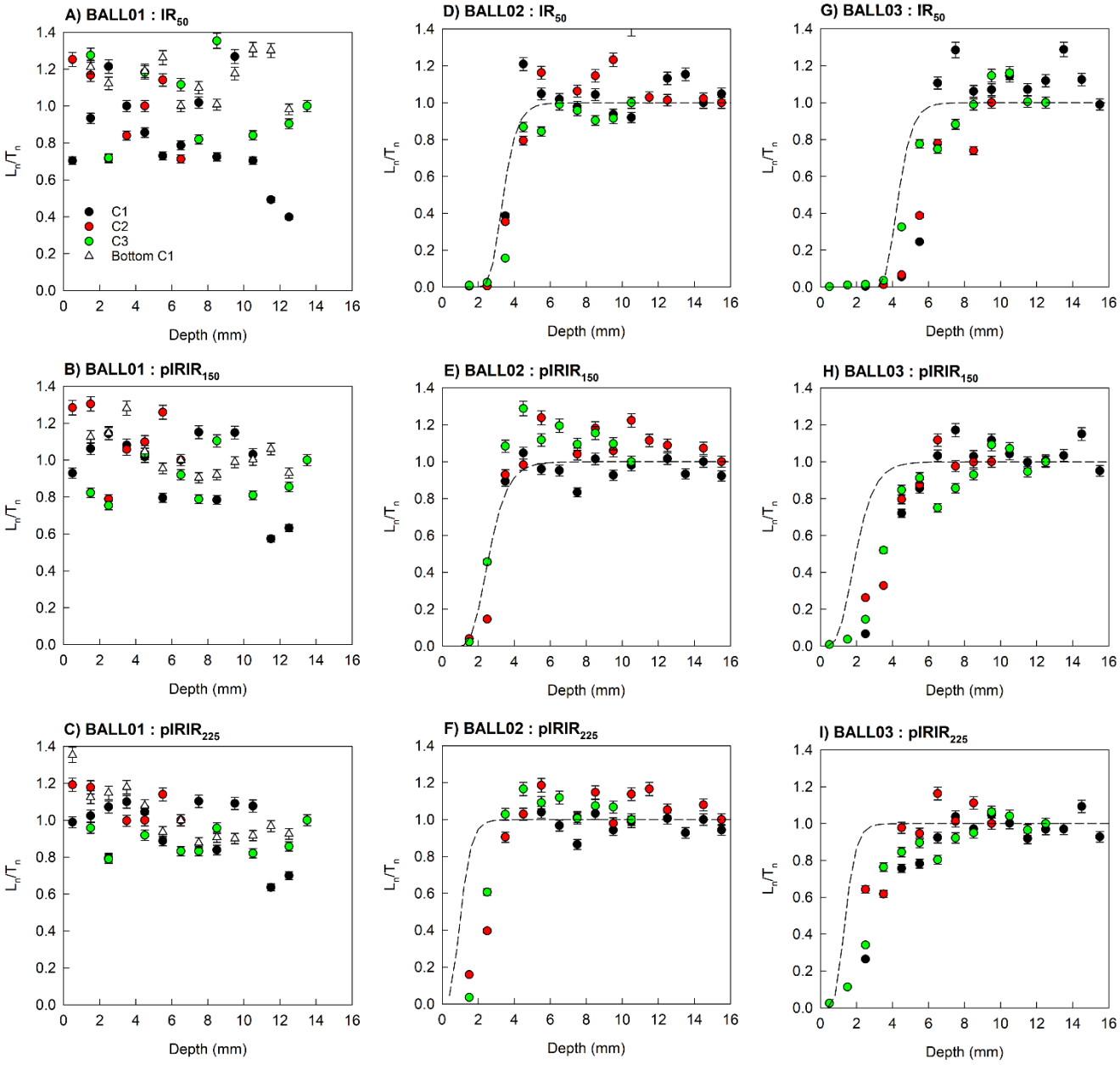

Figure 5. IRSL-depth profiles for each replicate cores analysed using the IR_{50} (A,D,G), $pIRIR_{150}$ (B,E,H) and $pIRIR_{225}$ (C,F,I) signals for samples BALL01 (A-C), BALL02 (D-F) and BALL03 (G-I). All of the raw L_n/T_n data (Table S5-S7) were normalised individually for each core, and subsequent analysis uses the data in this format. The dashed line is the inferred erosion model for each luminescence depth profile derived from the probability distributions shown in Fig. 7, where erosion rates are included in Table 3.

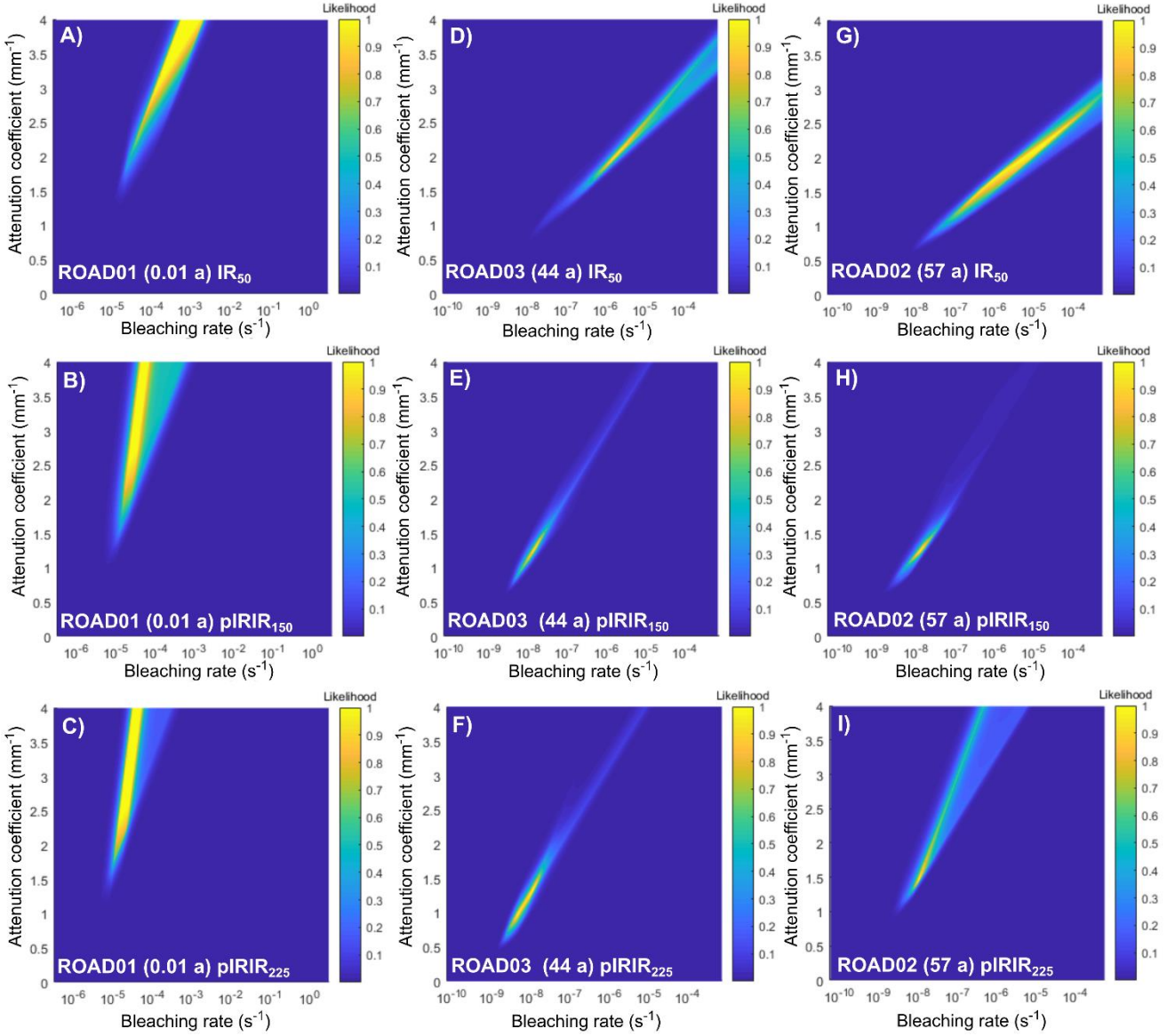

Figure 6. Presented in age-order is the relationship between $\overline{\sigma\varphi_0}$ and μ parameters for ROAD01 (A-C), ROAD03 (D-F) and ROAD02 (G-I) using the IR_{50} (A,D,G), $pIRIR_{150}$ (B,E,H) and $pIRIR_{225}$ (C,F,I) signals using the approach of Lehmann et al. (2018).

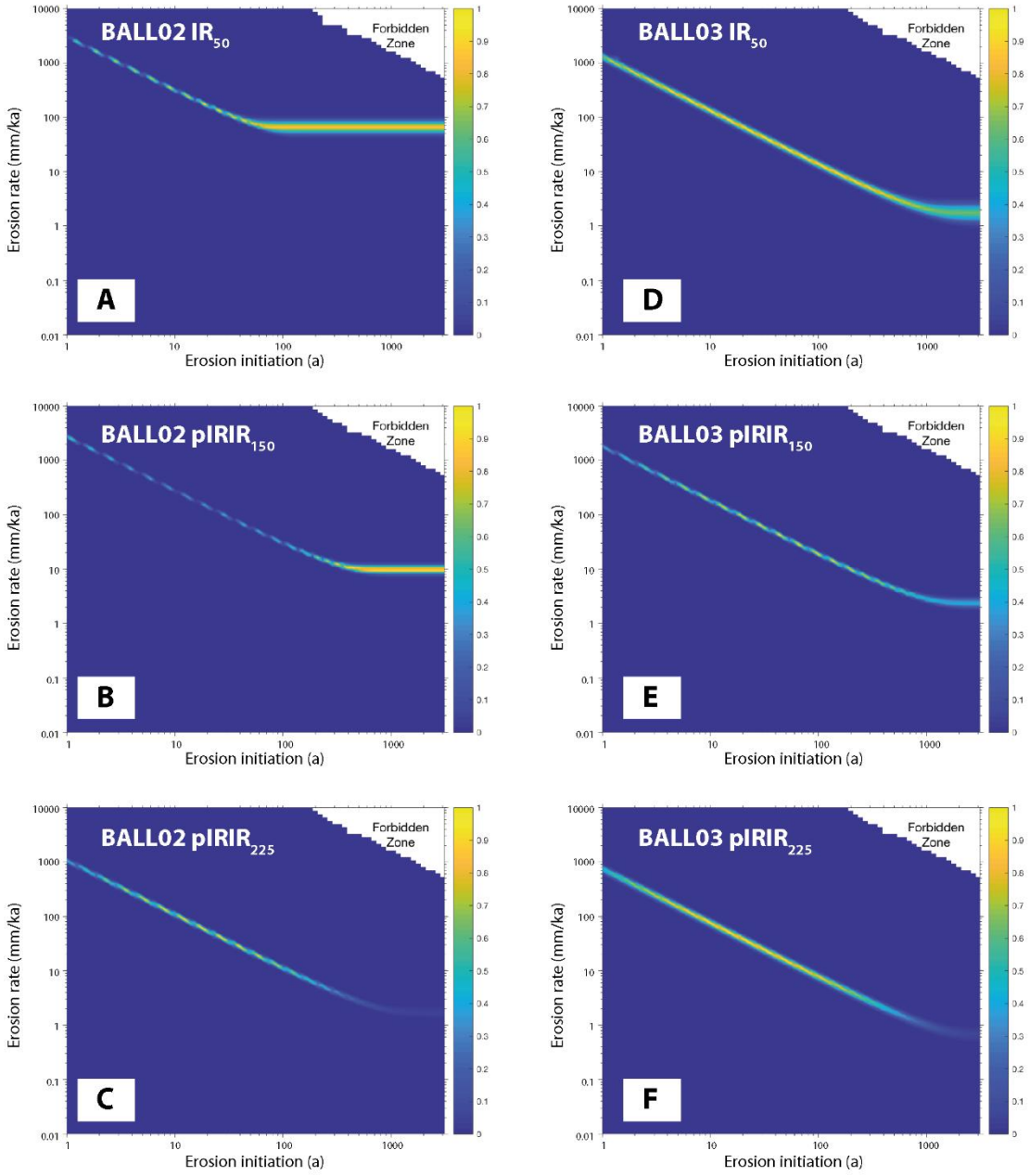

Figure 7. Probability distributions inverted from the respective plots of luminescence depth profiles derived from the inversion results (using the approach of Lehmann et al. 2019a) for samples BALL02 (A-C) and BALL03 (D-F) using the IR_{50}, (A,D), $pIRIR_{150}$ (B,E) and $pIRIR_{225}$ (C,F) signals. Forbidden zones define the range of solutions with high erosion rates and durations that are not feasible within the bounds of the experimental ^{10}Be and luminescence data.

Table 1. Luminescence results for the rock slices analysed in this study. Environmental dose-rates were determined using high-resolution gamma spectrometry. The dose-rates were calculated using the conversion factors of Guerin et al. (2011) and alpha (Bell, 1980) and beta (Guerin et al. 2012) dose-rate attenuation factors. An internal K-content of 10 ± 2 % (Smedley et al. 2012) and internal U and Th concentrations of 0.3 ± 0.1 ppm and 1.7 ± 0.4 ppm (Smedley and Pearce, 2016) were used to determine the internal alpha and beta dose-rates. An a-value of 0.10 ± 0.02 (Balescu and Lamothe, 1993) was used to calculate the alpha dose-rates. Cosmic dose-rates were determined after Prescott and Hutton (1994). Dose-rates were calculated using the Dose Rate and Age Calculator (DRAC; Durcan et al. 2015). Grain size was measured by randomly selecting grains in the rock slices for each sample and calculating ±1 standard deviation around the mean grain size.

Sample	Grain size (μm)	U (ppm)	Th (ppm)	K (%)	Internal alpha dose-rate (Gy/ka)	Internal beta dose-rate (Gy/ka)	External alpha dose-rate (Gy/ka)	External beta dose-rate (Gy/ka)	External gamma dose-rate (Gy/ka)	External cosmic dose-rate (Gy/ka)	Total dose-rate (Gy/ka)
BALL02	56-91	1.02±0.15	4.85±0.28	1.73±0.29	0.14±0.04	0.27±0.06	0.21±0.05	1.62±0.00	0.78±0.08	0.31±0.03	3.32±0.12
BALL03	79-117	1.02±0.14	5.21±0.28	1.86±0.29	0.16±0.04	0.35±0.08	0.17±0.04	1.71±0.00	0.83±0.08	0.31±0.03	3.52±0.12
ROAD01	33-51	2.07±0.27	7.80±0.42	2.45±0.43	0.10±0.03	0.16±0.03	0.61±0.12	2.43±0.00	1.22±0.11	0.30±0.03	4.81±0.18
ROAD02	67-113	1.55±0.18	5.67±0.38	2.88±0.40	0.15±0.04	0.32±0.08	0.23±0.05	2.59±0.00	1.16±0.10	0.30±0.03	4.76±0.15
ROAD03	112-225	1.93±0.21	5.30±0.30	1.96±0.31	0.18±0.04	0.58±0.20	0.14±0.04	1.85±0.00	0.96±0.08	0.29±0.03	4.00±0.22

Table 2. Calibration factors determined by fitting depth profiles. Note that values presented are medians.

Sample	IRSL signal	$\overline{\sigma\varphi_0}$ (s^{-1})	Range ±1 σ (s^{-1})	μ (mm^{-1})	Range ±1 σ (mm^{-1})
ROAD01	IR_{50}	$2.80e^{-4}$	$8.41e^{-4} – 6.43e^{-5}$	3.2	2.5 – 3.8
	$pIRIR_{150}$	$3.27e^{-5}$	$1.16e^{-4} – 2.14e^{-5}$	3.1	2.2 – 3.7
	$pIRIR_{225}$	$2.88e^{-5}$	$3.99e^{-5} – 1.51e^{-5}$	3.0	2.3 – 3.6
ROAD02	IR_{50}	$6.67e^{-6}$	$1.27e^{-4} – 3.50e^{-7}$	2.1	1.4 – 2.6
	$pIRIR_{150}$	$1.73e^{-8}$	$9.64e^{-8} – 9.75e^{-9}$	1.5	1.1 – 2.3
	$pIRIR_{225}$	$9.01e^{-8}$	$5.53e^{-7} – 2.31e^{-8}$	2.8	1.8 – 3.6
ROAD03	IR_{50}	$1.56e^{-5}$	$1.64e^{-4} – 1.48e^{-6}$	2.7	2.0 – 3.2
	$pIRIR_{150}$	$3.80e^{-8}$	$4.40e^{-7} – 1.12e^{-8}$	1.5	1.1 – 2.5
	$pIRIR_{225}$	$1.70e^{-8}$	$1.17e^{-7} – 4.70e^{-9}$	1.4	0.9 – 2.5

Table 3. Luminescence exposure ages and erosion rates determined using the approach of Lehmann et al. (2018) and Lehmann et al. (2019a), respectively. The values of $\overline{\sigma\varphi_0}$ and μ were determined from known-age sample ROAD02 (57 a).

Sample	Signal	$\overline{\sigma\varphi_0}$ (s^{-1})	μ (mm^{-1})	$\dot{D}$ (Gy/ka)	D_0 (Gy)	Exposure age (a)	Steady-state erosion rate (mm/ka)	Min. initiation time (a)	Max. transient erosion rate (mm/ka)	Initiation time (a)	Min. transient erosion rate (mm/ka)	Initiation time (a)
BALL02	IR_{50}	$6.67e^{-6}$	2.1	3.32 ± 0.12	500	8 ± 2	66	73	-	-	-	-
	$pIRIR_{150}$	$1.73e^{-8}$	1.5	3.32 ± 0.12	350	66 ± 16	9	593	-	-	-	-
	$pIRIR_{225}$	$9.01e^{-8}$	2.8	3.32 ± 0.12	350	263 ± 30	-	-	310	4	12	90
BALL03	IR_{50}	$6.67e^{-6}$	2.1	3.52 ± 0.12	500	387 ± 103	-	-	460	3	6	231
	$pIRIR_{150}$	$1.73e^{-8}$	1.5	3.52 ± 0.12	350	296 ± 54	-	-	100	19	14	137
	$pIRIR_{225}$	$9.01e^{-8}$	2.8	3.52 ± 0.12	350	362 ± 49	-	-	180	4	11	73

Supplementary material: Smedley et al.

Erosion rates in a wet, temperate climate derived from rock luminescence techniques

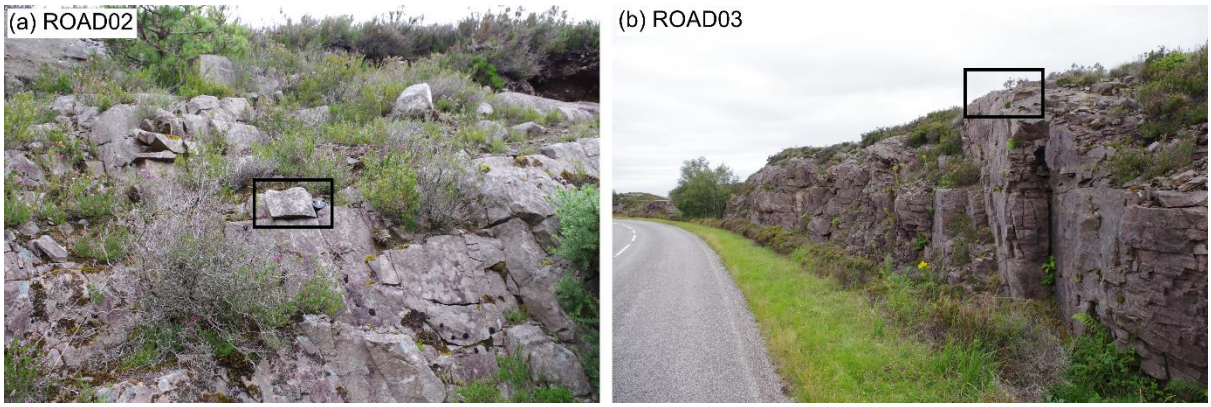

Fig. S1. Photographs of the known-age roadcut sections sampled for ROAD02 (a) and ROAD03 (b) constrained to 57 a and 44 a, respectively.

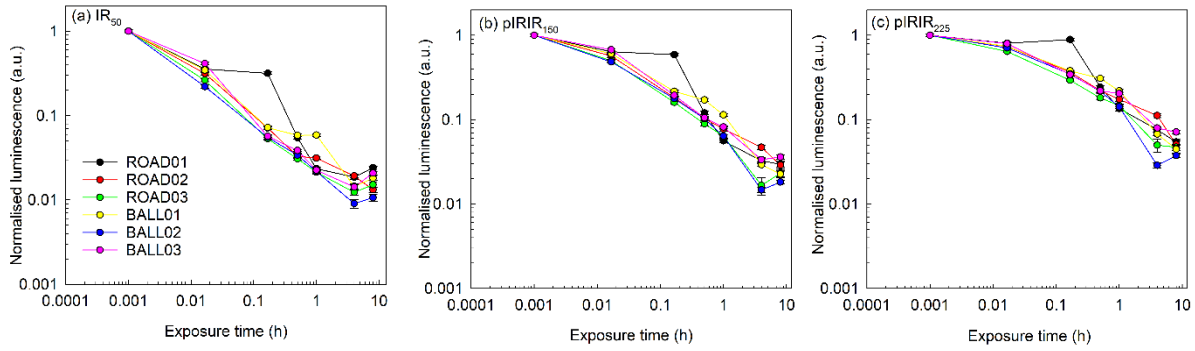

Fig. S2. Normalised luminescence signal remaining for individual discs from each sample after a given dose of 105 Gy and subsequent exposure to the solar simulator (0 m, 1 m, 10 m, 30 m, 1 h, 4 h and 8 h). Note that each disc had already been analysed for the natural luminescence signal.

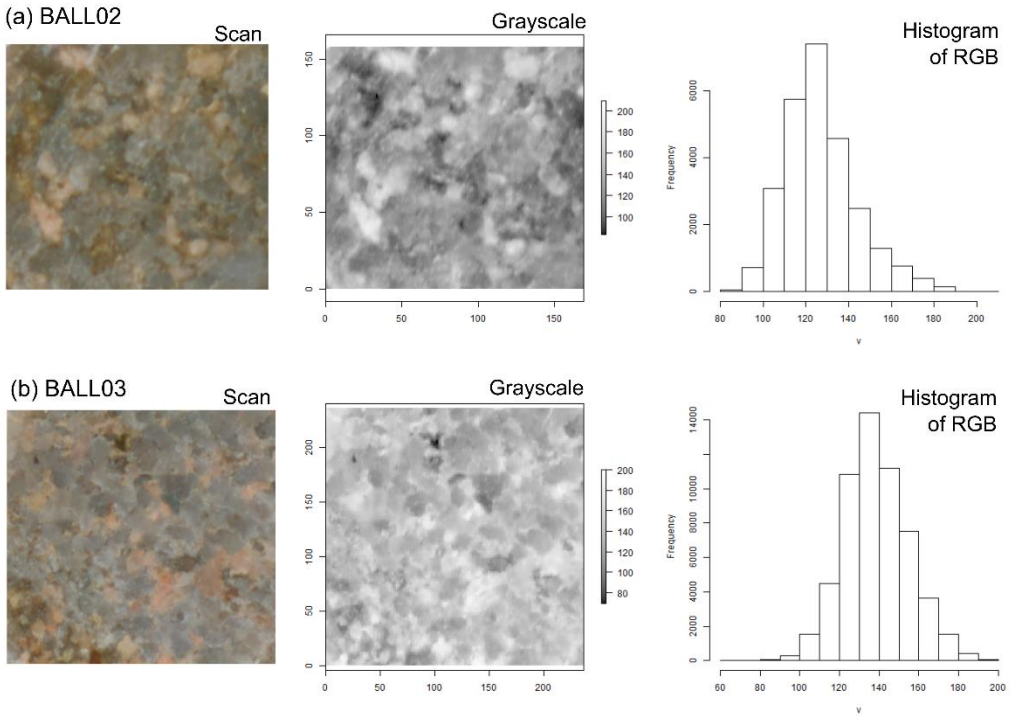

Fig. S3. Examples of true-colour and grayscale images for example slices of samples BALL02 and BALL03 using the EPSON Expression 11000XL flatbed scanner.

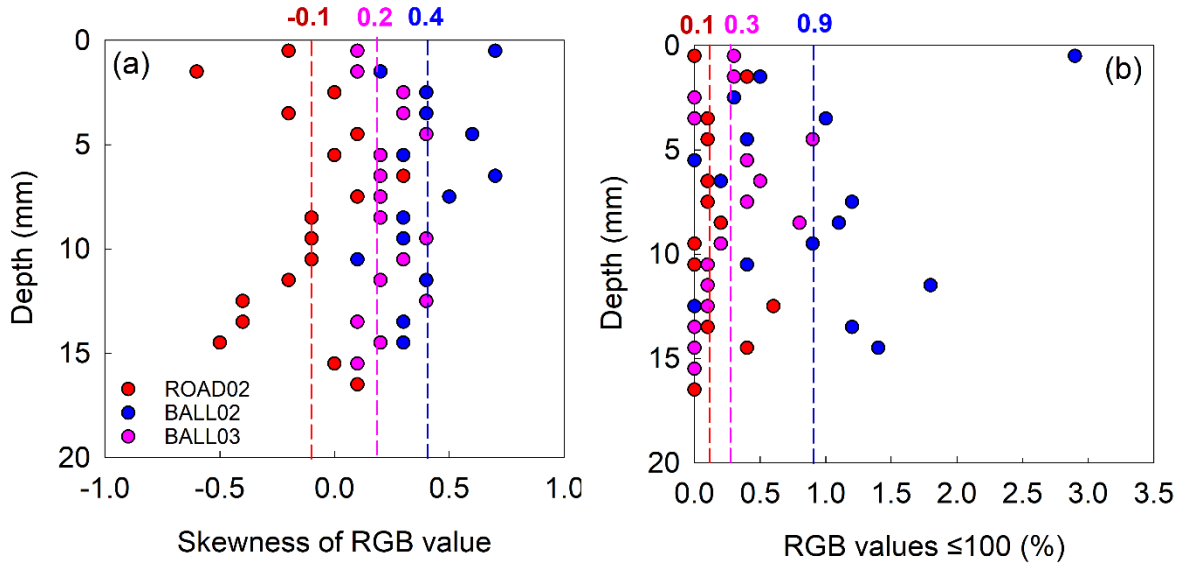

Fig. S4. Analysis of RGB values with depth for samples ROAD02, BALL02 and BALL03: (a) skewness of the pixel values for each images; (b) percentage of RGB values that are ≤100 (i.e. dark coloured).

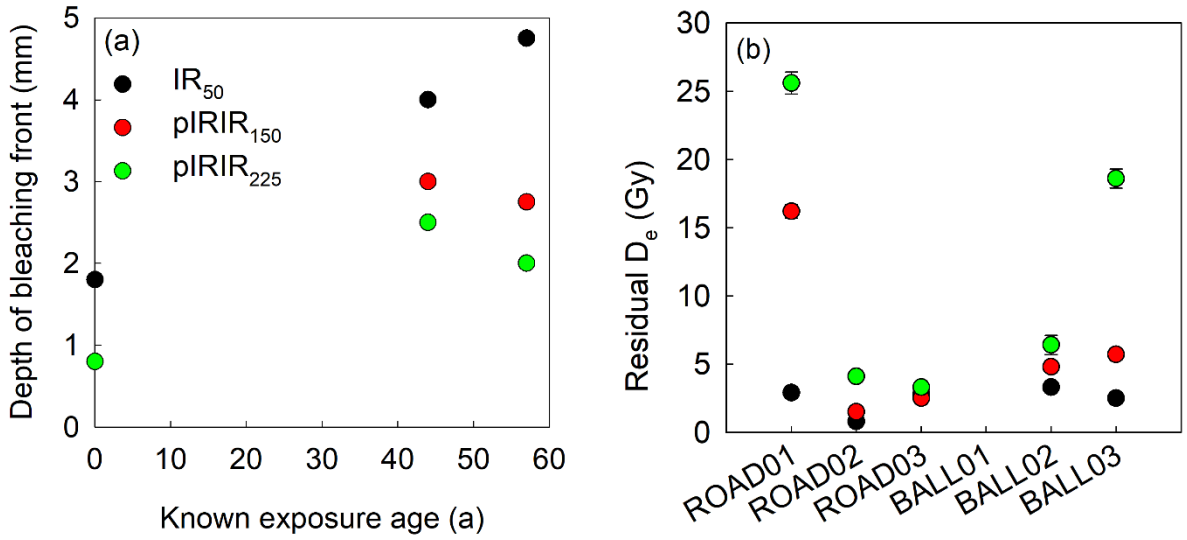

Fig. S5. (a) Depth of bleaching fronts for the known-age samples ROAD01 (0.01 a), ROAD02 (57 a) and ROAD03 (44 a). Note that the depth of the $pIRIR_{150}$ and $pIRIR_{225}$ bleaching fronts were identical for ROAD01 (0.01 a known-age sample). (b) Residual D_e values determined for the surface slice (0-1 mm depth) of each sample. Note that sample BALL01 is not plotted on this figure as the residual D_e values were large for all the IRSL signals: IR_{50} (477.5 ± 20.7 Gy), $pIRIR_{150}$ (574.6 ± 36.5 Gy) and $pIRIR_{225}$ (could not be interpolated on to the dose-response curve).

Fig. S6. Photograph of the Beinn Alligin rock avalanche to illustrate the nature of the area surrounding the sampled boulders, which includes dense vegetation, the small-scale topography of the boulders and little evidence of shattered material.

Table S1. Multi-elevated temperature post- IR IRSL sequence used for analysis.

Step	Procedure
1	Natural or regenerative dose
2	Preheat 250 °C for 100 s
3	IR LEDs 50 °C for 200 s
4	IR LEDs 150 °C for 200 s
5	IR LEDs 225 °C for 200 s
6	Test-dose 53 Gy
7	Preheat 250 °C for 100 s
8	IR LEDs 50 °C for 200 s
9	IR LEDs 150 °C for 200 s
10	IR LEDs 225 °C for 200 s
11	IR LEDs 290 °C for 200 s

Table S2. Raw L_n/T_n data used for fitting sample ROAD01 in Fig. 4A-C. Note that two rather than three cores were analysed for this sample.

	Core 1						Core 2					
	IR_{50}		$pIRIR_{150}$		$pIRIR_{225}$		IR_{50}		$pIRIR_{150}$		$pIRIR_{225}$	
Depth (mm)	L_n/T_n	Error	L_n/T_n	Error	L_n/T_n	Error	L_n/T_n	Error	L_n/T_n	Error	L_n/T_n	Error
0.5	0.01	0.00	0.06	0.00	0.11	0.00	0.05	0.00	0.16	0.01	0.25	0.01
1.5	0.20	0.01	0.68	0.02	0.79	0.03	0.64	0.02	0.98	0.03	1.02	0.03
2.5	1.02	0.03	1.09	0.03	1.04	0.03	0.98	0.03	0.99	0.03	0.99	0.03
3.5	1.02	0.03	1.03	0.03	1.05	0.03	1.15	0.04	1.01	0.03	0.95	0.03
4.5	0.97	0.03	1.01	0.03	1.02	0.03	0.94	0.03	0.93	0.03	0.97	0.03
5.5	1.01	0.03	1.01	0.03	1.04	0.03	1.04	0.03	1.03	0.03	1.03	0.03
6.5	1.02	0.03	1.06	0.03	1.05	0.03	1.03	0.03	0.99	0.03	0.98	0.03
7.5	1.00	0.03	0.98	0.03	0.98	0.03	1.04	0.03	1.02	0.03	1.03	0.03
8.5	1.03	0.03	0.99	0.03	0.98	0.03	1.06	0.03	0.98	0.03	1.00	0.03
9.5	1.09	0.03	1.04	0.03	1.03	0.03	1.00	0.03	1.00	0.03	1.00	0.03
10.5	1.10	0.03	1.07	0.03	1.04	0.03						
11.5	1.00	0.03	1.00	0.03	1.00	0.03						
12.5												
13.5												
14.5												
15.5												
16.5												
17.5												
18.5												
19.5												

Table S3. Raw L_n/T_n data used for fitting sample ROAD02 in Fig. 4G-I.

	Core 1						Core 2						Core 3					
	IR_{50}		$pIRIR_{150}$		$pIRIR_{225}$		IR_{50}		$pIRIR_{150}$		$pIRIR_{225}$		IR_{50}		$pIRIR_{150}$		$pIRIR_{225}$	
Depth (mm)	L_n/T_n	Error	L_n/T_n	Error	L_n/T_n	Error	L_n/T_n	Error	L_n/T_n	Error	L_n/T_n	Error	L_n/T_n	Error	L_n/T_n	Error	L_n/T_n	Error
0.5	0.00	0.00	0.01	0.00	0.02	0.00							0.02	0.00	0.37	0.01	0.64	0.02
1.5	0.00	0.00	0.02	0.00	0.13	0.00							0.07	0.00	1.02	0.03	1.12	0.04
2.5	0.01	0.00	0.29	0.01	0.61	0.02	0.02	0.00	0.75	0.02	1.01	0.03	0.55	0.02	1.01	0.03	1.03	0.03
3.5	0.03	0.00	0.76	0.02	0.89	0.03							0.90	0.03	1.08	0.03	1.06	0.03
4.5	0.15	0.00	0.96	0.03	1.03	0.03	0.43	0.01	0.92	0.03	1.07	0.03	0.96	0.03	1.09	0.03	1.13	0.04
5.5	0.47	0.01	0.93	0.03	0.99	0.03	0.85	0.03	0.92	0.03	1.08	0.03	1.00	0.03	1.00	0.03	1.00	0.03
6.5	1.06	0.03	0.93	0.03	1.00	0.03	0.98	0.03	0.96	0.03	1.12	0.03						
7.5	0.96	0.03	1.01	0.03	1.00	0.03	0.93	0.03	0.87	0.03	1.00	0.03						
8.5	1.14	0.03	1.05	0.03	1.02	0.03	1.00	0.03	0.88	0.03	1.01	0.03						
9.5	1.02	0.03	1.00	0.03	1.02	0.03	1.04	0.03	0.98	0.03	1.08	0.03						
10.5							1.00	0.03	0.99	0.03	1.08	0.03						
11.5	1.03	0.03	0.98	0.03	0.97	0.03	1.11	0.03	1.00	0.03	1.10	0.03						
12.5	1.00	0.03	1.00	0.03	1.00	0.03	1.09	0.03	0.89	0.03	0.95	0.03						
13.5							1.22	0.04	0.99	0.03	1.02	0.03						
14.5							1.31	0.04	0.99	0.03	0.97	0.03						
15.5							1.05	0.03	0.95	0.03	1.07	0.03						
16.5							1.25	0.04	1.00	0.03	1.00	0.03						
17.5																		
18.5																		
19.5																		

Table S4. Raw L_n/T_n data used for fitting sample ROAD03 in Fig. 4D-F.

	Core 1						Core 2						Core 3					
	IR_{50}		$pIRIR_{150}$		$pIRIR_{225}$		IR_{50}		$pIRIR_{150}$		$pIRIR_{225}$		IR_{50}		$pIRIR_{150}$		$pIRIR_{225}$	
Depth (mm)	L_n/T_n	Error	L_n/T_n	Error	L_n/T_n	Error	L_n/T_n	Error	L_n/T_n	Error	L_n/T_n	Error	L_n/T_n	Error	L_n/T_n	Error	L_n/T_n	Error
0.5	0.00	0.00	0.01	0.00	0.02	0.00	0.00	0.00	0.02	0.00	0.07	0.00	0.01	0.00	0.01	0.00	0.02	0.00
1.5	0.01	0.00	0.03	0.00	0.11	0.00	0.01	0.00	0.15	0.01	0.32	0.01	0.01	0.00	0.04	0.00	0.12	0.00
2.5	0.09	0.00	0.66	0.02	0.70	0.02	0.07	0.00	0.44	0.01	0.59	0.02	0.04	0.00	0.43	0.01	0.56	0.02
3.5							0.10	0.00	0.40	0.01	0.41	0.01	0.12	0.00	0.72	0.02	0.71	0.02
4.5	0.65	0.02	1.03	0.03	1.05	0.03	0.74	0.02	0.93	0.03	1.03	0.03	0.93	0.03	0.96	0.03	0.71	0.02
5.5	1.00	0.03	1.00	0.03	1.00	0.03	0.95	0.03	0.99	0.03	1.05	0.03	1.00	0.03	0.92	0.03	0.88	0.03
6.5							1.32	0.04	1.26	0.04	1.23	0.04	0.77	0.02	0.81	0.02	0.90	0.03
7.5							1.16	0.04	1.06	0.03	1.02	0.03	0.90	0.03	0.95	0.03	0.96	0.03
8.5							1.05	0.03	1.05	0.03	1.07	0.03	0.85	0.03	0.89	0.03	0.87	0.03
9.5							0.85	0.03	0.91	0.03	0.90	0.03	0.82	0.03	0.87	0.03	0.92	0.03
10.5							1.01	0.03	0.99	0.03	1.08	0.03	1.00	0.03	0.86	0.03	0.86	0.03
11.5							1.02	0.03	1.08	0.03	1.09	0.03	0.99	0.03	1.00	0.03	1.00	0.03
12.5							1.04	0.03	0.97	0.03	0.98	0.03	0.85	0.03	0.80	0.02	1.00	0.03
13.5							1.04	0.03	1.07	0.03	1.09	0.03	0.99	0.03	0.92	0.03	0.90	0.03
14.5							1.03	0.03	1.02	0.03	1.05	0.03						
15.5							0.96	0.03	1.07	0.03	1.14	0.04						
16.5							0.93	0.03	0.98	0.03	1.04	0.03						
17.5							1.08	0.03	1.05	0.03	1.07	0.03						
18.5							1.09	0.03	1.17	0.04	1.14	0.04						
19.5							1.00	0.03	1.00	0.03	1.00	0.03						

Table S5. Raw L_n/T_n data used for fitting sample BALL01 in Fig. 5A-C.

	Core 1						Core 2						Core 3						Core 4					
	IR_{50}		$pIRIR_{150}$		$pIRIR_{225}$		IR_{50}		$pIRIR_{150}$		$pIRIR_{225}$		IR_{50}		$pIRIR_{150}$		$pIRIR_{225}$		IR_{50}		$pIRIR_{150}$		$pIRIR_{225}$	
Depth (mm)	L_n/T_n	Error	L_n/T_n	Error	L_n/T_n	Error	L_n/T_n	Error	L_n/T_n	Error	L_n/T_n	Error	L_n/T_n	Error	L_n/T_n	Error	L_n/T_n	Error	L_n/T_n	Error	L_n/T_n	Error	L_n/T_n	Error
0.5	0.70	0.02	0.93	0.03	0.99	0.03	1.25	0.04	1.28	0.04	1.19	0.04							1.99	0.06	1.50	0.05	1.35	0.04
1.5	0.93	0.03	1.06	0.03	1.02	0.03	1.17	0.04	1.30	0.04	1.18	0.04	1.28	0.04	0.82	0.03	0.96	0.03	1.21	0.04	1.13	0.03	1.13	0.04
2.5	1.21	0.04	1.14	0.03	1.07	0.03	0.71	0.02	0.79	0.02	0.80	0.02	0.72	0.02	0.75	0.02	0.79	0.02	1.12	0.03	1.15	0.04	1.15	0.04
3.5	1.00	0.03	1.08	0.03	1.10	0.03	0.84	0.03	1.06	0.03	1.00	0.03							1.55	0.05	1.28	0.04	1.18	0.04
4.5	0.86	0.03	1.02	0.03	1.05	0.03	1.00	0.03	1.10	0.03	1.00	0.03	1.18	0.04	1.03	0.03	0.92	0.03	1.19	0.04	1.05	0.03	1.08	0.03
5.5	0.73	0.02	0.80	0.02	0.89	0.03	1.14	0.03	1.26	0.04	1.14	0.04							1.26	0.04	0.96	0.03	0.94	0.03
6.5	0.79	0.02	1.00	0.03	1.00	0.03	0.71	0.02	1.00	0.03	1.00	0.03	1.12	0.03	0.92	0.03	0.83	0.03	1.00	0.03	1.00	0.03	1.00	0.03
7.5	1.02	0.03	1.15	0.04	1.10	0.03							0.82	0.03	0.79	0.02	0.83	0.03	1.10	0.03	0.90	0.03	0.88	0.03
8.5	0.72	0.02	0.78	0.02	0.84	0.03							1.35	0.04	1.10	0.03	0.96	0.03	1.01	0.03	0.92	0.03	0.91	0.03
9.5	1.27	0.04	1.15	0.04	1.09	0.03													1.18	0.04	0.99	0.03	0.90	0.03
10.5	0.70	0.02	1.03	0.03	1.08	0.03							0.84	0.03	0.81	0.02	0.82	0.03	1.31	0.04	1.00	0.03	0.92	0.03
11.5	0.49	0.02	0.57	0.02	0.64	0.02													1.30	0.04	1.06	0.03	0.97	0.03
12.5	0.40	0.01	0.63	0.02	0.70	0.02							0.90	0.03	0.86	0.03	0.86	0.03	0.98	0.03	0.93	0.03	0.93	0.03
13.5													1.00	0.03	1.00	0.03	1.00	0.03						
14.5																								
15.5																								
16.5																								
17.5																								
18.5																								
19.5																								

Table S6. Raw L_n/T_n data used for fitting sample BALL02 in Fig. 5D-F.

	Core 1						Core 2						Core 3					
	IR_{50}		$pIRIR_{150}$		$pIRIR_{225}$		IR_{50}		$pIRIR_{150}$		$pIRIR_{225}$		IR_{50}		$pIRIR_{150}$		$pIRIR_{225}$	
Depth (mm)	L_n/T_n	Error	L_n/T_n	Error	L_n/T_n	Error	L_n/T_n	Error	L_n/T_n	Error	L_n/T_n	Error	L_n/T_n	Error	L_n/T_n	Error	L_n/T_n	Error
0.5																		
1.5							0.00	0.00	0.04	0.00	0.16	0.01	0.01	0.00	0.02	0.00	0.04	0.00
2.5							0.01	0.00	0.15	0.01	0.40	0.01	0.03	0.00	0.46	0.01	0.61	0.02
3.5	0.39	0.01	0.89	0.03	0.91	0.03	0.35	0.01	0.93	0.03	0.91	0.03	0.16	0.01	1.08	0.03	1.03	0.03
4.5	1.21	0.04	1.05	0.03	1.03	0.03	0.80	0.02	0.98	0.03	1.03	0.03	0.87	0.03	1.29	0.04	1.17	0.04
5.5	1.05	0.03	0.96	0.03	1.04	0.03	1.16	0.04	1.24	0.04	1.19	0.04	0.84	0.03	1.12	0.03	1.09	0.03
6.5	1.02	0.03	0.95	0.03	0.97	0.03							0.99	0.03	1.20	0.04	1.12	0.04
7.5	0.98	0.03	0.83	0.03	0.87	0.03	1.06	0.03	1.04	0.03	1.01	0.03	0.96	0.03	1.09	0.03	1.01	0.03
8.5	1.04	0.03	1.02	0.03	1.03	0.03	1.15	0.03	1.18	0.04	1.15	0.04	0.90	0.03	1.16	0.04	1.08	0.03
9.5	0.94	0.03	0.93	0.03	0.94	0.03	1.23	0.04	1.06	0.03	0.98	0.03	0.92	0.03	1.10	0.03	1.07	0.03
10.5	0.92	0.03	0.98	0.03	0.99	0.03	1.40	0.04	1.22	0.04	1.14	0.04	1.00	0.03	1.00	0.03	1.00	0.03
11.5							1.03	0.03	1.12	0.03	1.17	0.04						
12.5	1.13	0.03	1.02	0.03	1.01	0.03	1.01	0.03	1.09	0.03	1.05	0.03						
13.5	1.15	0.04	0.93	0.03	0.93	0.03												
14.5	1.00	0.03	1.00	0.03	1.00	0.03	1.02	0.03	1.07	0.03	1.08	0.03						
15.5	1.05	0.03	0.92	0.03	0.94	0.03	1.00	0.03	1.00	0.03	1.00	0.03						
16.5	1.14	0.03	1.06	0.03	1.04	0.03												
17.5																		
18.5																		
19.5																		

Table S7. Raw L_n/T_n data used for fitting sample BALL03 in Fig. 5G-I.

	Core 1						Core 2						Core 3					
	IR_{50}		$pIRIR_{150}$		$pIRIR_{225}$		IR_{50}		$pIRIR_{150}$		$pIRIR_{225}$		IR_{50}		$pIRIR_{150}$		$pIRIR_{225}$	
Depth (mm)	L_n/T_n	Error	L_n/T_n	Error	L_n/T_n	Error	L_n/T_n	Error	L_n/T_n	Error	L_n/T_n	Error	L_n/T_n	Error	L_n/T_n	Error	L_n/T_n	Error
0.5													0.00	0.00	0.01	0.00	0.03	0.00
1.5													0.01	0.00	0.04	0.00	0.11	0.00
2.5	0.00	0.00	0.07	0.00	0.26	0.01	0.01	0.00	0.26	0.01	0.64	0.02	0.01	0.00	0.15	0.00	0.34	0.01
3.5							0.01	0.00	0.33	0.01	0.62	0.02	0.04	0.00	0.52	0.02	0.76	0.02
4.5	0.06	0.00	0.72	0.02	0.76	0.02	0.07	0.00	0.80	0.02	0.98	0.03	0.33	0.01	0.85	0.03	0.85	0.03
5.5	0.25	0.01	0.86	0.03	0.78	0.02	0.39	0.01	0.88	0.03	0.95	0.03	0.78	0.02	0.91	0.03	0.90	0.03
6.5	1.11	0.03	1.03	0.03	0.92	0.03	0.78	0.02	1.12	0.03	1.16	0.04	0.75	0.02	0.75	0.02	0.80	0.02
7.5	1.29	0.04	1.17	0.04	1.04	0.03	0.88	0.03	0.98	0.03	1.01	0.03	0.88	0.03	0.86	0.03	0.92	0.03
8.5	1.06	0.03	1.03	0.03	0.97	0.03	0.74	0.02	1.00	0.03	1.11	0.03	0.99	0.03	0.93	0.03	0.95	0.03
9.5	1.07	0.03	1.12	0.03	1.05	0.03	1.00	0.03	1.00	0.03	1.00	0.03	1.15	0.04	1.09	0.03	1.06	0.03
10.5	1.15	0.03	1.04	0.03	1.00	0.03							1.16	0.04	1.07	0.03	1.04	0.03
11.5	1.07	0.03	1.00	0.03	0.92	0.03							1.01	0.03	0.95	0.03	0.97	0.03
12.5	1.12	0.03	1.01	0.03	0.97	0.03							1.00	0.03	1.00	0.03	1.00	0.03
13.5	1.29	0.04	1.03	0.03	0.97	0.03												
14.5	1.13	0.03	1.15	0.04	1.09	0.03												
15.5	0.99	0.03	0.95	0.03	0.93	0.03												
16.5	1.00	0.03	1.00	0.03	1.00	0.03												
17.5																		
18.5																		
19.5																		